Electronic Spectroscopy of Cold Cations in a 22-Pole Trap by Indirect Methods

Inauguraldissertation

zur

Erlangung der Würde eines Doktors der Philosophie

vorgelegt der

Philosophisch-Naturwissenschaftlichen Fakultät

der Universität Basel

von

Satrajit Chakrabarty

aus

Kolkata, Indien

Basel 2013

Genehmigt von der Philosophisch-Naturwissenschaftlichen Fakultät

auf Antrag von

Prof. Dr. J. P. Maier und Prof. Dr. S. Willitsch

Basel, 18. 6. 2013

Prof. Dr. Jörg Schibler
Dekan

I would like to express my gratitude to Prof. J. P. Maier for giving me the opportunity to carry out my doctoral studies in his group. The excellent facilities and the available support are highly appreciated. I thank him for his patience and guidance during the research related discussions that we have had.

I would like to thank Prof. S. Willitsch for agreeing to be the co-referee for my thesis. I benefited greatly from attending his course on spectroscopy.

Prof. Pfohl is thanked for chairing my defence.

During the last year of my PhD, I had the chance to work with Prof. D. Gerlich. This proved to be one of the most enriching and exciting phases of my stay in Basel. His deep knowledge on ion-trapping and inexhaustible enthusiasm for science in general are things of wonder. I consider myself fortunate to have shared lab space with him.

The contributions of Prof. G. A. H. Walker and Prof. D. A. Bohlender as co-authors are duly acknowledged.

I do not know the appropriate words to thank the following three individuals: Dr. Corey Rice, Dr. Rainer Dietsche and Mathias Holz. Just like the first beer that Corey forced into my hand one evening by the Rhine, he forced a lot more into my brain. Beginning from showing me how to trap ions and explaining spectroscopy to the fine art of soldering, Corey was always there to extend a helping hand. It was an absolute pleasure to work with Rainer. I should also thank him for being an excellent travel companion on our trip to the US. Mathias has been a fantastic addition to the group not just because of his skills but also because he is a great labmate to work with. The many sleepless nights that were spent in the lab would have been quite dreary had it not been for Rainer in the beginning and then Mathias.

I thank Dr. Vitaly Rudnev, who also explained the many aspects of the machine in my early days in the group. I will fondly remember the many discussions that we had about philosophy, culture and world history.

I am extremely grateful to Dr. A. Johnson for his constant support with the lasers and LabView programming. Inspite of the numerous laser systems in our laboratories, he would always make time to help out the individual groups.

During my stay in Basel, I did not come across anyone so absolutely immersed in spectroscopy as Dr. F. Mazzotti. Consequently, I learned plenty from him. His contributions as a co-author are also duly acknowledged.

I thank Dr. J. Fulara for introducing me to *ab-initio* methods and for the calculations on the $C_4H_3Cl^+$ isomers. I also thank him for teaching me the subtleties of cross-country skiing.

Dr. R. Nagarajan and Dr. A. Gopalan are thanked for their constant encouragement and helpful discussions.

Dr. R. Raghunandan and Dr. V. Gupta proved to be wonderful friends and I thank them for the many great evenings that we spent at Best Pizza.

I am grateful to other past and present members of the group that I have worked with.

Much of the work that we do in the laboratory would not have been possible without the excellent support from all the members of our mechanical workshop.

G. Holderied is also an indispensable and valuable member of the group. It would be a nightmare of a week if Georg were to be on vacation and one of our electronics refused to function.

Special thanks to the secretaries; Esther Stalder, Daniela Tischhauser and Maya Greuter. Much of the administrative matters that most of us dislike are taken care of by them.

I greatly enjoyed the company of Dr. S. Barat. I thank Dr. S. Roy and Dr. R. Paul. Over the years, the two of them have become more like brothers, by sharing their experiences and always reminding me from where I come. Times spent with all three of them discussing philosophy and life in general were especially enjoyable since all of us have the same mother-tongue.

I thank Dr. V. Balasubramanian, Dr. V. Shankar, Dr. P. Shende, Dr. S. More and Dr. S. Shankar for the colourful evenings that we enjoyed together.

I always greatly enjoyed the game of cricket but was never good to play it at any competitive level in India. Therefore when I found that I was more than welcome to play for Basel Cricket Club, I was elated. I thank my fellow team-mates for some of the best memories that I will carry with me from Switzerland.

I had an extremely interesting time working for the Calcutta Project. To look at my own country and city through someone else's eyes enlightened me far more than I expected to be. I thank all the members of the project for being so friendly and willing to accommodate me even though I do not speak any Swiss-German. I am grateful to the project for more than one reason because this is where I met Angela. Thanks for your support and understanding.

I would like to thank my friends back in India. My Best Wishes to all of you.

Finally, Thanks to my family.

Contents

1 Introduction

1.1 Motivation

Research in molecular spectroscopy of ions can be broadly classified into three categories based on underlying motivations. The first interest is in characterisation of the electronic, vibrational and rotational quantum levels with energy resolution and accuracy. Photoionisation and photoelectron spectroscopy have been used before. Another impetus relates to identification and structural characterisation of ions formed as a result of reactions between precursors. The third interest has been in observing the wavelengths and transition intensities of absorption and emission of ions. Related experiments have tried to answer fundamental questions connected to molecular identification in extra-terrestrial environments. Experiments presented in this thesis belong to the third category. This is discussed in greater detail in the following paragraphs.

The longest standing problem in astronomical spectroscopy is the identification of the Diffuse Interstellar Bands (DIBs). Absorption features are observed in the spectra measured towards stars located behind diffuse interstellar clouds and lie mostly in the visible part of the electromagnetic spectrum. After the first observations made by Mary Lea Heger during her Ph.D. studies at Lick observatory in 1931, [1] systematic studies were conducted by Merrill. [2] In 1934 he reported,

> *Recent observations at Mount Wilson, made chiefly to investigate the interstellar sodium lines, have disclosed four additional detached lines in the yellow and red whose approximate wave-lengths are 5780.4, 5796.9, 6283.9 and 6613.9 Å, respectively. These lines, found in types*

> *Oa to A4, behave like interstellar lines with regard to occurrence, intensity and displacement. Instead of being narrow and sharp, however, as interstellar lines should be, they are somewhat widened and have rather diffuse edges. Their chemical identifications have not been found. The widening of the lines and the difficulty of identification make the problem of their atomic origin an interesting one.*

Since the integration of high-resolution spectrographs with large telescopes, DIBs have been observed in over a hundred sightlines in the Milky Way, [3] Magellanic Clouds [4] and at cosmological distances. [5] The latest databases report more than 600 DIBs. Merrill's work proved definitively that the origin of these lines is the ISM and not caused by stellar emission. The central wavelength of DIBs that they observed in the spectrum of a binary star remained constant, while the stellar lines were periodically Doppler shifted by the orbital motion of the binary system. [6] These features are termed diffuse because they are somewhat hazy when compared to sharp atomic transitions in the interstellar medium (ISM). The linewidths ($\sim 2-100\,\mathrm{cm}^{-1}$) seem to be an intrinsic property of carriers and is independent of the physical conditions of the clouds in which they occur. Their diffuse character and the fact that they do not match with any known atomic lines, support the assumption that they have molecular origins. The widths have been attributed to short lifetimes of the excited states. This is further supported by the fact that the central wavelengths and profiles in different sightlines appear to be constant. Fine structures have also been observed in some DIBs. The spectra span across the range $\sim$4 000 to 13 000 Å, which corresponds to photon energy of 1-3 eV. Other spectroscopic characteristics include an absence of regularity in the wavenumbers of these bands and common bandwidths as would be expected in case the same excited state with a short lifetime were accessed by more than one transition. The latter is actually unlikely though if all excitations originate from the same quantum level due to the low temperature of the cloud. Over the last 30 years, the idea that the DIBs are due to gas phase molecules have gained popularity. Large molecules can absorb photons without undergoing destruction and can give rise to broad spectra due to fast internal relaxation. [7] The idea

of molecular origin of the DIBs was strongly advocated by Herzberg. Predissociation or preionisation contributing to the widths of the bands is a more recent idea. Other suggested assignments include colour centres, lattice defects, hydrogen anion, porphyrins, carbon chains, charge transfer transitions and molecular hydrogen. [8, 9] Polycyclic aromatic hydrocarbons (PAHs), fullerenes in various forms and even carbon nanotubes have been proposed as possible carriers. Additionally the "unidentified" infrared (UIR) emission bands arising from PAHs in nebullar and other regions has given birth to the "PAH hypothesis." [10, 11]

Laboratory measurements of electronic transitions of the potential carriers have to be done under conditions comparable to the ISM. This warrants the use of low temperatures (5-80 K) and rarefied environments where collisions between the molecules of interest have a low probability. Development of cryogenic ion-trapping technology has assisted in the field of ion spectroscopy. These storage devices allow ion confinement for long times without appreciable losses, which make them ideal for spectroscopic applications. Long interaction times also mean one can circumvent problems of ion generation in sufficient quantities by choosing to employ 'action' spectroscopic techniques, as opposed to the more conventional direct absorption methods where higher number densities of the sample are essential.

In this thesis, three such indirect methods have been used. The first two methods, resonant photodissociation and laser induced charge transfer, are well characterised and have been applied by others. The third method, laser induced inhibition of complex growth is an entirely new technique that was developed and tested for the first time.

1.2 Experimental aspects

Irrespective of the methods utilised, the experimental techniques of ion generation, mass filtering and confining and cooling them in a multipole trap remained the same. A temperature variable 22-pole trap was used as the ion confining device for this thesis. The wide field free region offered by such a trap ensures cooled ions

undergo very little interaction with trapping rf-fields which might lead to heating of the ions. The ions can be stored upto several minutes making long interaction times with a laser or neutral molecules possible. These make it an ideal choice for performing spectroscopy on cold molecular ions.

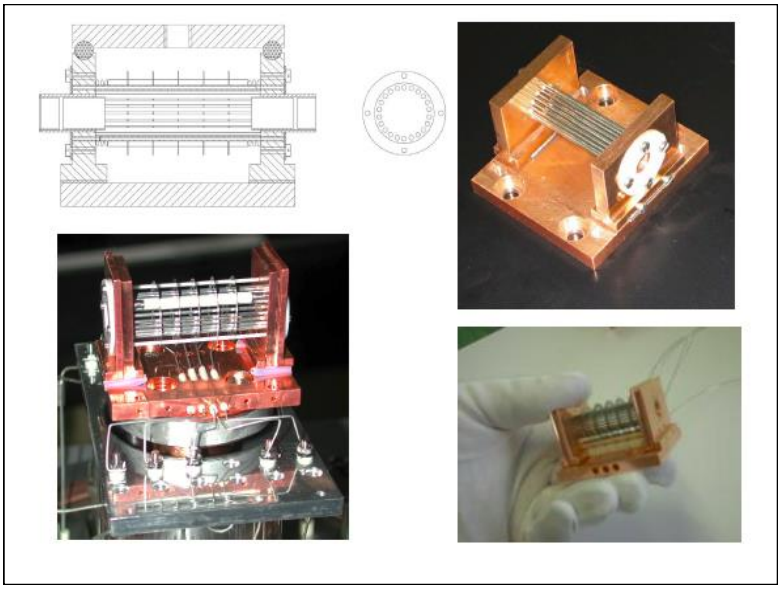

Figure 1.1: Different constructions of the 22-pole trap along with end-cap and ring electrodes.

Over the last 20 years, cold molecular ions have attracted plenty of interest because of their possible applications. Figure 1.2 summarises some of these.

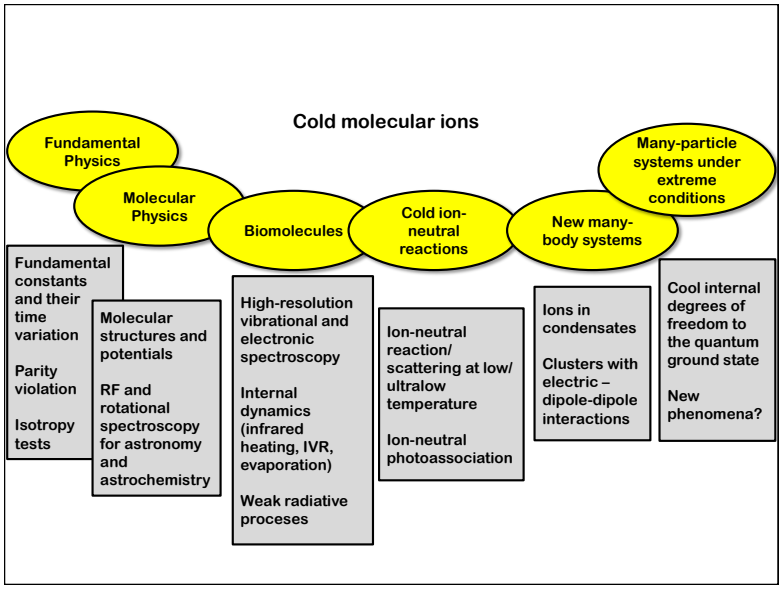

Figure 1.2: Overview of applications of cold molecular ions. [12]

There are several available techniques that have become rather standard for achieving low temperatures. For the purposes of comparison to DIB data, the temperature range most relevant is from 10 - 50 K. Additionally, all internal degrees of freedom in a molecule are equilibrated in the ISM. Therefore, it is essential to reproduce such laboratory conditions. From small ion traps to large storage rings- there are several devices available for this purpose. Externally created ions are trapped in potential wells and can then are collisionally cooled with a buffer gas. Even large molecules like proteins have been cooled in this way. [13] For most of the experiments discussed later, the trapped ions have been cooled by collisions with helium buffer gas.

1.3 Outline of the thesis

Chapter 2 discusses the fundamental principles and governing equations of mass filtering and ion motion in mutipole fields. Confinement of ions in the latter are discussed with special emphasis on characteristic trapping parameters and ideal operating conditions.

The underlying quantum mechanics and basic principles of spectroscopy are discussed in **Chapter 3**. Several spectroscopic techniques are mentioned. The methods that are relevant for this thesis have been dealt with in greater detail.

The experimental setup, and its configurations and laser systems have been described in **Chapter 4**.

Chapters 5-7 present results obtained by the use of three different "indirect" methods. These three techniques are as follows:

1. Photodissociation spectroscopy in which a fragmentation channel was monitored to generate electronic spectra.

2. The second method looked at products from laser induced reactions.

3. The third one is a novel technique that was developed to measure electronic spectra of cold ions.

Bibliography

[1] M. L. Heger. The spectra of certain class B stars in the regions 5360A6680A and 3280A3380A. *Lick. Obs. Bull.*, 337:146, 1922.

[2] P. W. Merrill. Unidentified Interstellar Lines. *Publ. Astron. Soc. Pac.*, 46:206, 1934.

[3] B. J. McCall, M. M. Drosback, J. A. Thorburn, D. G. York, S. D. Friedman, L. M. Hobbs, B. L. Rachford, T. P. Snow, P. Sonnentrucker, and D. E. Welty. Studies of the diffuse interstellar bands. IV. The nearly perfect correlation between 6196.0 and 6613.6. *Astrophys. J.*, 708:1628, 2010.

[4] P. Ehrenfreund, J. Cami, J. Jiménez-Vincente, B. H. Foing, L. Kaper, A. van der Meer, N. Cox, L. d' Hendecourt, F. Salama, P. J. Sarre, T. P. Snow, and P. Sonnentrucker. Detection of diffuse interstellar bands in the Magellanic clouds. *Astrophys. J.*, 576:L117, 2002.

[5] V. T. Junkkarinen, R. D. Cohen, E. A. Beaver, E. M. Burbridge, R. W. Lyons, and G. Madejski. Dust and diffuse interstellar bands in the z_a=0.524 absorption system toward AO 0235+164. *Astrophys. J.*, 614:658, 2004.

[6] P. W. Merrill. Stationary lines in the spectrum of the binary star Boss 6142. *Astrophys. J.*, 83:126, 1936.

[7] P. J. Sarre. The diffuse interstellar bands: a major problem in astronomical spectroscopy. *J. Mol. Spec.*, 238:1, 2006.

[8] G. H. Herbig. The Diffuse Interstellar Bands. *Annu. Rev. Astrophys.*, 33:19, 1995.

[9] T. P. Snow. The unidentied diffuse interstellar bands as evidence for large organic molecules in the interstellar medium. *Spectrochimica Acta Part A*, 57:615, 2001.

[10] A. Léger and L. d' Hendecourt. Are polycyclic aromatic hydrocarbons the carriers of the diffuse interstellar bands in the visible? *Astron. Astrophys.*, 146:81, 1985.

[11] G. P. van der Zwet and L. J. Allamandola. Polycyclic aromatic hydrocarbons and the diffuse interstellar bands. *Astron. Astrophys.*, 146:76, 1985.

[12] Low Temperatures and Cold Molecules, 2008.

[13] J. A. Stearns, Seaiby C, O. V. Boyarkin, and T. R. Rizzo. Spectroscopy and conformational preferences of gas-phase helices. *PCCP*, 11:125, 2009.

2 Ion motion in $2n$-pole fields

I think it is a sad situation in all our chemistry that we are unable to suspend the constituents of matter free.

-Göttingen physicist Georg Christoph Lichtenberg, 18^{th} century

The motion of an ion travelling through a field can be described by the following general differential equation that is derived from Newton's law of motion,

$$\mathbf{F} = m\frac{d^2\mathbf{r}}{dt^2}, \tag{2.1}$$

where $\mathbf{F}$ is the force acting on an ion of mass m and $\mathbf{r}$ is the radius vector from the origin. The force that an ion with a charge q experiences when it moves through an electric field $\mathbf{E}$ and magnetic field $\mathbf{B}$ is given by the Lorentz force law,

$$\mathbf{F} = q\mathbf{E}(\mathbf{r}, t) + q\dot{\mathbf{r}} \times \mathbf{B}(\mathbf{r}, t). \tag{2.2}$$

Here, the fields are dependent on both spatial and temporal coordinates. The ion velocity is given by the first derivative of $\mathbf{r}$. To simplify this equation, it is assumed that the electric field is weak and the particles are heavy with low kinetic energies. This implies the velocity $\dot{\mathbf{r}}$ is very small compared to the speed of light. It can be shown that $B_0 = E_0/c$, where B_0 and E_0 are the maximum amplitudes of the $\mathbf{B}$ and $\mathbf{E}$ and c is the velocity of light. Unless the ion is moving at velocities comparable to light, the force exerted by the magnetic field is weak and not considered. Maxwell equations are used to compute the electric field $\mathbf{E}$. The charges of ions and associated current densities are vanishingly small

under experimental conditions where the density of ions is low enough. Then, the Maxwell equations can be written in the final form,

$$\nabla \cdot \mathbf{E} = 0 \quad \text{and } \nabla \times \mathbf{E} = 0. \tag{2.3}$$

The second of the above equations is valid only for an alternating potential which has a frequency ν low enough such that

$$\lambda = c/\nu \gg l \tag{2.4}$$

That is the wavelength λ associated with the electromagnetic wave must be much greater than length l of the electrode. If the wavelength does not satisfy equation 2.4 there is a possibility of standing waves, which are not predicted by equations 2.3. Typically, the electrodes are much shorter than 1 m and the operating frequencies are ∼10 MHz. Therefore, the above equations are valid for ions in vacuum in the multipoles. Two theorems are made use of to evaluate **E**. Firstly, applying Stoke's theorem to the second of equation 2.3 gives

$$\oint \mathbf{E} \cdot d\mathbf{r} = 0 \tag{2.5}$$

over any closed path which defines a surface over which $\nabla\times$ E = 0. The second theorem asserts that any vector field E, which has the property $\oint \mathbf{E}\cdot d\mathbf{r} = 0$ around every closed path, can be represented as the divergence of a scalar field $\varphi(x, y, z)$, that is

$$\mathbf{E} = -\nabla\varphi(x, y, z) \tag{2.6}$$

The negative sign in equation 2.6 in not essential but is used in keeping with convention. This is analogous to the situation in classical mechanics where the potential energy *U(r)* is defined so that $F = -\nabla U(r)$. The scalar field $\varphi(x, y, z)$ is called the potential function. Equation 2.6 states that a vector field, which normally needs three scalar fields to represent it (one for each component), can

be represented by a single scalar field if equation 2.5 is satisfied for every closed path. Substituting E from equation 2.6 into the first equation of 2.3 gives,

$$\nabla^2\varphi(x,y,z) = 0 \tag{2.7}$$

Equation 2.7 is called Laplace's equation and in rectangular coordinates

$$\nabla^2 = \frac{\partial^2}{\partial x^2} + \frac{\partial^2}{\partial y^2} + \frac{\partial^2}{\partial z^2} \tag{2.8}$$

Once the potential $\varphi = (x, y, z)$ is known, the differential equation of motion can be found using Newton's law of motion

$$\mathbf{F} = m\frac{d^2\mathbf{r}}{dt^2} = -e\nabla\varphi(x,y,z) \tag{2.9}$$

This method is applicable for time varying potentials

$$\varphi(t) = \Phi(t) = U_0 - V_0\, cos(\Omega t) \tag{2.10}$$

where, U_0 is a DC voltage and V_0 is the peak amplitude of the voltage of the RF. A general approach to find the potential function $\varphi(x, y, z)$, is to find a function $A_n(x, y)$, that satisfies Laplace's equation and determine the equipotential surfaces of the pole pieces from this function. If conductors with given applied potentials are designed to coincide with equipotential surfaces, a potential function

$$\varphi(x,y) = K_n A_n(x,y) \tag{2.11}$$

can be found that satisfies Laplace's equation and the boundary conditions by proper choice of K_n. Physically, K_n is related to the dimension of the electrode structure and the applied electrode potentials; it is chosen such that $\varphi(x, y)$ matches the known potentials at the equipotential surfaces. Functions which satisfy Laplace's equation may be found by application of the theory of complex variables. If the complex variable $z = x + \mathrm{i}y$ is raised to an integral power n, then

the result can be expressed as a sum of two parts, a real $A_n(x, y)$ and an imaginary part $B_n(x, y)$

$$(x + iy)^n = A_n(x, y) + B_n(x, y). \tag{2.12}$$

The integer n defines the order of the multipole. From complex variable theory z^n is known to be analytic and so Cauchy-Riemann equations are applicable

$$\frac{\partial A_n(x, y)}{\partial x} = \frac{\partial B_n(x, y)}{\partial y} \tag{2.13}$$

$$\frac{\partial A_n(x, y)}{\partial y} = -\frac{\partial B_n(x, y)}{\partial x}. \tag{2.14}$$

The sum of the partial derivative of the first of these equations with respect to x and the partial derivative of the second with respect to y gives

$$\frac{\partial^2 A_n(x, y)}{\partial x^2} + \frac{\partial^2 B_n(x, y)}{\partial y^2} = 0. \tag{2.15}$$

Thus the function $A_n(x, y)$ satisfies Laplace's equation. In developing the above equations to describe ion motion under specific electric field distributions, several assumptions were made and forces whose magnitudes are small under ideal conditions were ignored. These are listed as follows:

1. Finite length of the electrode structure. The electromagnetic fields are not just functions of x and y but also z. Real electrodes are not infinitely long and on either end of the assembly may give rise to fringe fields.

2. Image force on ions. In reality the charge on the ion, induces an image charge with opposite polarity on the electrode, which draws the ion towards the latter.

3. E fields induced by ions. An ion creates an electric field E at the site of a second ion. The second ion therefore experiences a Coulomb force due to the first one.

4. B fields induced by ions. The motion of an ion generates a magnetic field B which influences the motion of another ion.

5. Radiation by the accelerated ion. An accelerating charge emits electromagnetic radiation which would require an effective force to balance it. This force was neglected.

6. Ion neutral interaction. The interaction of ions with residual gas in the chamber can be described by viscous forces. This is proportional to the speed of the ion and has not been taken into account here.

Gravitational and relativistic effects have also been neglected. [1]

2.1 Quadrupole mass filter

A quadrupole mass filter uses strong focusing principles, similar to those in high energy accelerators, to selectively transport ions of a specific m/z ratio. Ideally, it is constructed from four electrically conducting parallel hyperbolic cylindrical surfaces, described by the equation:

$$x^2 - y^2 = \pm C \tag{2.16}$$

where C is a constant. The opposite electrodes are connected together and the potentials applied to the two pairs are given by,

$$\Phi(t) = U_0 - V_0\, cos(\Omega t) \text{ and} \tag{2.17}$$

$$\Phi(t) = -U_0 + V_0\, cos(\Omega t), \tag{2.18}$$

where $\Omega = 2\pi f$ is the angular frequency. The rod assembly and the applied fields are shown in Figure 2.1.

This gives rise to equipotential surfaces (Figure 2.2) that are symmetric hyperbolic cylinders and the potential along the z-axis is zero.

An ion is injected at the end of such an assembly and parallel to the z-axis undergoes transverse motion under the action of the applied RF and DC fields which are perpendicular to the z-axis. The equations of motion in the xy plane are then given by Mathieu differential equations. Depending on the m/z of the

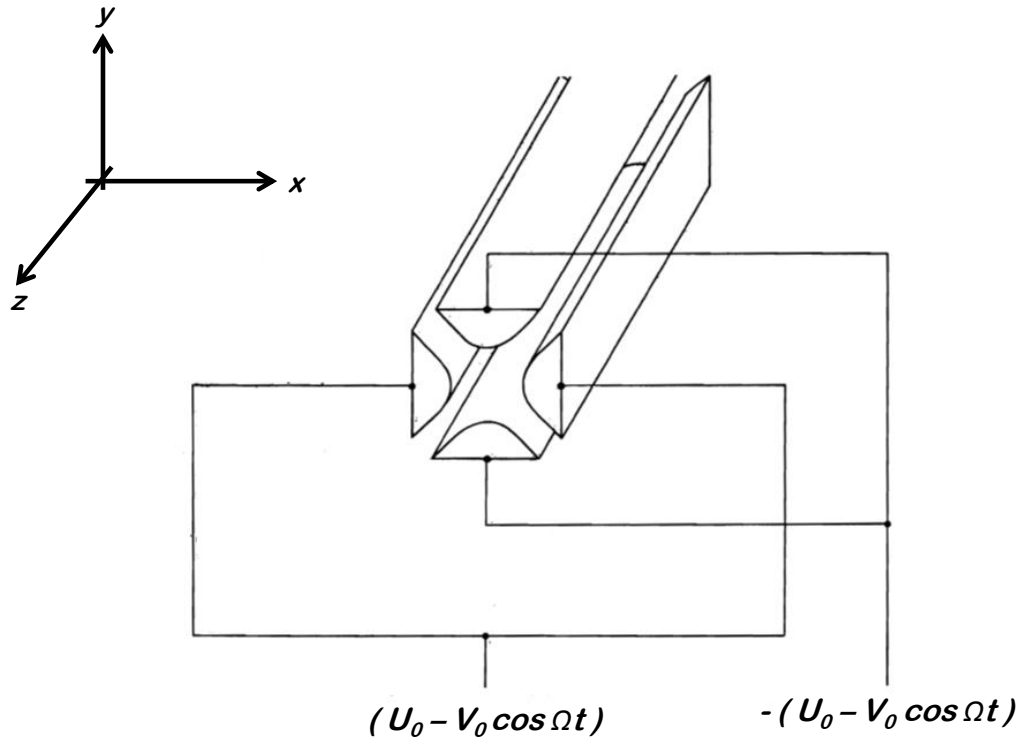

Figure 2.1: A typical quadrupole rod assembly.

ion, the solutions can contain either an oscillatory or an exponential factor. U_0 and V_0 can be properly chosen so that ions of a particular m/z will follow a stable trajectory and emerge on the other side of the quadrupole rod assembly. The other ions progressively move away from the z-axis and are eventually lost on the electrodes.

$$\ddot{x} + \frac{e}{mr_0^2}\,(U_0 - V_0 cos\Omega t)x = 0 \tag{2.19}$$

$$\ddot{y} - \frac{e}{mr_0^2}\,(U_0 - V_0 cos\Omega t)y = 0 \tag{2.20}$$

$$\ddot{z} = 0. \tag{2.21}$$

An inspection of equations 2.19-21 reveals that ion motion is decoupled in the x and y directions. This is a special property exclusive of quadrupole fields.

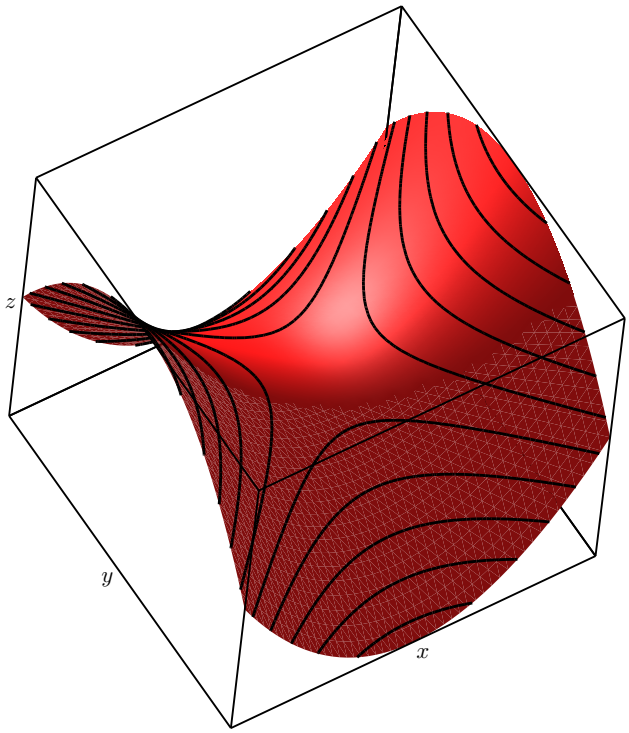

Figure 2.2: The symmetric hyperbolic equipotential surfaces in a quadrupole field.

The region of stable trajectories can be completely characterised in terms of two dimensionless parameters, a and q. These are defined as follows,

$$\frac{4eU_0}{mr_0^2\Omega^2} = a \tag{2.22}$$

$$\frac{2eV_0}{mr_0^2\Omega^2} = q. \tag{2.23}$$

Figure 2.3 shows the regions which are stable in x and y and their overlap. The magnified portion is one such small region. The operation of a quadrupole can be visualised in terms of this diagram. When no DC voltage is applied to the rods, the quadrupole acts as an ion guide in which all ions irrespective of their masses are transmitted. On the (a,q) diagram, this would correspond to regions close to the q axis. Superimposing a DC potential shifts the operating region closer to the cusp of the triangle. This is the mass filtering mode where ions with only

specific m/z are stable. At the vertex infinite resolution and no transmission are experienced. In reality, quadrupoles operate in such a way as to allow optimum transmission at a satisfactory resolution. In some experiments presented later, it was necessary to employ unity mass resolution to observe for fragment ions formed by hydrogen loss.

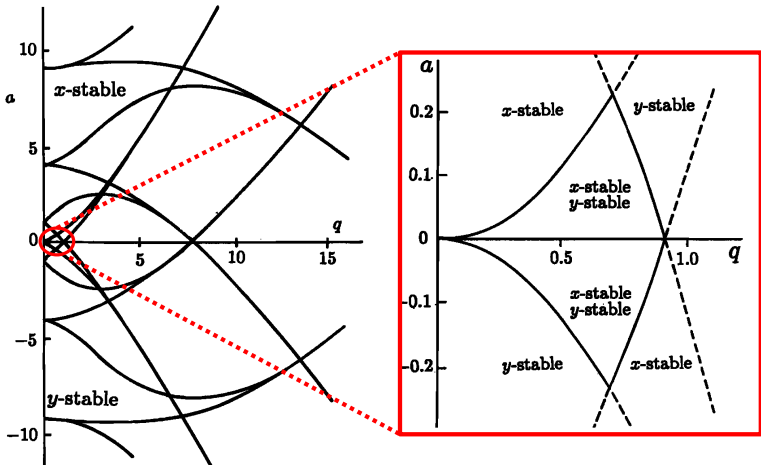

Figure 2.3: The stability diagram showing regions in (a,q) space which correspond to stable trajectories of ions. The expanded portion corresponds to a very small region in the diagram

Proper operation of a mass filter demands mechanical precision of the rod arrangement. In most practical arrangements, hyperbolic cylinders are replaced by circular cylindrical rods. The radii of the rods are chosen so that they are 1.145 times that of the inscribed radius. The fields close to the axis then are a close approximation to the ideal hyperbolic ones.

2.2 Multipoles: 22-pole ion trap

The equations of ion motion in the time dependent field of a multipole cannot be solved analytically because it is no longer decoupled in the x and y directions. Instead, one uses the effective potential approximation to describe the dynamics in

RF traps. The position coordinate is assumed to be a sum of a slowly varying drift motion $\mathbf{R}_0(t)$ and a rapidly oscillating motion $\mathbf{R}_1(t)$. The former is the secular motion and the latter which follows the radiofrequency is the micromotion.

$$\mathbf{r}(t) = \mathbf{R}_0(t) + \mathbf{R}_1(t) \tag{2.24}$$

with

$$\mathbf{R}_1(t) = -\mathbf{a}(t)cos(\Omega t) \tag{2.25}$$

where $\mathbf{a}$(t) is an amplitude vector. By expanding $\mathbf{E}$ in a Taylor series, it can be shown that

$$m\ddot{\mathbf{R}}_0 = -\frac{q^2}{4m\Omega^2}\nabla E^2 \tag{2.26}$$

This equation shows the time averaged influence of the oscillating field on the ion. The field gradient force is caused by the inhomogeneity of the electric field. This force is independent of the nature of the charge and the strength and direction are determined by the gradient of E^2. Therefore, charged particles are always pushed towards weaker fields. An ion can then experience a total average force which can be expressed in terms of a time independent mechanical potential V. The equation of motion for the secular motion can then be written as,

$$m\ddot{\mathbf{R}}_0 = -\nabla\, V^*(\mathbf{R}_0) \tag{2.27}$$

It has been shown that V^* can be expressed as follows

$$V^* = \frac{q^2 n^2 V_0^2}{4m\Omega^2 r_0^2}\left(\frac{r}{r_0}\right)^{2n-2} \tag{2.28}$$

$$V^* = \left\langle \frac{1}{2} m\dot{R}_1^2 \right\rangle, \tag{2.29}$$

where V_0 is the amplitude of the radiofrequency. The first of the above two equations clearly indicates that for increasing values of n, an effective potential is obtained with large field-free central regions with steep walls. The second equation relates the ion's time averaged kinetic energy of micromotion to the

effective potential. So within the effective potential approximation, kinetic energy of drift motion is converted to that of micromotion, providing an upper limit to the maximum radius of drift motion.

For deriving the effective potential, the total average energy was assumed to be an adiabatic constant of the ion motion. However, in reality there are factors that lead to a constant gain in energy because of which the ions may be eventually lost on the electrodes. This can be easily illustrated by the stability diagram of a quadrupole. If the operating conditions lie outside the region of stability, the amplitude of secular motion increases continuously until the ion hits an electrode. For multipoles, it is not possible to construct such (a,q) diagrams because of non-linearity and coupling of the differential equations of motion, another parameter has been used to quantify stable operating conditions for them. It is called the adiabaticity parameter and is given by the equation:

$$\eta = \frac{2q|\nabla E|}{m\Omega^2} \tag{2.30}$$

while for an ideal multipole,

$$\eta = 2n(n-1)\frac{|q|V_0}{m\Omega^2 r_0^2}\left(\frac{r}{r_0}\right)^{n-2} \tag{2.31}$$

The derivation of η is based on the imposed condition that the change in electric field experienced by an ion over the full range of its oscillation is much smaller than the field itself. The condition ∇E=0, leads to quadrupole fields and η is identical to the stability parameter q in this case. Theoretical evaluation of η indicates a value of 0.3 for safe operating conditions. Experimentally, a value of 0.38 has been determined. Gerlich has defined another parameter, the characteristic energy ϵ, to determine V^* and η numerically. [2] This is related to mass, frequency and radius as follows:

$$\epsilon = \frac{1}{2n^2} m\Omega^2 r_0^2. \tag{2.32}$$

ϵ is actually the kinetic energy that the ion possesses due its in-phase motion with the RF while orbiting with a radius r_0. It is obvious that the actual energy of the ion must be much smaller than ϵ for it to show adiabatic behaviour.

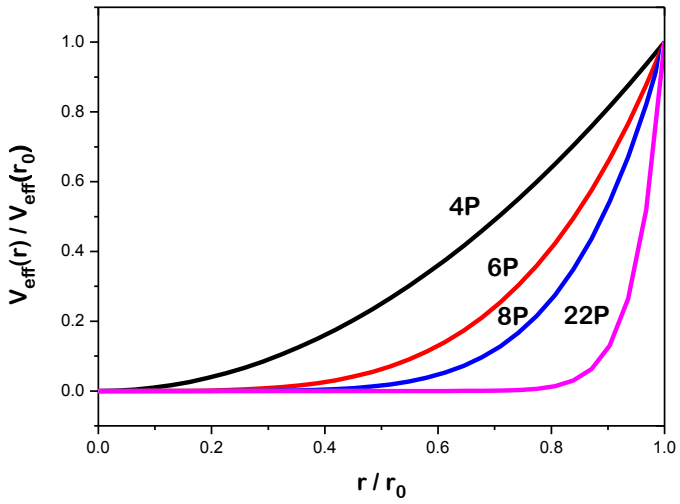

Figure 2.4: The field free region increases with the multipole order. This is illustrated by plotting the effective potential as a function of radial distance from the centre.

The behaviour of the effective potential as a function of r^n is shown in Figure 2.4. The field free region increases dramatically for higher values of n. This is one of the reasons for choosing to work with a 22-pole. The wide area which is free from RF induced perturbations makes it ideal for cooling ions down to the lowest possible temperatures.

Figure 2.5 illustrates the relation between safe operating conditions and the adiabaticity parameter by showing trajectories of ions with different values of η . Although the diagram is for an octopole, the same conclusions apply to all multipoles in general. When η=0.1, energy and angular momentum are conserved. The ion with η=0.7 has undergone one reflection but its energy and angular momentum have been modified. For η=0.4, all three trajectories are stable but differences arise because of non-radial perturbations.

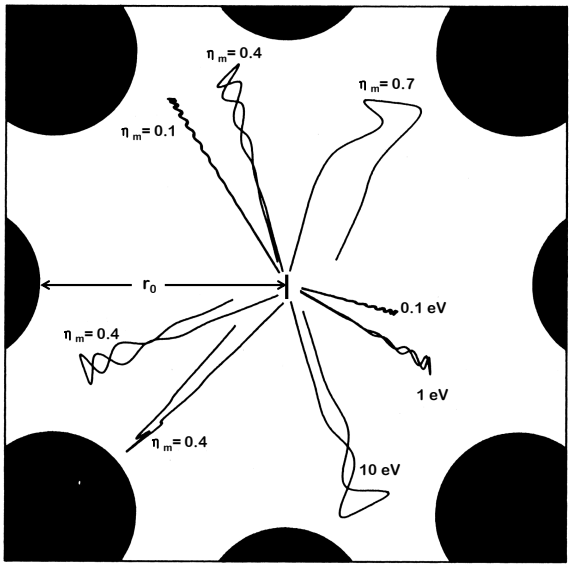

Figure 2.5: Trajectories of ions in an octopole with different starting conditions. The octopole rods have a radius of $r_0/3$. [2]

The other three trajectories have been calculated with same values for ϵ and V_0, but differing transverse energies of 0.1, 1 and 10 eV. [2]

Bibliography

[1] M. H. Friedman, A. L. Yergeyz, and J. E. Campanag. Fundamentals of ion motion in electric radio-frequency multipole fields. *J. Phys. E: Sci. Instrum.*, 115:53, 1982.

[2] Dieter Gerlich. Inhomogeneous Electrical Radio Frequency Fields: A Versatile Tool for the Study of Processes with Slow Ions,. *Adv. Chem. Phys.*, 82:1, 1992.

3 Spectroscopy

3.1 Quantum Mechanics

The central relationship in classical mechanics is Newton's equation of motion:

$$F = m \cdot \frac{d^2x}{dt^2} \tag{3.1}$$

which states that the acceleration on an object is completely determined by the forces acting on it. Given the initial position $x(0)$, initial velocity $(\frac{dx}{dt})_{x=0}$ and the forces $F(\mathrm{t})$ acting on a particle, it is possible to solve for the motion of a particle into the indefinite future. The simple idea of a trajectory of a particle no longer exists in such a form in the quantum world. Quantum mechanics provides a remarkably accurate theory to explain properties and behaviour of small objects. Further, classical mechanics develops naturally as the limiting form of quantum mechanics in the limit of high energies. The central concept in quantum mechanics is that of the wavefunction, Ψ, which determines everything that can be determined about a system. The state of a system composed of N particles is described as fully as possible by its wavefunction $\Psi(x_1, y_1, z_1 \ldots x_N, y_N, z_N, t)$. The quantity $|\Psi|^2 dx_1 dy_1 dz_1 \ldots dx_N dy_N dz_N$ is the probability of finding particle 1 in a small volume $dx_1 dy_1 dz_1$ about the point (x_1, y_1, z_1) while simultaneously finding particles 2,3...N in their respective volumes, all at time t. This is also known as the Born interpretation. The quantum analogue of the classical equation of motion is the time-dependent Schrödinger equation,

$$\hat{H}\Psi = i\hbar \frac{\partial \Psi}{\partial t}. \tag{3.2}$$

This can be expanded a step further to write,

$$-\frac{\hbar^2}{2m}\frac{\partial^2\Psi(x,t)}{\partial x^2} + V(x)\Psi(x,t) = i\hbar\frac{\partial\Psi}{\partial t}. \tag{3.3}$$

Here, m is the mass of the particle and *V(x)* is the potential energy as a function of the position. The solution of the time dependent Schrödinger equation can be written in the form:

$$\Psi(x,t) = C\Psi(x)exp\left(-\frac{iEt}{\hbar}\right). \tag{3.4}$$

This is not a general solution for equation 3.2. This is a linear differential equation that involves Ψ and its derivatives to the first power, so any sum of the solution is also a solution. Thus, the general solution is given by:

$$\Psi(x,t) = \sum_n C_n\Psi_n(x)exp\left(-\frac{iEt}{\hbar}\right), \tag{3.5}$$

where $\Psi_n(x)$ is an eigenfunction of $\hat{H}$ with eigenvalue E_n and C_n is a constant.

3.1.1 Born-Oppenheimer approximation

For a free molecule at rest consisting of N electrons and K nuclei, The Schrödinger equation can be rewritten in terms of the kinetic energy of the electrons and nuclei and the potential energy as

$$\left(-\frac{\hbar^2}{2m}\sum_{i=1}^{N}\nabla_i^2 - \frac{\hbar^2}{2}\sum_{k=1}^{K}\frac{1}{M_k}\nabla_k^2 + V(\mathbf{r},\mathbf{R})\right)\Psi = E\Psi(\mathbf{r},\mathbf{R}) \tag{3.6}$$

the corresponding Hamiltonian is $\hat{H} = \hat{T}_{el} + \hat{T}_{nuc} + V$, where the interaction potential $V(r,R)$ is given by,

$$V(\mathbf{r},\mathbf{R}) = V_{n,n} + V_{n,e} + V_{e,e} \text{ and} \tag{3.7}$$

$$V(\mathbf{r},\mathbf{R}) = \frac{e^2}{4\pi\epsilon_0}\left[\sum_{k>k'}\sum_{k=1}^{K}\frac{Z_kZ_{k'}}{R_{k,k'}} - \sum_{k=1}^{K}\sum_{i=1}^{N}\frac{Z_k}{r_{i,k}} + \sum_{i>i'}\sum_{i'=1}^{N}\frac{1}{r_{i,i'}}\right] \tag{3.8}$$

The first term describes the Coulomb repulsion between the nuclei, the second attraction between electrons and nuclei and the third mutual repulsion between the electrons. Electrons in a molecule move much faster than the nuclei due to their small masses. The electronic motion can be considered decoupled from the nuclear motion. Under this approximation, two separate equations can be written for electrons and nuclei,

$$\hat{H}_0\phi_n^{el}(\mathbf{r}) = E_n^{(0)}\phi_n^{el}(\mathbf{r}) \text{ and} \tag{3.9}$$

$$(\hat{T_{nuc}} + E_n^{(0)})\chi_n(\mathbf{R}) = E_{n,i}\chi_{n,i}(\mathbf{R}) \tag{3.10}$$

Solutions ϕ_n^{el} refer parametrically to the nuclear framework $\boldsymbol{R}$ and the nuclear wavefunctions $\chi_{n,i}(\boldsymbol{R})$ for the state i of the nuclear kinetic energy in the electronic state n. Therefore, the Born-Oppenheimer approximation allows the use of the terms electronic states $|n\rangle$ and the nuclear states $|i\rangle$. As the Hamiltonian $\hat{H} = \hat{H}_0 + \hat{H}'$ can now be expressed as a sum of the electronic and nuclear parts, the total wavefunction $|n, i\rangle$ can be written as a product of an electronic and nuclear wavefunction:

$$\Psi_{n,i}(\mathbf{r}, \mathbf{R}) = \phi_n^{el}(\mathbf{r}) \times \chi_{n,i}(\mathbf{R}). \tag{3.11}$$

This product wavefunction is possible because all interactions between electrons and nuclei have been neglected. Therefore, the total energy is a sum of the kinetic energy of the nuclei and electronic energy averaged over nuclear motion, including the repulsive potential energy between nuclei. The total energy of a molecule in an electronic state $|n\rangle$ is given by,

$$E_n = E_n^{el}(\mathbf{R}) + E_{vib}(\mathbf{R}) + E_{rot}(\mathbf{R}). \tag{3.12}$$

For each electronic state there are a set of vibrational levels characterised by the quantum number v. Each vibrational level in turn contains a multitude of rotational states characterised by the quantum number J. A pure rotational spectrum is obtained when two rotational levels in the same vibrational state are coupled by absorption or emission of a photon. The energy of such a transition lies in the mi-

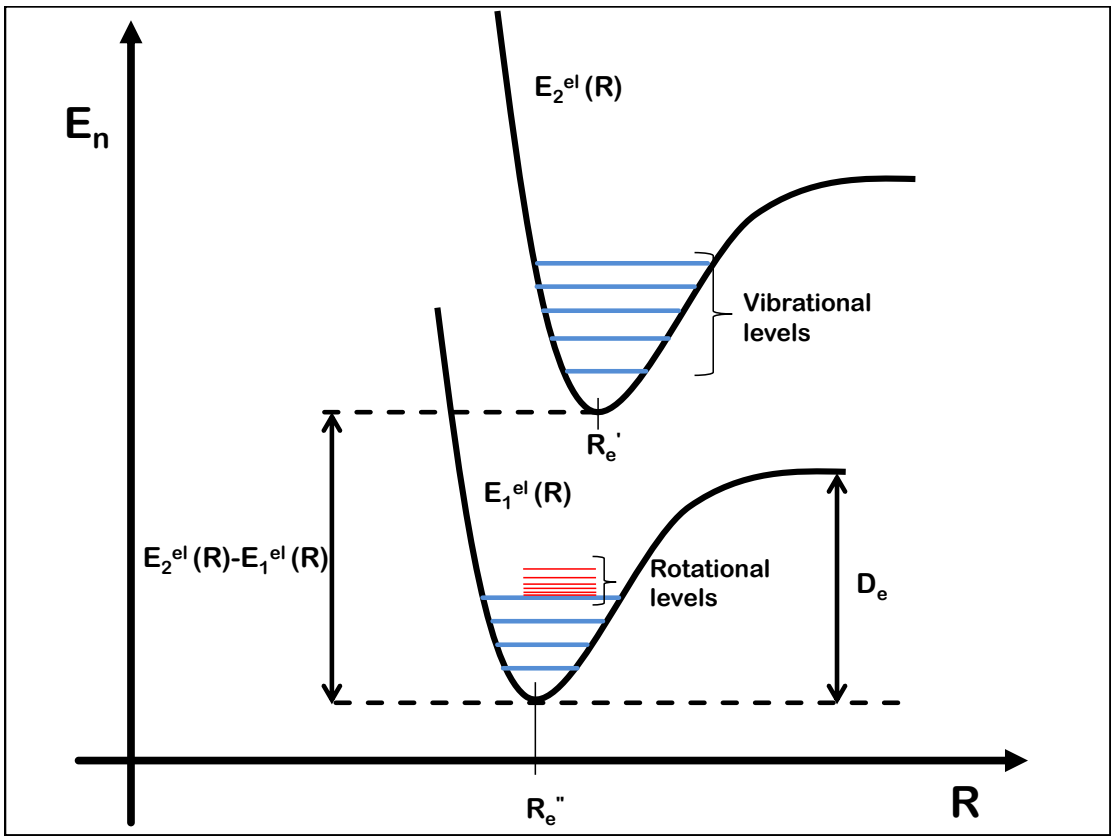

Figure 3.1: Schematic illustration of two electronic states with their equilibrium nuclear distances R_e. The vibrational levels are shown in blue and the rotational in red. For simplicity, the rotational states belonging to only one vibrational level of the ground electronic state have been shown.

crowave region of the electromagnetic spectrum and is of the order of a few tens of wavenumbers. An infrared spectrum is obtained when transitions occur between different vibrational levels of the same electronic state. These are of the order of couple of thousand wavenumbers. An electronic spectrum is obtained when transitions occur between ro-vibrational levels in two different electronic states. The energy required for such excitation can lie anywhere between near infrared to deep UV. All further treatments will be aimed at electronic transitions. Usually, the energy supplied to a molecule to induce an electronic transition is sufficient to excite vibrations and rotations in a excited state.

3.2 Electronic Spectroscopy

For diatomic molecules the ground state is denoted with the letter X. The letters A, B, C, D are used for the lowest excited electronic states with the same multiplicity as X. The letters a, b, c, d,... denote the lowest excited states of different spin multiplicity from the ground state. For polyatomic molecules, the conventions are the same, except that all letters have a superposed tilde; e.g., $\tilde{X}$, $\tilde{a}$,... because the un-accented letters are used for symmetry labels. In molecules, the addition of angular momenta are governed by Hund's rules.

3.2.1 Hund's coupling cases

The orbital angular momentum L, is not a good quantum number for diatomic molecules because of their cylindrical symmetry. Instead, the component of L along the internuclear axis, Λ is defined, which is a sum of the angular momenta of individual electrons, i.e., $\Lambda = \sum_i \lambda_i$. Electronic states with $\lambda > 0$ are doubly degenerate. Electronic states are designated by their value of λ using the Greek equivalents of S, P, D or

Λ	0	1	2	3	...
	Σ	Π	Δ	Φ	...

Depending upon whether the molecular orbital is symmetric (+) or anti-symmetric (−) with respect to reflection across any plane containing the internuclear axis, distinction can be made between Σ^+ and Σ^- states. For $\Lambda > 0$ states $\pm$ formalisms are not used. The subscripts u and g are added to distinguish between functions that are gerade and ungerade upon inversion through the centre of the molecule. The total spin S of the electrons in an electronic state is indicated by the multiplicity $2S+1$ as a superscript. Therefore, the ground state of H_2 is $^1\Sigma_g^+$. It is to be noted that the projection of S along the internuclear axis is also called Σ. For $\Lambda \neq 0$, $\Sigma = S, S-1, \ldots, -S+1, -S$ and the internal magnetic field causes precession in S, coupling the orbital and spin momentum. The total angular momentum is denoted by $\Omega = |\Lambda + \Sigma|$ and appears as a subscript in the term symbol. The complete notation for the coupling of angular momenta in molecules typically is

as follows:

$\mathbf{L}$ = electronic orbital momentum

$\mathbf{S}$ = electronic spin momentum

$\mathbf{R}$ = nuclear rotation momentum (sometimes $\mathbf{N}$)

$\mathbf{J}$ = total momentum of molecules = $\mathbf{L} + \mathbf{S} + \mathbf{R}$

Depending upon the nature of coupling of the above angular momenta, five cases (a)-(e) may be identified. Since, cases (d) and (e) are rarely observed, these will not be discussed any further.

Case (a) The coupling follows the scheme $\Lambda + \Sigma \rightarrow \Omega; \Omega + \mathbf{R} \rightarrow J$. The electronic spin orbit coupling A $\mathbf{L} \cdot \mathbf{S}$ is large, but the nuclear rotation -electron coupling $\mathbf{N} \cdot \mathbf{L}$ is small. Therefore, Ω remains a good quantum number and the energy expression is:

$$F(J) \simeq B_v[J(J+1) - A\Omega^2] \tag{3.13}$$

where $A \gg B_v$. Therefore, the expression is similar to that of a symmetric top. Each Ω state has its own rotational ladder. Case (a) is valid for $^2\Pi$ or $^3\Delta$ states of molecules with first and second row atoms. For the former, there are $^2\Pi_{1/2}$ and $^2\Pi_{3/2}$ states possible, each of which has its own complementary set of rotational levels, split by Λ doubling.

Case (b) Here the appropriate coupling is given by $\mathbf{R} + \Lambda \rightarrow \mathbf{N}; \mathbf{N} + \mathbf{S} \rightarrow \mathbf{J}$. In this case, the electronic spin orbit coupling is small, so the spin couples to the axis of rotation of the molecule. The situation almost always applies to Σ states where $\Lambda = 0$; but it also applies to Π and Σ states in light molecules where the rotational constants are large. $\mathbf{N}$ is the total angular momentum, excluding spin, and the $J = N+S, N+S-1, \ldots |N-S|$ levels with the same N are close together. For example, in a $^2\sigma$ state, the energy levels are:

$$F_1(N) = B_v N(N+1) + 1/2\gamma N \tag{3.14}$$

$$F_2(N) = B_v N(N+1) - 1/2\gamma(N+1) \tag{3.15}$$

where γ is the spin-rotation constant . For higher spin states, the spin-spin interaction must be taken into account.

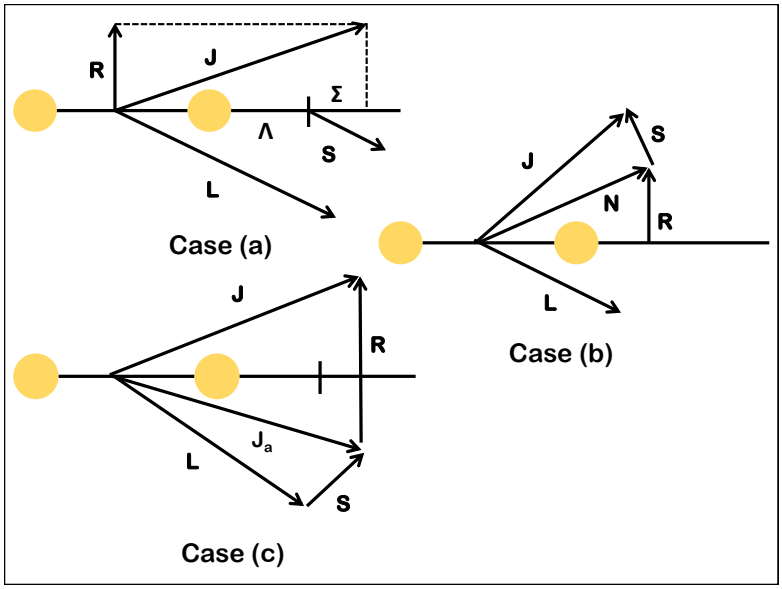

Figure 3.2: Hund' coupling cases (a), (b) and (c).

Case (c) The coupling occurs as $\mathbf{L}+\mathbf{S} \rightarrow \mathbf{J}_a; \sum_a J_a \rightarrow \Omega$ and finally $\Omega+\mathbf{R} \rightarrow \mathbf{J}$. Again, $\mathbf{R}$ is the nuclear rotation, and $R = 0, 1, 2, \ldots$ Λ and Σ are no longer good quantum numbers. This case is observed mostly in molecules with heavy atoms.

3.2.2 Selection rules

The product of the symmetry types of the lower and upper state wavefunctions, and that of the dipole moment operator must be totally symmetric:

$$\Gamma(\Psi_u^{el}) \times \Gamma(d^{el}) \times \Gamma(\Psi_l^{el}) = A_1 \tag{3.16}$$

For diatomic molecules, this results in selection rules for cases (a) and (b):

$$\Delta\Lambda = 0, \pm 1 \tag{3.17}$$

$$\Delta S = 0 \tag{3.18}$$

For case (c), $\Delta\Omega = 0, \pm 1$. For sigma states, the rules are $\Sigma^+ \leftrightarrow \Sigma^+$, $\Sigma^- \leftrightarrow \Sigma^-$, but $\Sigma^+ \nleftrightarrow \Sigma^-$. For homonuclear species, $g \leftrightarrow u$, but $g \nleftrightarrow g$ and $u \nleftrightarrow u$.

The transition frequencies in an actual electronic spectrum are given by:

$$h\nu = (T'_e - T''_e) + G_{v'} + F_{v'}(J) - G_{v''} - F_{v''}(J). \tag{3.19}$$

Here, the vibrational terms are given by G_v and the rotational term values by $F_v(J)$.

3.2.3 Franck Condon Principle

The strength of an electronic transition is proportional to the square of the matrix element between the upper and lower state:

$$R = \langle \Psi' | \mu | \Psi'' \rangle = \int \Psi'^* \mu \Psi'' d(\mathbf{r}, \mathbf{R}) \tag{3.20}$$

where

$$\mu = \mu^{el} + \mu^{nuc} \tag{3.21}$$

is the electric dipole moment operator and the integration is over both electronic and nuclear coordinates. Within the Born-Oppenheimer approximation,

$$\langle e'v' | \mu | e''v'' \rangle = \langle v' \langle e' | \mu^{el} + \mu^{nuc} | e'' \rangle v'' \rangle \tag{3.22}$$

$$= \langle v' \langle e' | \mu^{el} | e'' \rangle v'' \rangle + \langle e' | e'' \rangle \langle v' | \mu^{nuc} | v'' \rangle. \tag{3.23}$$

The second term vanishes because the electronic wavefunctions are orthonormal. If the electronic transition dipole moment is defined as

$$D^{el}(R) = \langle e' | \mu^{el} | e'' \rangle, \tag{3.24}$$

then

$$R = \langle v' | \mu^{el}(R) | v'' \rangle = \int \Psi'_v(R) \mu^{el}(R) \Psi''_v(R) dR \tag{3.25}$$

where the integration is over nuclear coordinates only. The oscillator strength is given by

$$f_{v'v''} = \frac{2}{3} \cdot g |\mu^{el}(R_e)|^2 |\langle v' | v'' \rangle|^2 \Delta E_{v'v''}. \tag{3.26}$$

Thus, the relative intensity of a transition between any two vibrational states is given by the square of the vibrational overlap integral

$$q_{v'v''} = |\langle v'|v''\rangle|^2 \tag{3.27}$$

which is known as the Franck Condon factor. Similarly, one can derive the Hönl-London factors $S_{J'J''}$, which give intensities of rotational transitions between two electronic states. The principles and derivations discussed until now are generally applicable to all types of molecules, although the above development has centred around diatomic molecules. The results presented in this thesis include electronic spectra of linear polyatomics and asymmetric tops. The following treatment will lay the foundation to interpret the rotational structures of the electronic transitions in different types of molecules. Molecules can be classified according to their moments of inertia as follows:

1. Linear molecules: I_A=0; I_B=I_C
2. Spherical tops: I_A=I_B= I_C
3. Prolate symmetric tops: $I_A < I_B$= I_C
4. Asymmetric tops: $I_A < I_B < I_C$

where the axes a, b and c are chosen such that $I_A \leq I_B \leq I_C$. Considering a molecule to be a rigid rotor, the Hamiltonian can then be written in the form:

$$\hat{H} = \frac{\hat{J}_a^2}{2I_A} + \frac{\hat{J}_b^2}{2I_B} + \frac{\hat{J}_c^2}{2I_C}. \tag{3.28}$$

Solution of the Schrödinger equation for a rigid rotor,

$$\left[\frac{\hat{J}_a^2}{2I_A} + \frac{\hat{J}_b^2}{2I_B} + \frac{\hat{J}_c^2}{2I_C}\right]\Psi = E\Psi \tag{3.29}$$

is complicated by the fact that $\hat{J}_a$, $\hat{J}_b$ and $\hat{J}_c$ are the components of J in the fixed-body coordinate system.

3.2.4 Symmetric tops

There are two types of symmetric tops: Prolate symmetric top: $I_A < I_B = I_C$
Oblate symmetric top: $I_A = I_B < I_C$
Using equation 3.28, one can write for prolate symmetric tops:

$$\hat{H} = \frac{\hat{J}^2}{2I_B} + \left(\frac{1}{2I_A} - \frac{1}{2I_B}\right)\hat{J}_a^2. \tag{3.30}$$

The angular momenta $\hat{J}_a$, $\hat{J}_b$, $\hat{J}_c$ are the components of the angular momentum vector $\hat{J}$ along the a, b and c axes which are fixed in the molecule. Lower case letters are used to denote the fixed-body frame while upper cases are used for the laboratory frame. The angular momenta in the fixed-body frame are given by $\hat{J}_x$, $\hat{J}_y$ and $\hat{J}_z$, while those in the laboratory frame are denoted by $\hat{J}_X$, $\hat{J}_Y$ and $\hat{J}_Z$. These two axes systems are relate by Euler angles. The eigenfunctions of $\hat{J}^2$, $\hat{J}_z$ and $\hat{J}_Z$ (symmetric top wavefunctions) are described by the quantum numbers J, K and M, where K is the projection of J on the fixed-body frame and M on the laboratory frame. The final energy term E_{JKM} can then be derived from the relevant Schrödinger equations and can be written as:

$$E_{JKM} = BJ(J+1) + (A-B)K^2 \tag{3.31}$$

$$= BJ(J+1) + (C-B)K^2 \tag{3.32}$$

for prolate and oblate symmetric tops respectively. Each level specified by K, J has a degeneracy of $(2J+1)$ due to various possible values of M. For symmetric tops, each value of K, leads to a stack of levels labelled by J, that are spaced exactly like in linear molecules. The lowest J for each K is given by $J=|K|$ because $|K| \leq J$. In reality, rotation distorts the molecule slightly changing its moment of inertia. Therefore, a more accurate description of the energy levels is provided by,

$$F(J,K) = BJ(J+1) + (A-B)K^2 - D_J[J(J+1)]^2 - D_K K^4 - D_{J,K}J(J+1)K^2, \tag{3.33}$$

where D_J, D_K and D_{JK} are distortion constants.

3.2.5 Asymmetric tops

In these molecules, the final form of the Hamiltonian can be written as,

$$\hat{H} = \frac{1}{\hbar^2}\left[\frac{A+B}{2}(\hat{J^2} - \hat{J_c^2}) + C\hat{J_c^2} + \frac{A-B}{4}((\hat{J^+})^2 + (\hat{J^-})^2)\right], \tag{3.34}$$

where $\hat{J^+} = \hat{J}_x + i\hat{J}_y$ and $\hat{J^-} = \hat{J}_x - i\hat{J}_y$ and $a = x$ and $b = y$. The symmetric top wavefunctions $|JKM\rangle$ are not eigenfunctions of this Hamiltonian because of the presence of $(\hat{J^+})^2$ and $(\hat{J^-})^2$. These couple the function $|JKM\rangle$ to $|JK \pm 2M\rangle$. Even then the symmetric top wavefunctions form a suitable basis for solving the symmetric top problem. With this approximation, the asymmetric top energy levels can be correlated to the prolate and oblate types and the notation $J_{K_aK_c}$ is used. The permanent dipole moment μ, for the electronic state and vibrational level in an asymmetric top may have components along the a, b and c inertial axes. These are designated μ_a, μ_b and μ_c, respectively. The allowed transitions are those that conform to,

$$\Delta J = 0, \pm 1 \tag{3.35}$$

$$\Delta M = 0, \pm 1 \tag{3.36}$$

Therefore, when μ lies along an inertial axis, then only a single type of transition will occur. When it is perpendicular to an inertial axis, it will have components along the two remaining axes and at most two types of transitions are expected.

3.2.6 Polyatomic Franck-Condon factors

The Franck-Condon factor for a diatomic has been discussed earlier. In the case of a polyatomic molecule the treatment is more complicated. This is because the vibrational wavefunction of a polyatomic contains one factor for each normal mode. This is true for both initial and final states. Further, the normal coordinates used to describe vibrations in the ground state are different in the excited state. For molecules in which the symmetry does not change in the excited state, progres-

sions are formed in vibrational modes which are displaced in the two electronic states, which must be totally symmetric modes. If the point group of the molecule changes upon electronic excitation, then one of the non-totally symmetric modes becomes totally symmetric in one of the electronic states.

3.3 Spectroscopic techniques

Regardless of the region of electromagnetic spectrum that molecules are excited in, there are two broad classes of spectroscopic techniques. [1] These are the *direct* and *indirect* methods. The first category revolves around experimental realisation of the well-known Beer-Lambert law and measures attenuation in light intensity. However, a drop in the intensity of an incident beam of photons is only one of several possible consequences of absorption. *Indirect* methods or *action* spectroscopic techniques are based on observation of these phenomena. The more popular methods are described below with a greater emphasis on the approaches that were utilised in the experiments for this thesis.

3.3.1 Absorption Spectroscopy

The attenuation in the intensity of an incident photon beam of a particular wavelength, as it passes through and emerges from a sample of molecules can be measured and constitutes the general principle of absorption spectroscopy. A quantitative picture of the last statement is presented by the Beer-Lambert law, and this is discussed as follows. The law essentially states that absorbance A and number density N of an absorbing species have a linear proportional relation. Mathematically it is written as,

$$A = \sigma N L \equiv \alpha L \tag{3.37}$$

where A (unitless) is the measured absorbance, σ (cm^2) is the absorption coefficient that depends on the wavelength, L (cm) is the path length, N (cm^{-3}) the particle density and α (cm^{-1}) is the attenuation coefficient. Actual measurements

are made in terms of transmittance, T, which is I_L/I_0. A and T are related as follows:

$$A = -lnT = -ln(I_L/I_0) \tag{3.38}$$

The molecule can be approximated by an opaque disk having a surface area σ which is seen by a photon of frequency ν. The constraints added to the following derivation assume that when ν is far from resonance, then σ=0, while on resonance σ achieves a maximum value. To obtain the total absorption cross section over a line one needs to integrate over the full line profile,

$$S = \int_0^\infty \sigma(\nu) d\nu \tag{3.39}$$

I_0 is the intensity entering the sample at z=0, I_z is the intensity entering the infinitesimal section of the solution given by the length dz, dI is the intensity absorbed by this part and I is the intensity leaving the sample. The total opaque area Q on this section due to absorbers is $\sigma NQdz$; consequently the fraction of photons absorbed is $\sigma NQdz/Q$, and hence

$$\frac{dI}{I_z} = -\sigma n dz \tag{3.40}$$

Integrating the above from z=0 to z=L gives

$$ln(I_L) - ln(I_0) = -\sigma NL \tag{3.41}$$

or

$$-ln(I_L/I_0) = \sigma NL \equiv A. \tag{3.42}$$

In exponential form,

$$I(L) = I_0 exp(-\sigma NL). \tag{3.43}$$

The product of the absorption coefficient (σ) and the particle number density (N) is often given by α (cm^{-1}) and is called the attenuation coefficient. The more popular molar absorptivity (ϵ) is given by,

$$\epsilon = \frac{6.023 \times 10^{23}}{2.303 \times 10^{3}} \sigma = 2.61 \times 10^{20} \sigma \tag{3.44}$$

Typical cross-sections and molar absorptivity values are as follows: There are sev-

Table 3.1:

	σ/cm^2 Å	ϵ/ M^{-1} cm^{-1}
Atoms	10^{-12} to 10^{-15}	3×10^{8} to 3×10^{5}
Molecules		
electronic transitions	10^{-14} to 10^{-17}	3×10^{6} to 3×10^{3}
vibrational transitions	10^{-19} to 10^{-21}	3×10^{0} to 3×10^{-2}
Raman scattering	$\sim 10^{-29}$	3×10^{-9}

eral experimental techniques for the application of direct absorption spectroscopy. Two of these which are particularly relevant for this thesis are Matrix Isolation Spectroscopy (MIS) and Cavity Ring Down Spectroscopy (CRDS).

3.3.2 Laser Induced Fluorescence (LIF) Spectroscopy

LIF is spontaneous emission from molecules or atoms that have been excited by laser. When population from the ground state is transferred into the excited one by resonant absorption of a photon, the molecule can dissipate this excess energy in several ways. Spontaneous emission is a dominant loss channel in the absence of collisional quenching and non-radiative pathways. By detecting the emitted photons, usually perpendicular to the excitation source, the electronic spectrum of a molecule is obtained. The fluorescence spectral power density, Φ_F, that is detected from the laser interaction volume can be approximated as:

$$\Phi_F(\nu) = \epsilon h \nu A \frac{\Omega_c}{4\pi} \int_{V_c} n_2 F(\nu) dV_c, \tag{3.45}$$

where ϵ is the efficiency of the collection optics, ν is the frequency of transition, A is the Einstein coefficient for spontaneous emission, $\Omega_c/4\pi$ is the fractional solid angle seen by the collection optics, n_2 is the population transferred to the excited state and $F(\nu)$ is the normalised line shape function. V_c is the focal volume, which is the overlap region between laser beam and collection optics. The fluorescence radiant energy Q_F arriving at the detector is given by an integration over spectral response interval of the detector and the actual fluorescence lifetime.

$$Q_F = \int_{\Delta t} \int_{\Delta\nu_{det}} \Phi_F(\nu) d\nu dt \tag{3.46}$$

Considering n_2 to be a function of time, one can write Q_F as,

$$Q_F = \epsilon h\nu A \frac{\Omega_c}{4\pi} \int_{V_c} \int_{\Delta t} \int_{\Delta\nu_{det}} n_2(t) F(\nu) d\nu dt dV_c \tag{3.47}$$

$$= \epsilon h\nu A \frac{\Omega_c}{4\pi} \int_{V_c} \int_{\Delta\nu_{det}} F(\nu) d\nu dV_c \int_{\Delta t} n_2(t) dt \tag{3.48}$$

$$= C \int_{\Delta t} n_2(t) dt, \tag{3.49}$$

where C is a calibration constant that is determined by geometrical constants and variable.

3.3.3 Light scattering methods

Non-resonant interaction of light with matter results in scattering. This is dependent on the chemical and physical properties of the scattering material and can be elastic or inelastic. The three types of scattering processes are Mie, Rayleigh and Raman. Strength of the scattered signal is dependent on wavelength of the incident laser intensity I_L,

$$I_{scat} \propto C_m \nu_{scat}^4 I_L, \tag{3.50}$$

where C_m depends upon the physical properties of the molecule and the photon frequency is $\nu_{scat} = \nu_L$ in the case of Rayleigh scattering or $\nu_{scat} = \nu_L \pm \nu_{Raman}$

in case of Raman scattering. For the latter, polarisability of the molecule is the property that is probed. Only the latter provides information specific to a molecule and will be considered further. Raman scattering can be generalised as,

$$\nu_{Raman} = h\nu_L + \Delta E_{vib,rot}, \tag{3.51}$$

where $\Delta E_{vib,rot}$ is the energy difference between the state from which the scattering process started and the where the molecules ends at the end of the process. Depending on whether the scattered Raman photon has lesser or greater energy than the incident photon, the phenomenon is called Stoke's or anti-Stoke's shift. The line intensities for Stoke's, I^S_{nm}, and anti-Stoke's, I^{AS}_{nm}, transitions are given by,

$$I^S_{nm} = \frac{2\pi^2 h}{c^4} \frac{(\nu_L - \nu^4_{vib,rot})}{\nu_{vib,rot}[1 - exp(-h\nu/kT)]} g_\nu (\frac{\partial\alpha}{\partial Q})^2 \tag{3.52}$$

and

$$I^{AS}_{nm} = \frac{2\pi^2 h}{c^4} \frac{(\nu_L + \nu^4_{vib,rot})}{\nu_{vib,rot}[exp(h\nu/kT) + 1]} g_\nu (\frac{\partial\alpha}{\partial Q})^2, \tag{3.53}$$

where g_ν is degeneracy of the vibrational levels involved and n and m are the initial and final states. The partial derivative $\frac{\partial\alpha}{\partial Q}$ signifies that the polarisability α of the molecule should change along the nuclear coordinates Q. Therefore, for a Raman transition to be observed, this derivative should be non-zero.

3.3.4 Ionisation Spectroscopy

Resonance Enhanced Multiphoton Ionisation or REMPI is a method in which a molecule is first excited by a photon to an intermediate state, from where it absorbs one or more photon(s) of the same or different colour to undergo ionisation. The ions are then detected as a function of the first photon energy to yield spectrum of the neutral. Schematically, the process occurs as:
$AB(v'', J'') \xrightarrow{h\nu_1} AB^*(v', J')$

$AB^* \xrightarrow{h\nu_2} AB^+ + e.$

Theoretically, the signal intensities can be approximated by the following equation,

$$I = C\frac{N(v'', J'')}{2J'' + 1} q_{v',v''} S(J', J'') \tag{3.54}$$

In equation 3.54, the population of ground state (v'', J'') levels is $N(v'')$ with $(2J'' + 1)$ being the degeneracy. The Franck-Condon factor and rotational line strength are given by $q_{v',v''}$ and $S(J', J'')$, respectively, between the ground the intermediate electronic state. The factor C is dependent on rotational and vibrational quantum numbers and is proportional to the intensities of both lasers, the absorption cross section of the molecule and the quantum yield for ionisation.

3.3.5 Spectroscopy by Laser Induced Reactions

Trapped ions are suitable candidates for spectroscopic probing by laser induced chemical reactions (LIR). [2] The basic concept revolves around enhancing the rate of a reaction that is extremely slow when the ion is its vibrational ground state. An example of chemical probing without laser is the reaction between metastable HOC^+ and CH_4. The ground state HCO^+ counterpart does not show proton transfer because of endothermicity. By detecting CH_5^+ ions one can estimate the number of metastable HOC^+ present in the trap. In LIR, chemical probing of the trapped ion becomes possible due to varying rate coefficients in the ground and excited states.

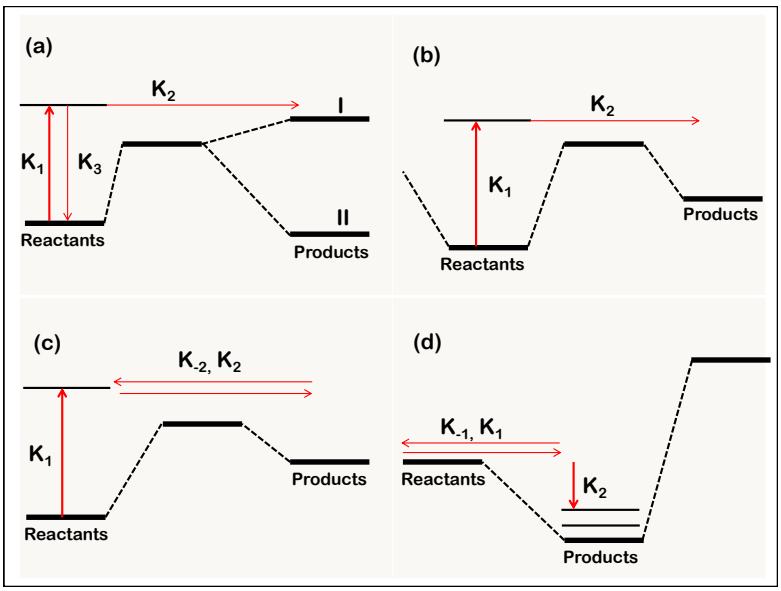

Figure 3.3: Schematic illustration of model systems suitable for LIR spectroscopy. (a) excitation of a ro-vibrational state leads to bimolecular reaction, (b) Vibrational predissociation spectroscopy, (c) laser induced shift of the equilibrium of a bimolecular reaction, (d) stimulated association of a molecule.

Vibrational spectrum of $C_2H_2^+$ in the C-H stretching region and the antisymmetric cis-bending vibration have been measured by LIR. [3] The photon induced isotopic exchange of a hydrogen with deuterium has been used to measure the $1_{01} \leftarrow 0_{00}$ transition of para-H_2D^+ and $1_{11} \leftarrow 0_{00}$ of ortho-D_2H^+. [4] Another notable application of this method is the measurement of the vibrational spectrum of CH_5^+. [5]The following reaction, endothermic by 3 kJ mol^{-1} was used:

$$CH_5^+ + CO_2 \rightarrow CH_4 + HCO_2^+. \tag{3.55}$$

This is an experimental example of scheme (a) in Figure 3.3. The rate at which the products are formed is given by,

$$K = K_1 \cdot \frac{K_2}{K_2 + K_3}. \tag{3.56}$$

Here, $K_1 = B \cdot g \cdot \rho$ where B is the Einstein coefficient, g is the population of the lower state and ρ is the power density of the laser. The reaction rate, $K_2 = k_2 \cdot [CO_2]$, where k_2 is the rate coefficient and $[CO_2]$ is the number density of carbon dioxide neutrals introduced into the trap. Similarly, the quenching rate is given as, $K_3 = k_3 \cdot [CO_2] \cdot A$, where A is the Einstein coefficient for emission. Numerical simulations have allowed the approximation, $k_L \sim k_{col} = k_2 + k_3$. The denominator in equation 3.56 can be re-written as $A + k_{col} \cdot [CO_2]$. In the high pressure regime, $A \gg k_{col}[CO_2]$ and taking all this into account,

$$K = \frac{k_2}{k_{col}} \cdot B \cdot \rho \cdot g. \tag{3.57}$$

Assuming there are no other competing reactions, the number of product ions is given as:

$$[HCO_2^+] = [CH_5^+] \frac{k_2}{k_{col}} \cdot B \cdot \rho \cdot g \delta t \tag{3.58}$$

This simple approach has been found to be sufficient to compare experimental LIR spectra with theoretical ones. Similarly, the reaction

$$N_2^+ + Ar \rightarrow N_2 + Ar^+ \tag{3.59}$$

has been used to measure rotationally resolved electronic spectrum of N_2^+. Ar^+ ions were counted as a function of the laser wavelength to generate the spectrum. [6] This is an example of asymmetric charge transfer between a gaseous ion and an atom at low velocity. [7] A rigorous understanding would require a wavemechanical treatment of collisions. The attractive potential, V, between an ion and atom at a large distance is given by $-\frac{\alpha q}{2R^4}$, where α is the polarisability of the neutral and R is the distance between the ion and the atom. The trajectories of the atom about the ion as a function of impact parameter, b, belong to two categories. Some of these produce impact and some result in grazing incidence. The cross section for impact collisions is given by,

$$\sigma = \left(\frac{2\pi q}{v}\right) \sqrt{\left(\frac{\alpha}{\mu}\right)} \tag{3.60}$$

where v is the relative velocity and μ is the reduced mass. In terms of potential energy surfaces, charge transfer occurs through curve crossing. There must exist an appreciable overlap between the vibrational wavefunctions of the excited ion and the product ion. In addition, the Franck-Condon factors between the neutral and its ionic state should be favourable as well.

3.3.6 Photodissociation Spectroscopy (PDS)

Photodissociation in various ways has been applied successfully in measuring spectra of molecular ions that can only be created in small number densities in the gas phase. The guiding principle is that an ion dissociates only when it absorbs a photon. Therefore, measuring photodissociation probability or cross section as a function of exciting wavelength is expected to be a reliable reflection of the optical spectrum of an ion. [8] Much of the application of PDS has been dedicated to radical or odd-electron ions. This is because of two major reasons. Closed-shell species have very low reactivity and can therefore be studied in solution while any interaction of an open shell molecule with the surrounding environment will lead to a an immediate reaction. Secondly, there is rich spectroscopy of radical ions in the visible and UV because of the inner shell promotions possible to the half empty HOMO from the lower lying filled orbitals. Dissociation spectroscopy by multiple infrared photons has been extensively used as well to characterise vibrational transitions in a wide variety of molecules. [9] One of the biggest advantages of this method lies in the fact that it is an essentially background free technique. Fragments are formed only when an absorption event occurs. In the UV/Vis region, absorption of a single photon is often sufficient to induce dissociation. These mechanisms are shown. On the left of Figure 3.4, absorption of a photon couples the lower state to a repulsive state and the spectrum is expected to be broad without discernible features. This is seen in $S_1 \leftarrow S_0$ electronic transition of protonated benzene. On the other hand, the predissociation spectrum should reveal details of the rotational structure of the excited state. This is indeed the case as has been observed for the $A^2\Sigma^+ \leftarrow X^2\Pi_{3/2}\ 1_0^2$ electronic spectrum of N_2O^+. This

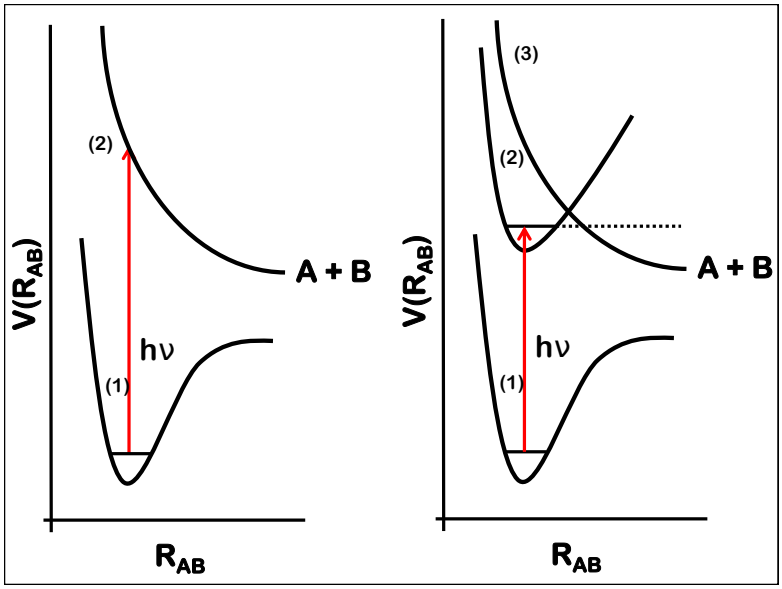

Figure 3.4: Schematic representation of electronic direct dissociation and predissociation. In the latter, the molecule undergoes non-radiative transition from the bound state (2) to the repulsive state (3) and subsequently decays.

is known as Herzberg type I predissociation. Radiationless transition from (2) to (3) can occur via internal conversion or intersystem crossing. Two other types of predissociation are shown in Figure 3.5. In Herzberg type II predissociation, the molecule AB lies on the excited state surface above the threshold for dissociation, but there exists a barrier. The excited state is quasi-bound and is called a resonance. The molecule overcomes the barrier either via tunnelling or redistribution of internal vibrational energy. In type I, the dissociation lifetime is determined by the nature of coupling of the electronic states and in type II, the tunnelling rate or the efficiency of energy transfer is the deciding factor. [10]

Figure 3.6 shows the schematic for a two photon dissociation process. Usually, the energy transferred to the molecule by the first photon undergoes some form of redistribution before the arrival of the second photon. In most cases the excited state population undergoes both radiative and non-radiative processes and eventually occupy the excited vibrational levels of state (1). In some molecules, a close lying state with a different spin state may also trap some part of the population.

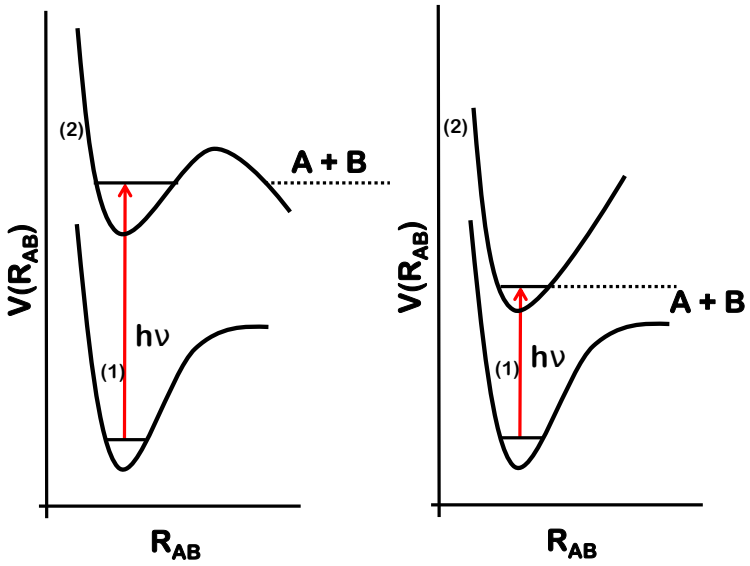

Figure 3.5: The left panel shows mechanism of Herzberg type II predissociation. Fragmentation in the right panel happens after population transfer to vibrationally excited levels of state (1).

Therefore, in two colour two photon processes, it is very seldom that the second photon is absorbed from the final state of the first excitation. [11,12] The kinetics of the excitation dissociation scheme can be understood as follows: Figure 3.7 summarises the discussions above in terms of rate constants of excitation, relaxation and dissociation steps. A-H$^+$ corresponds to an ensemble of trapped ions that have undergone equilibration to the trap temperature via collisions with helium atoms. A nano-second laser in the visible, corresponding to a photon frequency of ν_1 induces an electronic excitation to form [A-H$^+$]**. I is the intensity and the absorption cross section is σ_1. The excited ion then undergoes a fast internal conversion to higher vibrational levels of the electronic ground state. The [A-H$^+$]* ions so formed absorb a second photon, usually in the UV to undergo dissociation. Usually collisional quenching with helium and radiative relaxation by emission of infrared photons are competing processes. The former is dependent on the helium number density, [He]; while k_3 and k_r are the rate constants for bimolecular collisions with helium and radiative decay respectively. When an ion absorbs two photons simultaneously from the same laser, then these two pathways do not play

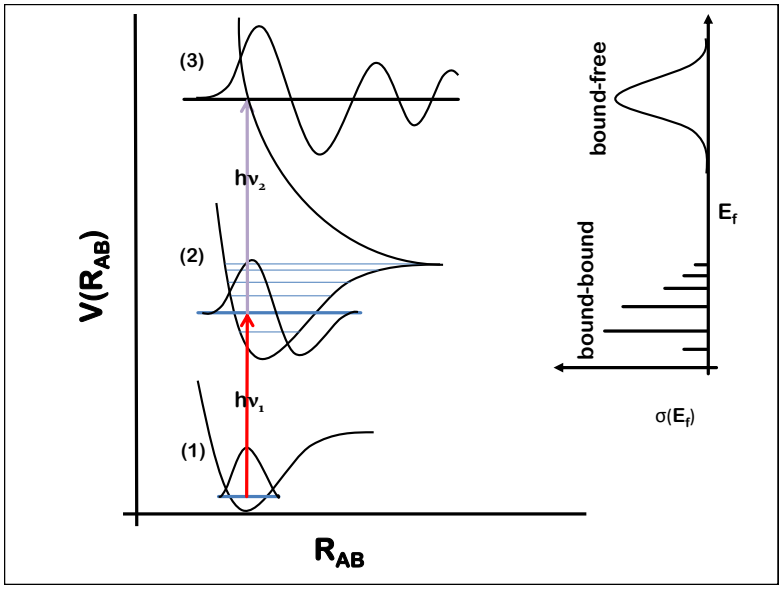

Figure 3.6: Schematic representation of a two photon process. The first photon promotes transition to a higher electronic state, the second photon initiates fragmentation. A transition from state (1) to state (3) would have resulted in the structureless band as shown on the right. Using state (2) as an intermediate allows mapping of the ro-vibrational levels in it. This results in a more detailed spectrum.

any role in the fragmentation rate. When the two photons have a time delay, then dissociation yields are determined by an interplay between relaxation and excitation schemes. This can be exploited experimentally to evaluate time evolution of the excited state inside the trap and estimate efficiency of non-radiative pathways.

3.4 Line-Shape functions

An experimental spectrum contains absorption featured that are called lines that constitute a band associated with a normal mode. These lines have definite widths and characteristic shapes. Only those factors that were relevant under the experimental conditions used in this thesis are discussed here. [13]

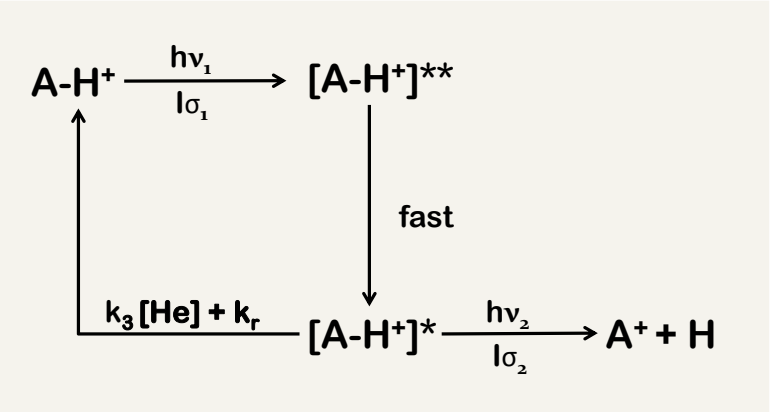

Figure 3.7: Rate processes involved in two photon dissociation schemes. See text for details.

3.4.1 Natural Lifetime Broadening

When an atom or molecule undergoes absorption to be promoted to an excited state, it can spend only a finite length of time there. An excited particle can be pictured as an oscillating dipole that radiates power at a rate proportional to $|\mu_{10}|^2$, where the subscripts denote the states between which emission occurs. The normalised line shape function can then be shown to be,

$$g(\nu - \nu_{10}) = \frac{\gamma}{(\gamma/2)^2 + (2\pi)^2(\nu - \nu_{10}^2)} \tag{3.61}$$

where, $\gamma = 1/\tau_{sp} = \mathrm{A}_{1\to 0}$ and ν is the frequency. In the absence of spontaneous emission, the lineshape function would be $\delta(\nu - \nu_{10})$ because the cosine wave representing the dipole oscillates at a frequency ν_{10}. Spontaneous emission leads to a decay in the cosine wave giving a Lorentzian function of finite width. The full width half maxima (FWHM), $\Delta\nu_{1/2}$ is then given by,

$$\Delta\nu_{1/2} = \frac{\gamma}{2\pi} = \frac{1}{2\pi\tau_{sp}} \tag{3.62}$$

The lineshape function in terms of the FWHM then transforms as,

$$g(\nu - \nu_0) = \frac{\Delta\nu_{1/2}/(2\pi)}{(\Delta\nu_{1/2}/2)^2 + (\nu - \nu_0)^2}. \tag{3.63}$$

Spontaneous emission therefore limits the time that an atom or a molecule that can exist in the excited state.

3.4.2 Doppler Broadening

When an atom or a molecule moving with velocity **v** interacts with a plane wave with a wave vector **k**, then it sees a Doppler shifted frequency $\nu' = \nu(1 \pm \frac{v}{c})$. To obtain a line shape function, one needs a distribution of velocities. The Maxwell-Boltzmann distribution function,

$$p_v dv = \left(\frac{m}{2\pi kT}\right)^{1/2} e^{-\left(\frac{mv^2}{2kT}\right)} dv \tag{3.64}$$

gives the distribution of molecular velocity components along a given axis, **k**, in a gaseous system for particles of mass m and at temperature T. The normalised inhomogeneous lineshape function is then given by,

$$g_D(\nu - \nu_0) = \frac{1}{\nu_0}\left(\frac{mc^2}{2\pi kT}\right)^{1/2} e^{-\frac{mc^2(\nu-\nu_0)^2}{2kt\nu_0^2}}. \tag{3.65}$$

The FWHM $\Delta\nu_D$ is then given as,

$$\Delta\nu_D = 2\nu_0\sqrt{\frac{2kTln2}{mc^2}} \tag{3.66}$$

or

$$\Delta\tilde{\nu_D} = 7.1 \times 10^{-7}\tilde{\nu_0}\sqrt{\frac{T}{M}}, \tag{3.67}$$

where T is in K, M in amu, $\tilde{\nu}_0$ and $\tilde{\nu}_D$ in cm^{-1}.

3.4.3 Power Broadening

The use of high power lasers in spectroscopic measurements leads to line broadening and splitting. A simple estimate of the linewidth can be made from Heisenberg's uncertainty principle,

$$\Delta E \Delta t \geq \hbar. \tag{3.68}$$

A molecule undergoes Rabi oscillation at high powers at an angular frequency of $\omega_R = \mu_{10}E/\hbar$. The length of time that the molecule then is in the excited state is $h/\mu_{10}E$. Therefore,

$$\Delta E \frac{h}{\mu_{10}E} \sim \hbar \tag{3.69}$$

or

$$\Delta\nu \sim \frac{\mu_{10}E}{2\pi h} = \frac{\omega_R}{4\pi^2}. \tag{3.70}$$

Bibliography

[1] H. H. Telle, A. G. Urena, and R. J. Donovan. *Laser Chemistry: Spectroscopy, Dynamics and Applications.*

[2] S. Schlemmer and O. Asvany. Laser induced reactions in a 22-pole ion trap. *Journal of Physics: Conference Series*, 4:134, 2005.

[3] S. Schlemmer, E. Lescop, J. von Richthofen, and D. Gerlich. Laser Induced Reactions in a 22-Pole Trap: $C_2H_2^+ + h\nu_3 + H_2 \rightarrow C_2H_3^+ + H$. *J. Chem. Phys.*, 117:2068, 2002.

[4] O. Asvany, O. Ricken, H. S. P. Müller, T. Giesen, M. Wiedner, and S. Schlemmer. High-Resolution Rotational Spectroscopy in a cold Ion Trap: H_2D^+ and D_2H^+. *Phys. Rev. Lett.*, 100:233004, 2008.

[5] O. Asvany, P. Kumar, P. B. Redlich, I. Hegemann, S. Schlemmer, and D. Marx. Understanding the Infrared Spectrum of Bare CH_5^+. *Science*, 309:1219, 2005.

[6] S. Schlemmer, T. Kuhn, E. Lescop, and D. Gerlich. Laser excited N_2^+ in a 22-Pole trap, Experimental Studies of Rotational Relaxation processes. *Int. J. Mass Spectrom. Ion Proc.*, 185:589, 1999.

[7] D. Rapp and W. E. Francis. Charge Exchange between Gaseous Ions and Atoms. *J. Chem. Phys.*, 37:2631, 1962.

[8] R. C. Dunbar. Photodissociation of trapped ions. *Int. J. Mass Spectrom.*, 200:571.

[9] T. Baer and R. Dunbar. Ion Spectroscopy: Where Did It Come From; Where Is It Now; and Where Is It Going? 21:681, 2010.

[10] Tutorials in Molecular Reaction Dynamics, 2010.

[11] A. Dzhonson, D. Gerlich, E. Bieske, and J. P. Maier. Apparatus for the study of electronic spectra of collisionally cooled cations: para-dichlorobenzene. *J. Mol. Struct.*, 795:93, 2006.

[12] A. Dzhonson, E. B. Jochnowitz, and J. P. Maier. Electronic Gas-Phase Spectra of Larger Polyacetylene Cations. *J. Phys. Chem. A*, 111:1887, 2007.

[13] P. F. Bernarth. *Spectra of Atoms and Molecules*. 1995.

4 Experimental

According to Jean H. Futrell,

> *Tandem mass spectrometry is the branch of mass spectrometry concerned with selection of a particular ion (a component of the normal mass spectrum) formed from a molecule or a mixture of molecules and its activation, usually by one or more collisions, to generate characteristic secondary fragment ions. The motivation may be analytical, determination of ion structure(s), fundamental studies of properties of ions, or any combination thereof.*

Tandem mass spectrometry has a rich and long history and it has been applied to a broad range of fields. The following table provides an overview of the development of this technique over the years as applied primarily to characterisation of protein molecules. In the early years, sector magnets were used as mass filters. Ions were activated inside gas filled cells by collisions. During the 1960s, one of the first departure from magnetic sector technologies appeared when quadrupole mass filters were used. Thereafter, an RF only quadrupole was used as a collision cell. This proved a significant improvement because it increased ion transmission and resulted in much higher collision efficiency.

In 1974, Teloy and Gerlich discussed several limitations of tandem setups. [1] They showed that by using inhomogeneous oscillatory electric fields for production, guidance and collection of ions, many of these associated problems could be overcome. An octopole was experimentally realised for the first time and this opened up the possibility of new experiments with very well-defined ion energies down to tens of millivolts. Although used initially for studying reaction dynamics

Table 4.1: Tandem mass spectrometry over the years

Year	Development
1947	Hipple uses mass spectrometer to measure half-lives of metastable ions
1953	Lindholm uses mass spectrometer to determine products of ion-molecule collisions
1963	Lindholm studies charge-exchange processes in acetylene and slow positive ions with double mass spectrometer
1966	Futrell and Miller describe tandem MS utilising two double focusing instruments
1967	Cooks' group begins extensive study of mass spectra of organic compounds undergoing electron ionisation
1969	Clow and Futrell study charge-exchange in xenon methane mixtures by ion cyclotron resonance technique
1971	Beynon and Cooks describe Ion Kinetic Energy Spectrometry (IKES)
1973	Westal, Futrell and ryan adapt Bendix time of flight instrument for study of unimolecular decay processes
1974	Futrell' group begins study of crossed beam ion molecule reactions
	Vestal and Futrell use tandem quadrupole to study photodissociation in mono-halogenated methyl ions.
1976	Cooks' group describes mixture analysis of organic compounds by mass analysed ion kinetic energy spectrometry
1978	McLafferty and Bockhoff use tandem mass spectrometer to analyse mixtures of organic compounds directly
	Kondrat and Cooks describe mixture analysis of drugs and biomolecules by MIKES
1982	Gross et al describe high resolving power EBE triple analyser
1985	Marshall and co-workers describe 'tailored' excitation for FT-ICR MS
1987	Cooks'group describes tandem quadrupole for study of surface-induced dissociation
1988	McLafferty: tandem double focusing MS for neutralisation-reionisation and collisional activation studies
1990	Cooks: Collisionally activated dissociation of peptides with a quadrupole ion-trap MS
1995	Little and McLafferty: Sequencing 50-mer DNAs with ESI tandem mass spectrometry

over a wide range of collision energies, the last fifteen years has seen the advent of temperature variable multipoles as invaluable tools for performing spectroscopy on ions. The familiar principles of tandem MS have been retained in such that mass selected parent ions are subjected to laser interrogation followed by mass analysis of the product ions. The important difference lies in the use of a multipoles as ion traps. Although conventional Paul traps use a fast oscillating quadrupole field to confine ions in three dimensional space, the wide field free regions offered by the higher orders of multipoles are preferred. Different types of multipole geometries that have been used include octopole, [2], hexadecapole [3] to the more common 22-pole. Such traps offer long confinement times, which make it possible to carry out spectroscopy by indirect means even with a few thousand ions.

All the experiments reported in this thesis were performed on ions confined in a 22-pole. After the parent ions were produced in an ion source, they were mass filtered by a quadrupole, held in the trap for a defined length of time and then probed with laser radiation. Several schemes of spectroscopy were employed, all of which led to the production of daughter ions of some form which were analysed by a second quadrupole mass filter. A suitable detector was then used to count the

ions. The basic construction of the experimental setup is shown in Figure 4.1. All

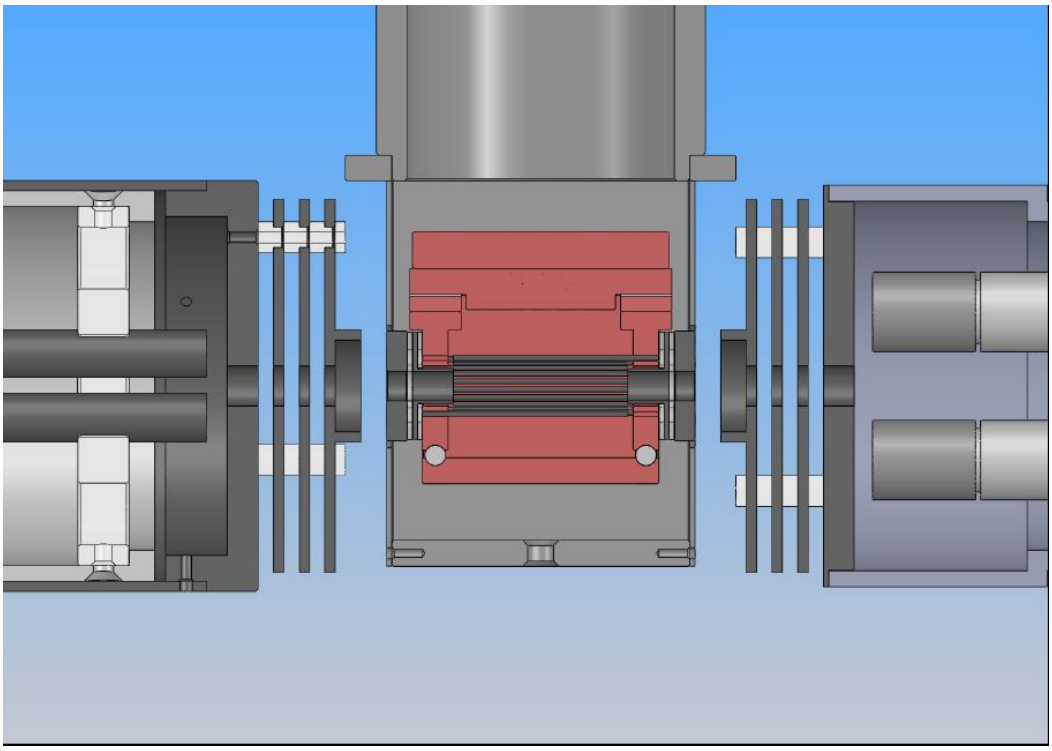

Figure 4.1: The apparatus.

devices mentioned above necessarily require good vacuum conditions for primarily two purposes. In order to work with ions, one must ensure that the neutral density inside the chambers are as low as possible (¡$10^8\,\mathrm{cm}^{-3}$). Turbomolecular pumps are used to maintain extremely low pressures($\sim 10^9$ mbar) in the chambers. Typically, the chambers that house the source, quadrupoles, the trap and detector are all equipped with their own pumps. These pumps are then backed by another booster pump. Several elements inside the machine, especially the quadrupoles and the detector use high voltages (several kV). Low pressures are essential to prevent arcing and ensure proper operating conditions for these parts.

4.1 Ion source

A variety of sources are available to produce ions and choosing a particular type depends upon several criteria:

1. The source should be able to ionise a wide variety of species.
2. Ion generation mechanism should deposit as less excess energy into the ion as possible. Internally excited molecular ions are likely to disintegrate upon collision with background gas.
3. Since higher orders of mulltipoles have shallow potential wells, for experiments related to trapping in them, the ions should have low kinetic energy and the distribution should be narrow.
4. The ion beam should be stable over several hours to allow consistent experimental conditions.
5. The design of the source should be relatively simple to allow easy and regular maintenance as it is likely to get dirty quite frequently.

Some of the most commonly used ion sources that satisfy one or more of the above conditions to varying extents are as follows:

1. **Electro-spray source**
   John Fenn was awarded the Nobel Prize in 2002 for the development of the electro-spray source and its coupling with a mass spectrometer. This device has proved very useful in bringing biological molecules into the gas phase without destroying them. Very low concentrations of the solute can be employed and the solvent is usually polar, volatile and has a low viscosity. In this source, gaseous ions are created by spraying a solution of the appropriate sample from the tip of a needle that is held at several kilovolts. Highly charged droplets are formed at the tip of the needle which limits the formation of bigger aggregates. The droplets break down further as solvent molecules evaporate.

2. **Laser vaporisation source**

   A laser beam is focussed on a metal target which causes vaporisation of the metal and subsequently induces multi-photon ionisation. This plasma then interacts with a suitable gas mixture to produce the desired ions. One other variety of this type is the laser ablation source, which replaces a metal rod with, for example, a graphite plate leading to the formation of carbon chains.

3. **Electron impact**

   The electron impact source is a combination of the molecular beam apparatus and an electron gun. The former can be either pulsed or continuous. Ionisation is achieved by an electron beam that is perpendicular to the beam of neutrals.

The basic operating principle of the source used for the experiments in this thesis, is similar to the electron impact source. However, a separate electron gun was not used. An effusive beam of neutrals was created either by introducing the appropriate neutral gas into vacuum directly or by heating in case of insufficient vapour pressure. These molecules were then ionised by bombardment with electrons generated from thermoionic emission from a filament. The source proved to be quite efficient in creating carbon chain cations and proved to especially useful in synthesising higher chains starting from the smaller ones. However, there were some limitations as well. Because of the rather open construction, the neutral vapours could escape and very often condensed on cooler parts of the chamber. Accumulation of such residue on ion optics would result in charging effects that influenced the efficiency of ion transmission. The high density of neutrals, ions and electrons in the ionisation region limited the lifetime of the filament to a couple of weeks. The mechanism of ion formation was not always well understood and the source was not efficient in creating certain types of ions. To exemplify, the odd carbon chains with the general formula $HC_{2n+1}H^+$ were never observed. Besides, protonated polyaromatic hydrocarbons could not be synthesised.

4.1.1 Basic elements

An electron bombardment source to produce cations can be assembled in a number of different ways to cater to specific needs. The basic elements of such a source remain the same. This section describes these parts.

The central element of the source is a filament, which is electrically heated to emit electrons. Both thoriated-tungsten and rhenium filaments have been used. The latter appeared to be more robust; however, it was never tested rigorously with hydrocarbon neutrals. The filament is held in place by four holders (3) which are

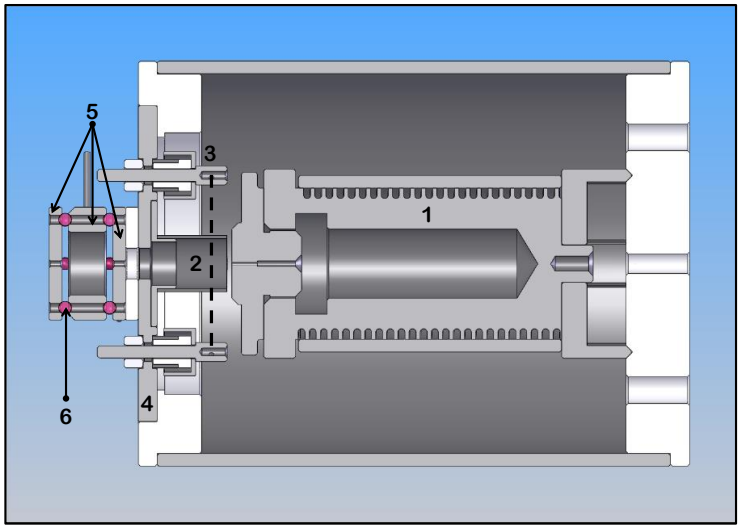

Figure 4.2: The electron bombardment ion source. 1 Oven, 2 Grid, 3 Holder with filament, 4 Base plate, 5 Extraction electrodes, 6 Ruby ball. All the parts in white are ceramic

electrically insulated from the supporting base plate by ceramic spacers. Screws are used to hold the filament in a compact arrangement. The filament runs around a meshed grid (2) which is held at a slightly positive potential with respect to the reference. The voltage applied to the grid eventually determines the kinetic energy of the ions. Best operating conditions are achieved when this is maintained on 0 V. The preferential direction of flow of electrons from the filament to the grid is determined by the gradient created by applying a negative potential to the

former. Neutral vapours undergo collisions with the electrons to produce ions. The temperature in this part reaches in excess of 500 K because of energy radiated from the heated filament. This region has a high density of electrons and ions often resulting in complicated chemistry giving rise to a plethora of ions. This caused the filament to undergo rapid degeneration under such extreme conditions. Often the employed temperatures were much higher to vaporise hydrocarbons with very small vapour pressures. Typically, a filament had to be replaced after two weeks of operation.

A stack of three electrodes (5) was used to extract positively charged molecules out of the ionisation region and inject them into the next part of the machine.

The source was equipped with an oven (1) as well. Hydrocarbons like large polyaromatics have vanishing vapour pressures even at 200 K. Such molecules have to be heated to quite high values of temperature to maintain a steady flow of neutrals to the ionisation zone. The oven is made from stainless steel. It is 5.5 cm long and has a diameter of 2.5 cm. A twin core heating element is wrapped around the oven. The current flows through it in both directions nullifying any magnetic field. The oven can reach temperatures of 1000 K. This was measured by a thermocouple that was introduced through a hole drilled into the external stainless steel shield.

4.1.2 Later modifications

A conical part that projected partially into the grid was added to the first extraction electrode. This created a field penetration that facilitated the transport of ions into the extraction zone. The third electrode was modified to have a similar design with the conical part projecting into the next element of the machine. A repeller plate, parallel to the base plate, was also added behind the grid. A positive potential was applied to it force the ions that escaped in the other direction towards the extraction electrodes. An improvement on this design could be made by encasing the entire ionisation assembly in a closed cylinder held at a positive potential.

4.2 Quadrupole mass filters

The theory behind mass selection using quadrupole mass filters has been discussed in Chapter 2. The present apparatus utilises two quadrupoles. The first one selects the ion of interest from the several species produced in the source. The second one is necessary for mass analysing the ionic products formed in the trap. A set of electrodes on either end of the quadrupole rod assembly, is utilised to transport ions into or from the quadrupole. Figures 4.3 and 4.4 show the two quadrupoles used for majority of the experiments in this thesis.

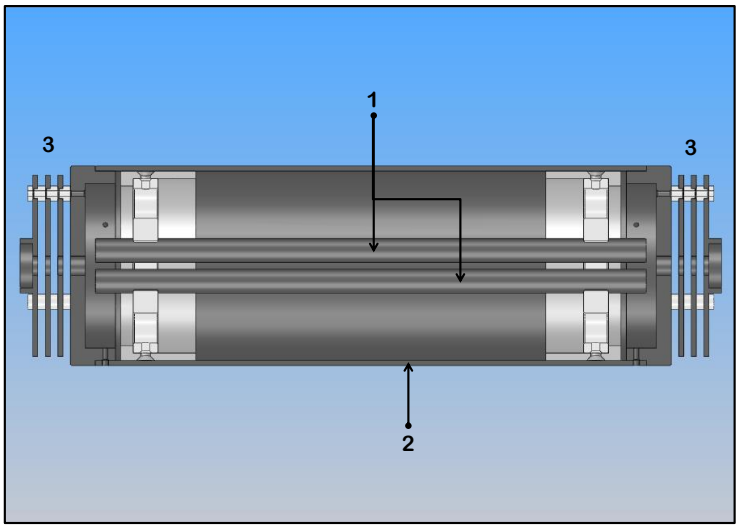

Figure 4.3: The first quadrupole. 1 Rods, 2 Surrounding shield, 3 Electrodes.

The rods used for the first quadrupole were built and assembled in-house. The rods have a diameter of 9.5 mm and are 220 mm long. The rf-power supply (model 150QC) provides 300 W at 1.2 MHz. The DC power supply is a model U-1272 and both are from Extranuclear. This quadrupole was tuned to reach a maximum of 800 Daltons. The second quadrupole is a commercial unit from Nermag. The rods are 15.5 mm wide and 364 mm long. The operating frequency was 880 kHz which gave a mass range of 2000 Daltons. Both the quadrupoles were housed inside shields that had holes or sections cut out to allow pumping.

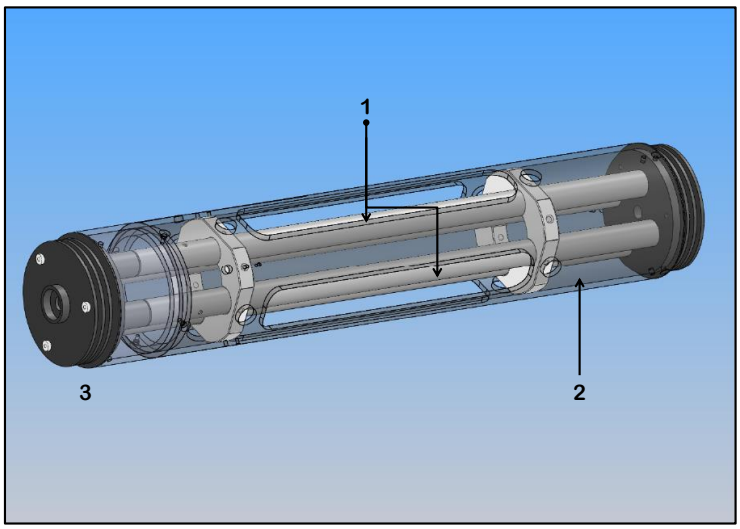

Figure 4.4: The second quadrupole. 1 Rods, 2 Surrounding shield, 3 Electrodes.

4.3 22-pole trap

4.3.1 Trapping ions

Before going into more details about the 22-pole trap used for these experiments, some typical values for multipoles are summarised in the table below. The following table uses a hexapole and a 22-pole, because these are the two that have been used during the course of this thesis. N_2^+ was the ion of choice, so m/z = 28 in the following calculations.

Table 4.2: Characteristic dimensions and parameters for the multipoles used in this thesis:

n	r_0/mm	R_0/mm	$\Omega = 2\pi f$/MHz	V_0/V	η	V^*	ϵ
3	2.5	5	$2\pi\times3$	100	0.38	3.7	138.17
11	0.5	5	$2\pi\times5$	50	0.21	0.32	28.54

A hexapole was used principally as an ion guide to transport ions from the source to the quadrupole. Its utilities have been discussed later in the section

dealing with different configurations that were used for the setup. Figure 4.5 shows the potential function corresponding to a hexapole field.

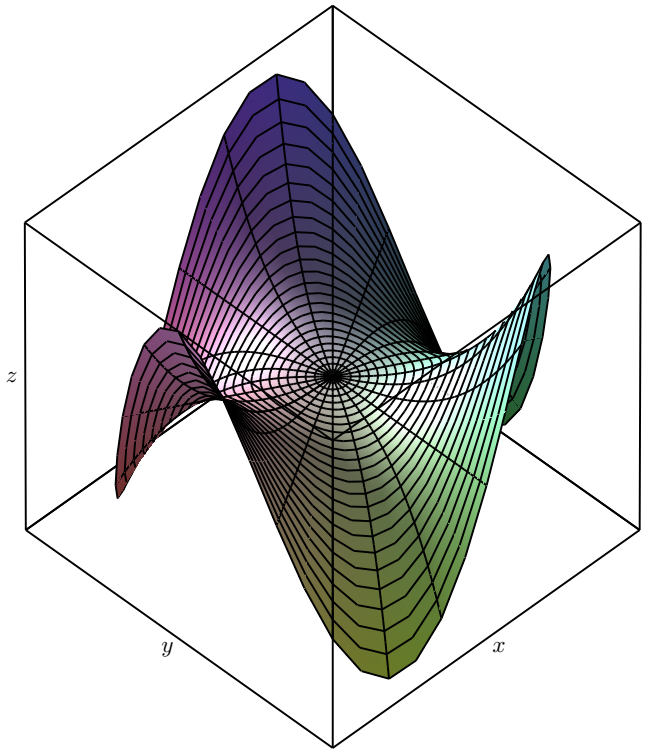

Figure 4.5: Potential field distribution surfaces for a hexapole electric field.

The construction of the hexapole that was used for this thesis is shown in Figure 4.6.

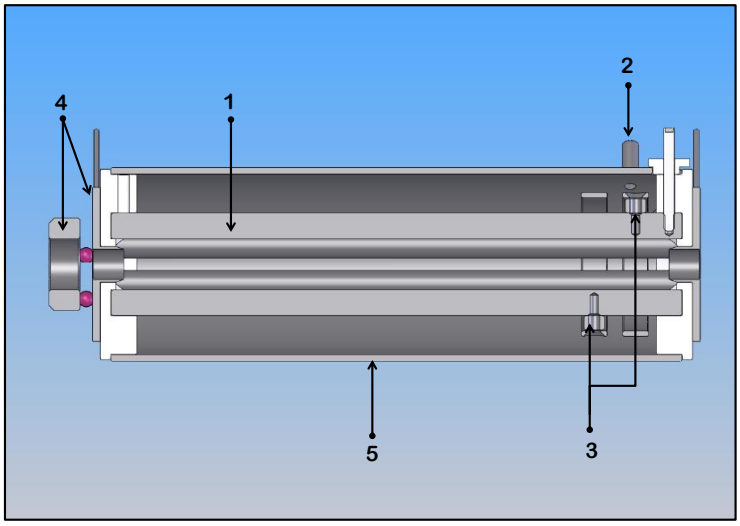

Figure 4.6: The Hexapole. 1 Rods, 2 Inlet for gas, 3 Connectors for RF, 4 Electrodes, 5 Surrounding shield

The relative location of the hexapole with respect to other elements of the machine has been shown later.

The 22-pole trap is the heart of the machine. While the body of the trap is made from copper, the rods themselves are of stainless steel. Figure 4.7 shows the trap along with ring electrodes. In the two layouts shown, the major difference is in the design of the end-cap electrodes. The tubular design in (b) presents a much smaller surface area to black-body radiation emitted from the vacuum chambers. The electrodes are encased inside a ceramic cylinder which provides electric insulation.

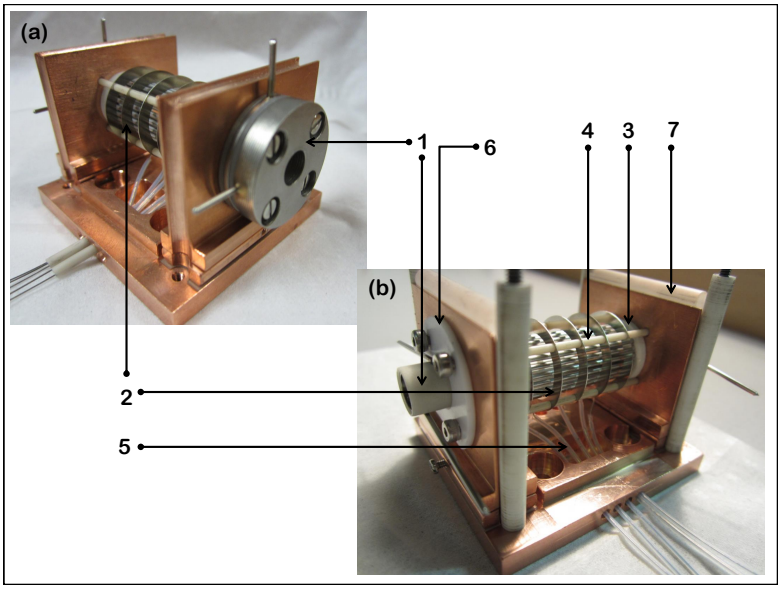

Figure 4.7: The 22-pole trap and the different designs of the end cap electrodes. 1 End cap electrodes, 2 Ring/Shaping electrodes, 3 Teflon ring to hold the rods, 4 Ceramic spacers, 5 Connectors for ring electrodes, 6 Teflon ring to hold the electrodes, 7 Sapphire rod for electrical insulation

These cylinders are held in place on either side-plate by teflon rings that are screwed into the latter. These screws also press against springs that in turn push against the ceramic spacers for the ring electrodes. This arrangement lends rigidity to them and ensures that they stay parallel to each other, which is an obvious necessity for their proper functionality. In addition, a pair of Teflon rings with 22 holes are also used on the inside of the side plates to provide precise alignment of the rods. The side plates are electrically separated from the base plate by sapphire plates, which are thermally conducting. The trap is covered by a Π shaped copper piece which remains in thermal contact with the trap. Ceramic rods between the side plates and the Π piece maintain electrical insulation. This cover shields the trap from the ∼50 K radiation that emanates from the surrounding Al shield, which is discussed later. The trap along with the cover is attached, via a copper adapter, to the second stage of a SUMITOMO RDK-2050 4K coldhead coupled to a CKW-21A compressor. This cools the walls of the trap down to 4.2 K. Earlier,

a Leybold cryostat was used which could go down to a minimum temperature of 20 K. Indium is used between surfaces that sit against one another to enhance thermal contact and compensate for surface defects that may lead to inefficient cooling. Two silicon diodes (Lakeshore Model number DT-670B-CU) are used to monitor the temperature. The first is placed on the cold head and the second one is attached to the top of the Π piece. The locations have been carefully chosen to check for temperature gradient across the trap. Typically, the second diode shows a reading that is 1 K higher than the first one. When He is introduced into the trap, this difference rises to around 2 K. The temperatures at the two points are read from a Lakeshore 332 temperature controller that also serves as the power supply for the cartridge heater.

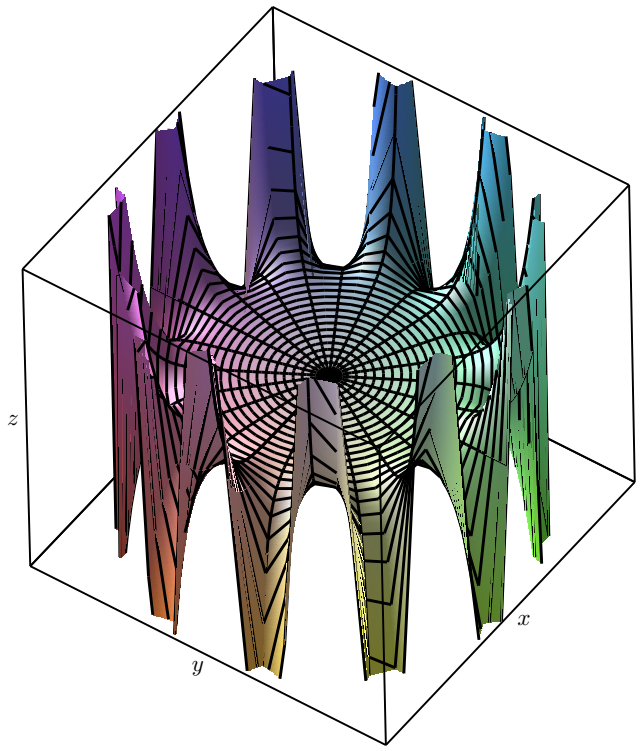

Figure 4.8: Potential surfaces for a 22-pole electric field showing alternating maxima and minima.

The Al shield is attached to the first stage of the cryostat and is therefore cooled to only about 50 K. Use of this shield is essential to protect the trap from the 300 K blackbody radiation emitted from the vacuum chamber. The surfaces of the Al plates, constituting the shield, are well polished to ensure maximum reflectivity and best possible thermal contact. The entire assembly as it sits on the cold head is shown in Figure 4.9. Recently, covered holes were introduced on the shield plates to make sure any He that may accumulate is pumped out without exposing surfaces on the inside. Details of He entry are discussed in the next section.

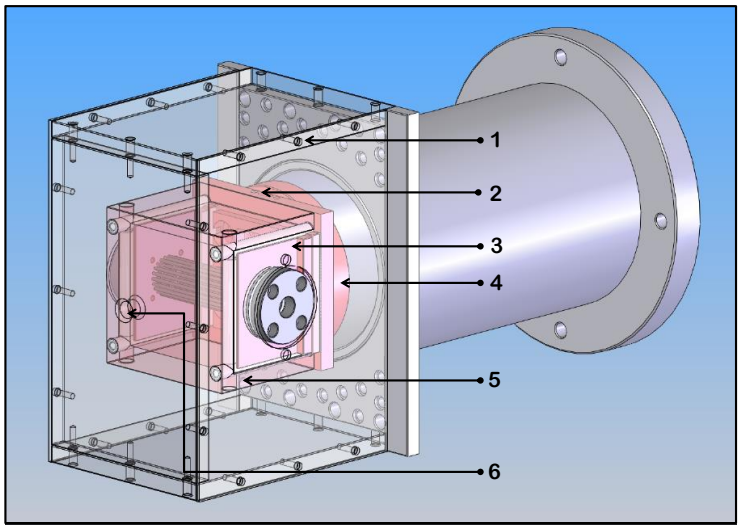

Figure 4.9: The 22-pole trap assembly. 1 Al shield attached to the first stage of the cryostat, 2 Entry point for continuous flow of He, 3 22-pole trap, 4 Adapter, 5 Π cover, 6 Entry for pulsed flow of He from the piezo valve

A cartridge heater is attached to the Π block allowing heating of the trap. This has a twofold purpose. Continuous operation of the trap at temperatures below 5 K results in condensation of residual gas in the chamber on the walls of the trap. Heating the trap at the end of a day removes all such material and cleans the surface of the trap rods. Figure 4.10 shows the construction of the trap in greater details.

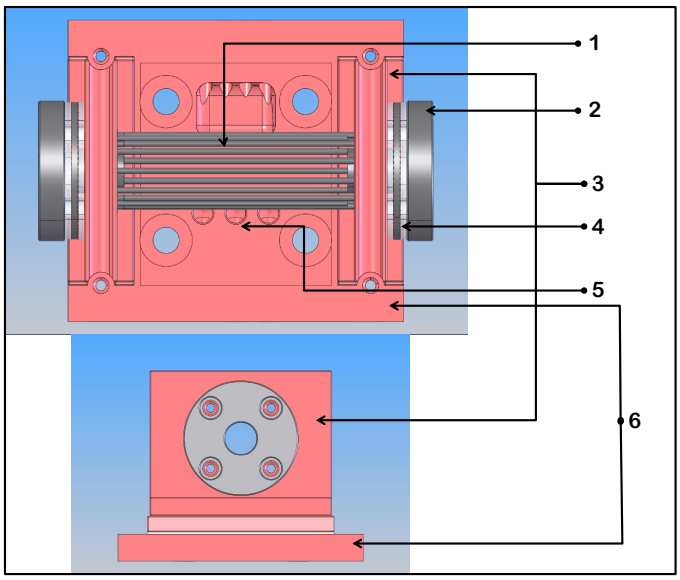

Figure 4.10: The 22-pole trap. 1 The rods, 2 End-cap electrodes, 3 Side-plate, 4 Sapphire insulation, 5 Entry point for gaseous neutrals, 6 Base plate.

Experimental trapping of ions can be realised as follows. Ions are accumulated in the trap for 10-20 ms by holding the potential on the entrance electrode of the trap at a value lower than the mean kinetic energy of the ions. During this time, the potential of the exit electrode is held high so that the ions that enter cannot escape from the other side. Use of buffer gas helps increase trapping efficiency by providing a bath for ions to dissipate the excess energy. This ensures that by the time an ion makes a complete trip after reflection from the exit electrode, its energy is lower than the entrance electrode potential. After a few more round trips the ions eventually settle to the bottom of the potential well. Figure 4.11 is a schematic illustration of the process.

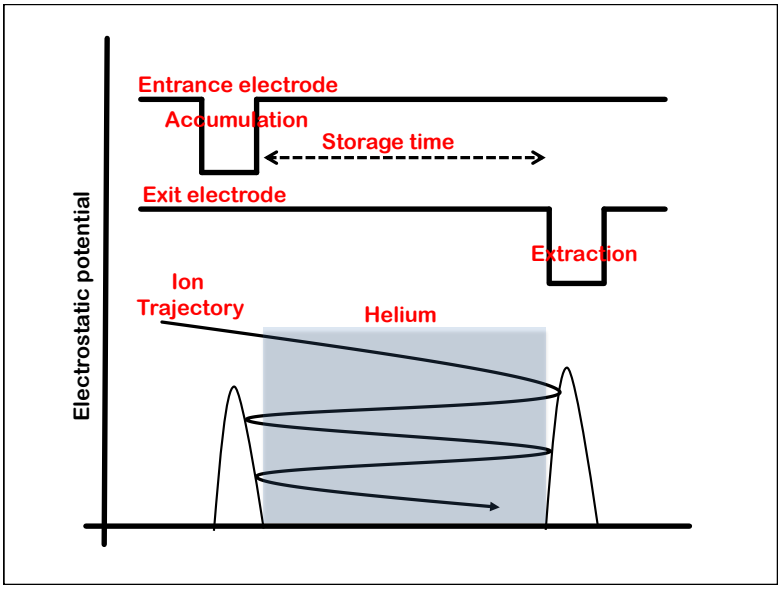

Figure 4.11: The trapping sequence. The potential on the entrance electrode is lowered to allow the ions into the trap. Ions equilibrate to the temperature of the cold head via collisions with He and settle to the bottom of the potential well created by superposition of the RF and the DC potentials. After a certain time, the potential of the exit electrode is lowered to let the ions out of the trap.

An important aspect is to make sure that the superposition of the RF amplitude on the end caps is not too large. For this it was essential to use capacitive filters between the electrodes and electrode and ground.

4.4 Cooling Ions

Collisional cooling with buffer gas relaxes translational and internal degrees of freedom of an ion or a molecule. Helium remains the best choice for this purpose. Its low mass and high vapour pressure even at temperatures lower than 3 K make it an ideal collision partner to cool hot molecules. Although it is sufficient to cool ions to ∼10 K to measure their electronic spectra at temperatures relevant to the ISM, for certain experiments even lower temperatures are desirable. Helium of

high purity (99.999 %) was used for all experiments. There are two possible ways of introducing He into the trap chamber. A precision leak valve can be used to leak in He continuously at a well defined rate which is important to maintain a stable pressure for the entire duration of the experiment. The He then enters the trap through one of the three holes on the base plate. A piezo valve, based on Gerlich's design, was used to introduce He in pulsed mode. A suitable repetition rate, usually 10 Hz, was chosen for the present experiments. The piezo material can also be resonantly excited to bleed in He for a well-defined period. For the cluster formation experiments, the piezo was gated for 500 ms at a frequency of 3.05 kHz. The design of the valve is shown in Figure 4.13.

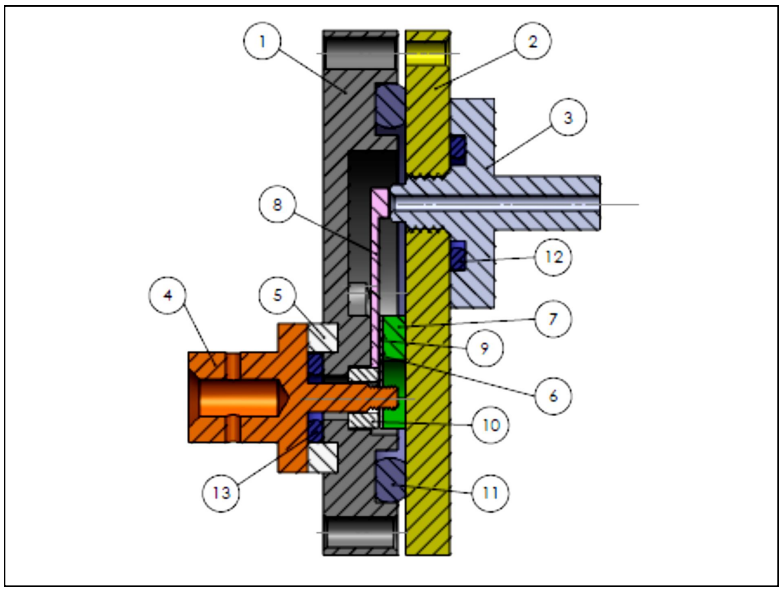

Figure 4.12: The piezo valve. The different parts are as follows: 1 Base plate, 2 Deckel, 3 Nippel, 4 Pin, 5 Macor, 6 Teflon, 7 Inox, 8 Quartz Element, 9 Copper, 10 Ceramic ring, 11, 12, 13 Viton O-Ring.

The details of the functioning of a piezo has been well documented by Gerlich. [4] Before the piezo valve was installed, a general valve from Parker was used. The pulse profile was broader and He pump out time was longer. Buffer gas cooling remains the most general method of cooling because it relaxes all the degrees of freedom through elastic and inelastic collisions. However, the efficiency of cooling

the different degrees vary and require different timescales until a real thermal ensemble is attained. Therefore, the time required for cooling ranges from a few ms to several min. When thermal equilibrium is reached, the trapped ions and the cooling neutrals reach a common temperature T, defined by the walls of the trap. The distribution of relative velocity *f(g)* is given by, [5]

$$f(g) = f_M(g;\mu,T) = (4\pi^{1/2})\left(\frac{\mu}{2kT}\right)^{3/2} g^2 exp\left(-\frac{\mu}{2kT}g^2\right) \tag{4.1}$$

where μ is the reduced mass and g is the relative velocity. However rhe translational temperature of the ions often deviate from the trap temperature. In such cases, the motion of the ions and the buffer gas can be approximated by two Maxwellians with temperatures T_1 and T_2. Then the mass weighted collision temperature is given by,

$$T = (m_1T_2 + m_2T_1)/(m_1 + m_2). \tag{4.2}$$

It is the collision temperature T that determines the internal energy of the ions after sufficient number of collisions and not the translational temperature T_1. It becomes obvious from the above expression that lower the mass of the buffer gas the more efficient a coolant it is.

Determination of ion temperature can be done accurately by spectroscopy. The rotationally resolved one colour one photon dissociation spectrum of N_2O^+ has been used as a thermometer for rotational temperature of ions. The $A^2\Sigma^+ \leftarrow X^2\Pi_{3/2}\ 1_0^2$ excitation was monitored which lies above the dissociation threshold of the ion. The number of NO^+ fragments were counted to generate the spectrum. Figure 4.14 shows the experimental spectrum and compares it to simulations done on PGOPHER. [6] While the trap temperature was 5 K, the rotational temperature of the ions was determined to be between 10 and 15 K. Ions were vibrationally cold as well, which was concluded from the other spectra and have been discussed in more details later. None of the spectra show any hot bands and no transitions were observed corresponding to population of the low frequency modes. Determination of the translational temperature required a laser of linewidth narrower

than the Doppler profile. This was made possible by the use of a mode locked Titanium: Sapphire ring laser to measure the $A^2\Pi_u \leftarrow X^2\Sigma_g^+$ rotationally resolved spectrum of N_2^+. Gaussian fit of the measured profile yielded a translational temperature of 44 K. The other, qualitative confirmation of low temperatures comes from successful formation of clusters with He atoms in the trap.

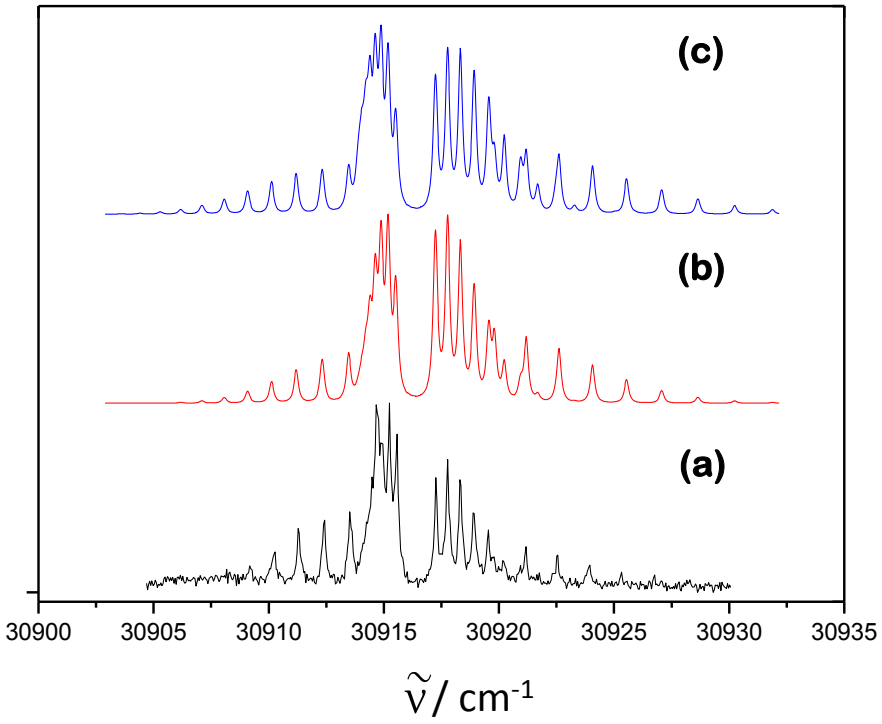

Figure 4.13: The $A^2\Sigma^+ \leftarrow X^2\Pi_{3/2}\ 1_0^2$ spectrum of N_2O^+. Trace (a) is the experimental photodissociation spectrum. Traces (b) and (c) are simulations at 10 and 15 K, respectively.

4.4.1 Determination of neutral number density

A capacitance manometer (CMR-365) was installed to measure the absolute pressures in the trap. This was done to determine neutral number densities necessary to evaluate cluster formation kinetics in the LIICG method. The pressure values

as indicated by the external ion gauge (P_{IG}), corrected for He and the absolute pressure values given by the capacitance manometer (P_{CM}), with the trap at 5 K were plotted. The slope was used to determine the calibration factor which was found to be 35.27 ± 2.07.

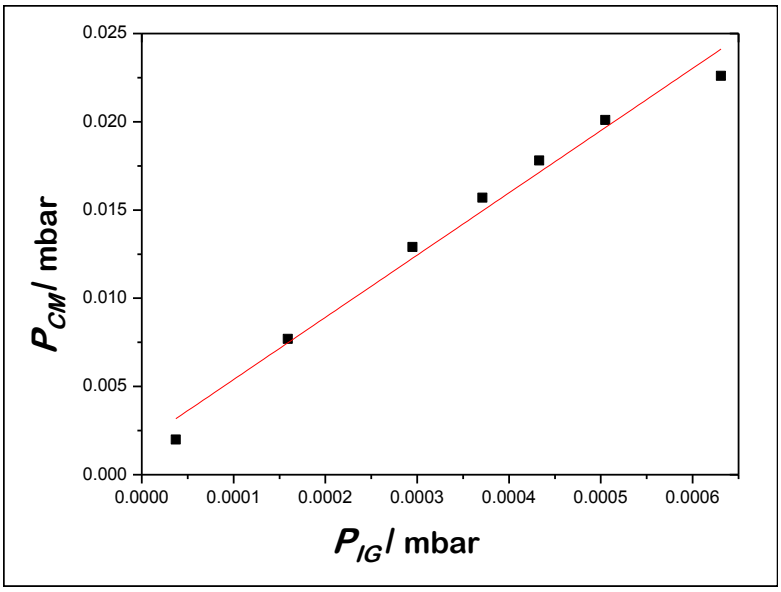

Figure 4.14: Plot of P_{IG} against P_{CM}. The calibration factor was determined from the slope of the plot.

The phenomenon of thermal transpiration causes a pressure difference between the trap and that shown on the manometer due to different operating temperatures. The magnitude of pressure drop depends on pressure, geometry and type of gas. The viscous flow regime corresponds to high pressures and the two pressures are then in equilibrium. Therefore,

$$p_2/p_1 = 1 \tag{4.3}$$

where p_2 and p_1 are the pressures at the manometer and in the trap respectively. For small values of pressure or in the regime of free molecular flow, there is an

equilibration of the fluxes. This leads to a difference in pressures. Knudsen's value gives the ratio of the pressures:

$$p_2/p_1 = \sqrt{(T_2/T_1)} \tag{4.4}$$

where, T_1 and T_2 are temperatures of the trap and manometer respectively. This condition applies when the velocity of He in the two parts correspond to their respective temperatures and the hole of the interconnecting tube is small compared to the chamber dimensions. If the connection between the two sides is through an aperture, then the probabilities for He atoms to traverse the space are equal for both entry sides. For a tubular connection, as is used in reality, transmission probability is larger for hot atoms towards the cold side than the other way around. In the pressure regime in between the two discussed above (regime of Knudsen flow), the ratio of pressures is given by, [7]

$$\frac{p_1}{p_2} = 1 + \frac{\sqrt{T_1/T_2} - 1}{A \cdot (X/X_0)^2 + B \cdot X/X_0 + C\sqrt{X/X_0} + 1} \tag{4.5}$$

$$X = \frac{2dP_2}{T_1 + T_2} \tag{4.6}$$

where X_0=1 mm Pa/K, d is the diameter of the tube connecting the trap and the manometer. A, B and C are nondimensional constants that were determined for He, in the gas temperature range 4.2−90 K to be,

$$A = 6.11 \tag{4.7}$$

$$B = 4.26 \tag{4.8}$$

$$C = 0.52 \tag{4.9}$$

Another factor F has been defined as the degree of thermal transpiration and is given as,

$$F = \frac{1 - P_1/P_2}{1 - \sqrt{T_1/T_2}}. \tag{4.10}$$

F is 0 at high pressures and 1 in the Knudsen region. For the present experiments, F is 0.8345 when X is 2.59×10^{-2} mm Pa/K for a manometer reading of 1.29×10^{-2} mbar. A general formulation for neutral number density can then be derived and is given as:

$$n = n_0 \frac{p_1}{p_0} \frac{T_0}{T_1} \tag{4.11}$$

where n_0, p_0 and T_0 are Avogadro's number, standard pressure and temperature respectively. Using the above expression, the number density of He was calculated to be $4.75 \times 10^{15}\,\mathrm{cm}^{-3}$ for the above mentioned manometer reading.

4.5 Daly detector

A Daly type detector [8] is used to count the ions exiting the second quadrupole. It consists of a highly polished metal conversion dynode that is held at -25 kV. The positive ions are accelerated towards the dynode under the influence of the highly negative field gradient. Upon striking the surface, secondary electrons are emitted. The latter, under the influence of the same high voltage, are accelerated towards a grounded scintillator (BC400 plastic scintillator, 0.5 mm thick, from GC Technology GmbH, Freidling 12 D-84172 Buch am Erlbach). The electrons pass through a thin coating of aluminium before hitting the phosphor, where they are converted to photons. This coating prevents entry of scattered light, thereby reducing greatly background noise. It also serves to reflect back the photons that may move in the wrong direction from the phosphor. The output pulse of the scintillator is of the order of a few nanoseconds. The photons so created are finally detected by a photomultiplier tube (R647 Hamamatsu PMT) that is located outside the vacuum chamber. The detector has a high efficiency and is extremely robust. It does not undergo degradation with venting and has no mass discrimination. In case of problem with the PMT tube, replacement can be done without breaking vacuum. The dynode and photomultiplier arrangement are housed inside a grounded shield to prevent penetration of the high electric field from penetrating into the second quadrupole. The setup allows easy laser access

to the 22-pole trap because of its transverse location with respect to rest of the machine.

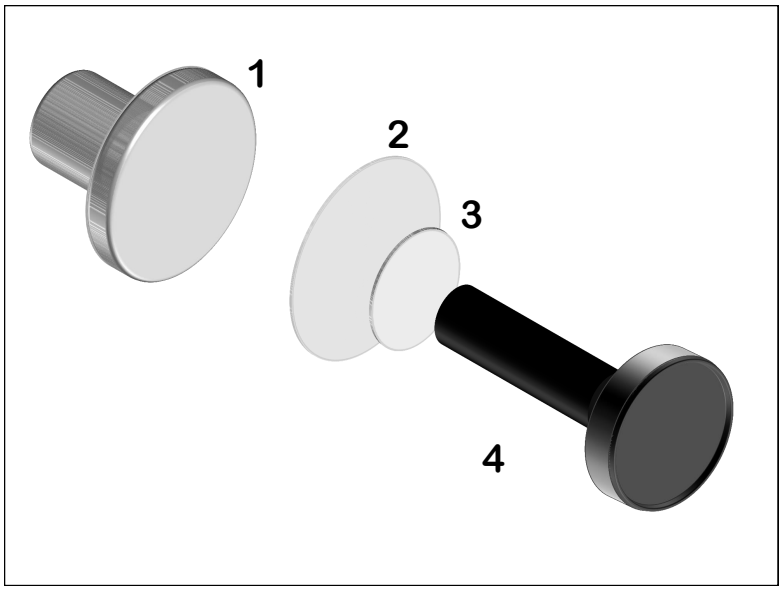

Figure 4.15: Daly detector, 1 Conversion dynode, 2 Holder, 3 Phosphor plate, 4 Photomultiplier tube

4.6 Data acquisition

The analogue output from the PMT is sent to a discriminator (Phillips Scientific Model 6904, 300 MHz). This output is sent to a counter (HP5316A). Later another one was used. The counter receives a gate either from a delay generator. This can be achieved in two ways. A commercial delay generator from Berkeley Nucleonics Corporation (BNC) or a PCI-6023E data acquisition card (DAQ) from National Instruments have been used for this purpose. In all the experiments, the BNC pulse generator was used as the master clock, providing the trigger pulse for the experiment via a TTL pulse to the DAQ card. This initiated a sequence of pulses, which were applied to the entrance and exit electrodes of the trap with a well defined width and delay. Another card, PCI-DAS6014 from Measurement Computing was used to tune the masses on the two quadrupoles. Programs written in LabView were used to communicate with the electronics through the cards. The

BNC pulse generator was used to control the time and extent of opening of the piezo valve. When the piezo was resonantly excited, the same provided the gate for the frequency generator. Besides these components of the machine, trigger signals and delay between flashlamp and Q-switch for pulsed lasers were derived from the BNC delay generator as well. When continuous wave radiation was used, a shutter had to be used, the opening time for which was defined by the BNC delay generator.

4.7 Laser

Several different laser systems were used as sources of radiation. The photodissociation and charge transfer experiments were all conducted with pulsed nanosecond lasers. For broad range scans, an EKSPLA Optical Parametric Oscillator was used. It is straightforward to scan with such a laser over a wide range. Typical pulses are 5 ns wide and the smallest possible step size is 0.1 nm. The linewidth is 5 cm^{-1} and the output power varies between 10-20 mJ per pulse. It is obvious from the specifications that such a laser is suited only for survey scans. The UV output was used to provide the second photon- the fixed wavelength in a two colour scheme- to promote fragmentation in resonance. For rotational resolution, pulsed dye lasers pumped by an Nd: YAG laser were used. SCANMATE from LAMDA-PHYSIK was used for the earlier experiments and the linewidth was 0.15 cm^{-1}. An internal *é*talon could be employed to achieve an even finer resolution of 0.05 cm^{-1}. Later a double grating pulsed dye laser from SIRAH was installed which had an output linewidth of 0.07-0.09 cm^{-1}. For the LIICG experiments, CW sources were preferred for reasons explained later. Either a mode locked Titanium: Sapphire ring laser (pumped by a 532 nm diode pumped solid state cw laser) or a diode laser was used. The diode was purchased from SACHER. The ring laser had a linewidth of 500 kHz. The internal wavemeter and *é*talon arrangement ensured such a narrow linewidth. A free running diode was as wide as ∼800 MHz, while with an external grating arrangement, linewidths as

low as ∼10 MHz were achieved. Calibration of laser frequency was done by using a commercial wavemeter from Hi-Finesse.

4.8 Arrangement of the machine

The previous sections described the different elements that are necessary components for the experimental set-up. Depending upon the scheme of spectroscopy that one wishes to employ, these parts can be assembled in several different ways to achieve an optimum configuration best suited to the needs of a specific experiment. Accordingly, the machine has been remodified on more than one occasion and this section describes the different orientations that were used and their advantages and limitations.

4.8.1 Configuration 1

In this arrangement, the ion source was oriented perpendicular to the rest of the machine. A magnetic bender placed right after the extraction electrode, served to compress and bend the ion beam into a hexapole. Neutrals, remained unaffected and were pumped out by a turbo-molecular pump that was attached to the flange opposite the source. It was possible to look down the axis of the machine through UHV compatible windows provided on either end. These were also used to introduce the laser, and its re-emergence from the other end confirmed proper alignment.

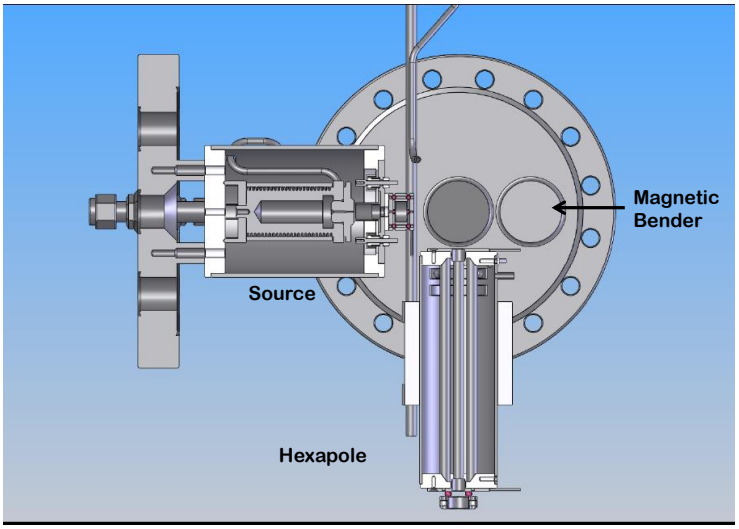

Figure 4.16: The ions after extraction from the source were bent into the hexapole by the magnetic bender. The hexapole then guided the ions into the first mass filter

The hexapole was installed to act as a pre-trap or a collision cell to relax ions to room temperature. It had a point of entry for buffer gas. Another idea was to prepare secondary ions in the hexapole, by laser induced reactions, beginning from primary ones created in the source. However, for most experiments, it was used as an ion guide.

4.8.2 Configuration 2

The layout of the trap was significantly modified in this setup. Immediately after the exit electrodes of the first quadrupole, an electrostatic bender was introduced. By proper choice of voltages on the four poles, the ion beam could be bent in any direction as desired. The 22-pole trap was relocated to sit behind the bender. When the photo-products were released from the trap, the polarity of the voltages on the quadrupole rods were reversed to direct the ion beam into the second quadrupole. The cryostat was placed on top of the chamber, allowing laser access through the windows coaxial with the trap.

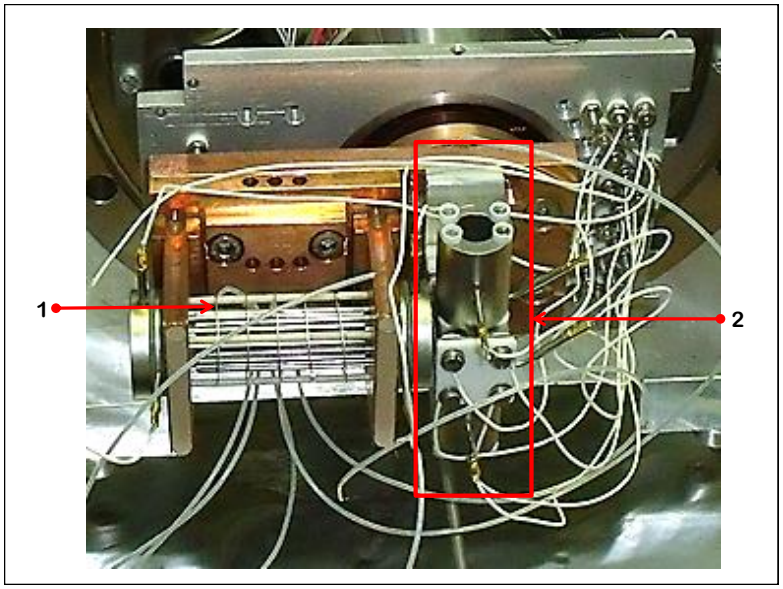

Figure 4.17: The trap (1) was relocated to sit perpendicular to the axis of the quadrupoles. An electrostatic bender (2) was used to transport the ions in and out of the trap.

Due to the significantly shorter path that the laser had to traverse, it proved to be much simpler to align. However, it was later realised that the short turning radius provided by the bender led to a significant loss in ion intensity.

4.8.3 Configuration 3

Before starting with the LIICG experiments, it was decided to simplify the arrangement of the machine significantly. The magnetic bender, hexapole and the electrostatic bender were removed. The ion source, quadrupoles and the trap were placed on the same axis. The cryostat was put back in its initial horizontal position. These modifications resulted in the simplest possible layout which would allow a stepwise determination of necessary future additions specific to enhancement of cluster formation.

Bibliography

[1] E.Teloy and D. Gerlich. Integral Cross Sections for Ion Molecule Reactions: The Guided Beam Technique. *Chem. Phys.*, 4:417, 1974.

[2] C. Hock, J. B. Kim, M. L. Weichman, T. I. Yacovitch, and D. M. Neumark. Slow photoelectron velocity-map imaging spectroscopy of cold negative ions. *J. Chem. Phys.*, 137:244201, 2012.

[3] K.R. Asmis, G. Santambrogio, M. Brümmer, and J. Sauer. Polyhedral Vanadium Oxide Cages: Infrared Spectra of Cluster Anions and Size-Induced d-Electron Localization. *Angew. Chem. Int. Ed.*, 44:3122, 2005.

[4] D. Gerlich. http://www.tu-chemnitz.de/physik/ION/Technology/PiezoValve/index.html.

[5] Dieter Gerlich. Inhomogeneous Electrical Radio Frequency Fields: A Versatile Tool for the Study of Processes with Slow Ions,. *Adv. Chem. Phys.*, 82:1, 1992.

[6] C. M. Western. PGOPHER, a Program for Simulating Rotational Structure, http://pgopher.chm.bris.ac.uk .

[7] H.Tanuma, H. Fujimatsu, and N. Kobayashi. Ion mobility measurements and thermal transpiration effects in helium gas at 4.3 K. *J. Chem. Phys.*, 113:1738, 2000.

[8] N. R. Daly. Scintillation Type Mass Spectrometer Ion Detector. *Rev. Sci. Instrum.*, 31:264, 1960.

5 Photodissociation Spectroscopy

This section discusses the electronic spectra that were measured by photodissociation. A general scheme is where an ion is resonantly excited by the first photon ans sequentially fragments with a second one. Depending upon the energy levels and dissociation threshold of an ion, the two photons can be of the same wavelength or different. For diacetylene (HC_4H^+) and triacetylene (HC_6H^+) cations, the transitions studied were in the visible while fragmentation was achieved by a UV photon. The third ion ($C_4H_3Cl^+$), absorbed two photons of the same colour making it a one laser experiment. For the fourth, protonated benzene ($C_6H_7^+$), absorption of one photon in the UV was sufficient to electronically excite the ion and induce dissociation.

The first three ions discussed in this section were all derived by electron bombardment of a sample of neutral C_4H_2. Diacetylene is synthesised and stored as a solid in a freezer at -80°C. The boiling point of diacetylene is 10°C and so at room temperature a gas mixture with helium was prepared and stored in a lecture bottle. This bottle was attached to an inlet through which the molecules were then introduced into the source chamber at a steady rate to maintain a pressure of $5\times\ 10^{-6}$ mbar. Extreme conditions within the source initiate ion neutral reactions, leading to the formation of several charged species. While HC_4H^+ was produced by direct ionisation, HC_6H^+ resulted from polymerisation. As will be discussed later, $C_4H_3Cl^+$ was discovered accidentally because its neutral counterpart was present as an impurity in the sample precursor. $C_6H_7^+$ was generated by dehydrogenation reaction of 1,6-dihydrocyclohexene. The latter has an appreciable vapour pressure at room temperature enabling its introduction into vacuum directly through a leak valve. After mass filtering, the ions were injected into the

22-pole trap where they underwent collisions with helium buffer gas resulting in cooling of internal degrees of freedom. Typically a few thousand ions were trapped for these experiments which is an illustration of the sensitivity of this technique. The repetition rate being 10 Hz, the ions had 60-70 ms for thermal equilibration after which they were exposed to laser radiation. Photofragments were let out of the trap immediately after, which were then analysed by a second quadrupole and counted by a Daly detector.

5.1 The $A^2\Pi_u \leftarrow X^2\Pi_g$ electronic spectrum of HC_4H^+

5.1.1 Introduction

In 2010, Krewłoski et al [1] reported the observation of a new diffuse interstellar band at 5069 Å. They compared their data with previously published gas phase laboratory spectrum of the origin band of the $A^2\Pi_u \leftarrow X^2\Pi_g$ electronic transition of HC_4H^+ and concluded a match [2]. This work was done to examine the basis of this claim more closely. Additional absorption features were measured in the gas phase and compared with the DIB catalogue. Since there is a high concentration of DIBs in the optical region 5000-7000 Å, it is necessary to identify more than one absorption feature of a specific carrier to make an absolute assignment.

The molecular orbital configurations for the ion in the $X^2\Pi_g$ and $A^2\Pi_u$ states are $...(\pi_u)^4(\pi_g)^3$ and $(\pi_u)^3(\pi_g)^4$ respectively. The spin orbit constant in the ground state is -33.3 cm^{-1} and -31. cm^{-1} in the excited state. The negative sign indicates that the Ω= 3/2 component is lower in energy than the 1/2 component. The rotational constant of HC_4H^+ (B''=0.14690 cm^{-1}) is quite small compared to spin-orbit splitting and therefore for lower J levels, the $A^2\Pi_u \leftarrow X^2\Pi_g$ transition belongs to Hund' s case (a). An energy level diagram is shown in Figure 5.1.

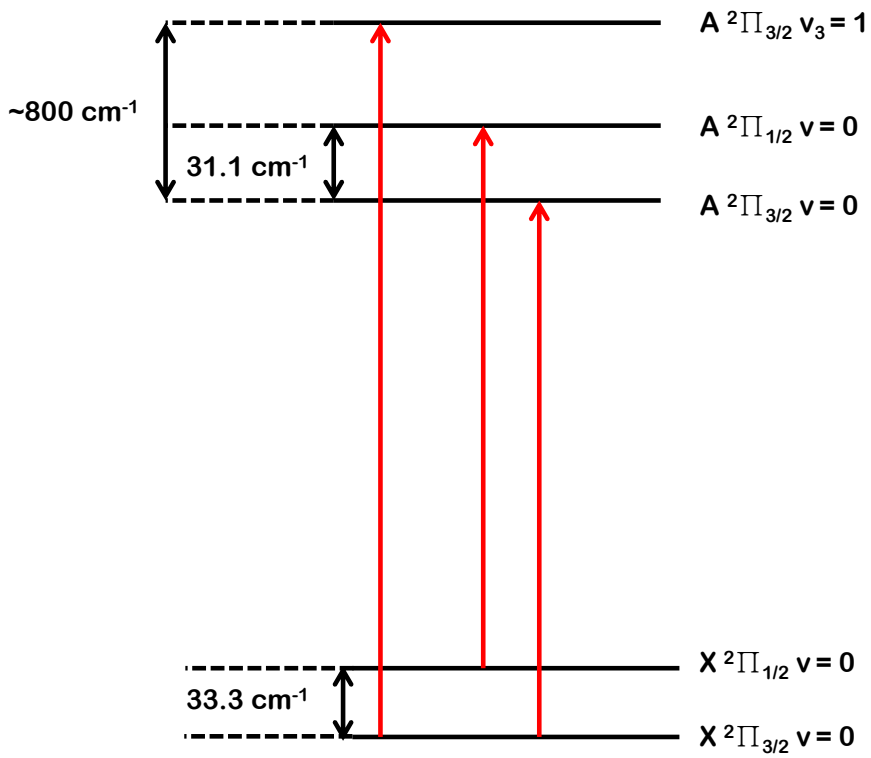

Figure 5.1: Energy level diagram of the $X^2\Pi_g$ ground and $A^2\Pi_u$ excited electronic states involved in the spectrum shown in Figure 5.2.

5.1.2 Results and Discussion

Figure 5.2 is the $A^2\Pi_u \leftarrow X^2\Pi_g$ electronic spectrum of HC_4H^+. Within the energy range relevant to the present experiments, HC_4H^+ is known to have a single dissociation pathway, i.e, loss of an H atom. All the spectra shown in this section were recorded by counting C_4H^+ fragments. The broad range spectrum was measured with radiation from an OPO with a linewidth of $5\,cm^{-1}$ (1 Å). The fragmentation photon was taken from another OPO. The origin band at 5067.8 Å is the strongest absorption feature. Each individual band was then rotationally resolved and except the origin band, the rest have been shown in the insets in Figure 5.2. The

origin band has been shown in Figure 5.3. For rotationally resolving individual bands, a dye laser of linewidth $0.15\,\mathrm{cm}^{-1}$ (0.04 Å) was employed.

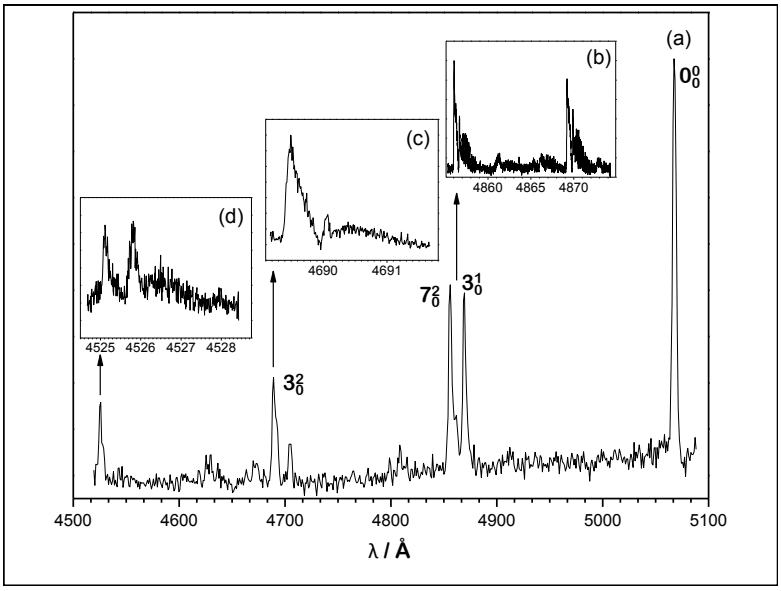

Figure 5.2: $A^2\Pi_u \leftarrow X^2\Pi_g$ electronic absorption spectrum of HC_4H^+ measured by resonance two colour two photon dissociation at $\sim 25\,\mathrm{K}$ with a laser of bandwidth 1 Å. The spectra in the insets were measured with 0.04 Å resolution. Assignments of the bands are given in Table 5.1.

Table 5.1: Band Maxima (R_1 bandheads, ± 0.1 Å) observed in the $A^2\Pi_{3/2,u} \leftarrow X^2\Pi_{3/2,g}$ transition of HC_4H^+ measured at $\sim 25\,\mathrm{K}$ and their relative intensities.

Assignment	λ/ Å	Relative Intensity
0_0^0	5067.8	1
3_0^1	4869.2	0.5
7_0^2	4856.0	0.5
3_0^2	4689.5	0.3
	4525.8	0.1
	4525.1	0.1

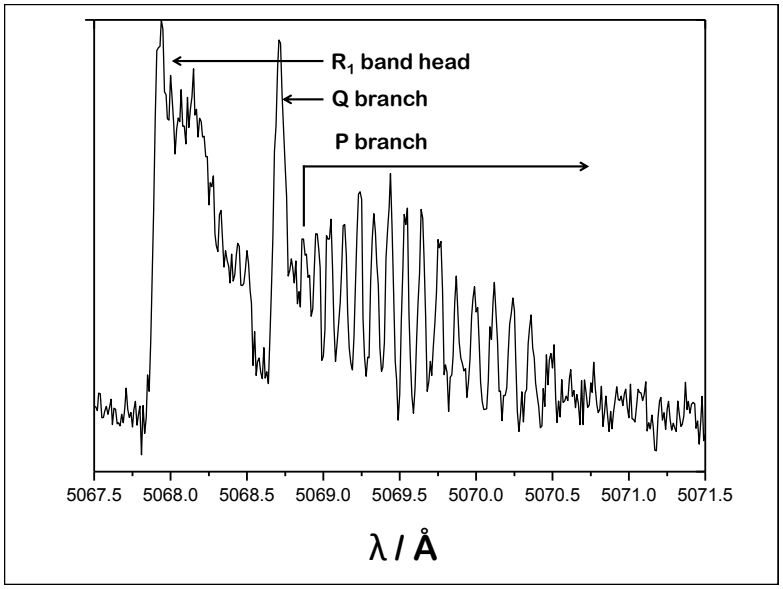

Figure 5.3: The rotationally resolved origin band of the $A^2\Pi_u \leftarrow X^2\Pi_g$ electronic transition of HC_4H^+. At 25 K, the spectrum is dominated by transitions from the Ω= 3/2 component.

The rotational temperature of the ion ensemble is determined from fitting a simulation to the experimental spectrum shown in Figure 5.3. The profiles were simulated on PGOPHER using known rotational constants. This gave a value of $\sim$25 K. In Figure 5.2 the baseline goes to zero on either side of the origin band. "Hot" bands, which would arise due to residual population of low frequency modes (ν_9 is 200 cm^{-1}) were not observed. This is evidence for equilibration of vibrational and spin-orbit temperature and it can be concluded that the transitions in the spectrum originate from Ω= 3/2 component in the $X^2\Pi_g$ ground state. Although there was no new information regarding the 0_0^0, 3_0^1 and 7_0^2 bands, the other three bands having intensities about three to six times weaker than the origin band are reported for the first time. Due to overlapping absorptions from C_2 and C_3, it is difficult to identify them by fluorescence or cavity ring down (CRD) spectroscopy. This is an advantage of using mass selection prior to laser probing because it ensures that an ion of only a single m/z ratio is studied. Another important feature of the photodissociation technique is that it is background free. The C_4H^+ fragments were almost exclusively produced when the summation of energy

of the two photons exceeded the thermodynamic threshold. Ion generation was soft enough to result in a collision induced background of less than 10 counts per ion filling cycle.

A comparison of fragmentation and CRD spectra revealed that the intensity patterns in the former were realistic within error limits of 10 %.

Figures 5.4 and 5.5 show a comparison of laboratory spectra measured in the 22-pole trap and by CRD with the astronomical one from Ref. [1]. Temperatures were in the range of 50−80 K, based on earlier observations made in diffuse interstellar clouds for non-polar polyatomics. [3, 4]

A linewidth of 0.33 Å and two different temperatures of 30 and 60 K were used. The rotational constants for the simulations are summarised in Table 5.2. It

Table 5.2: Constants used for PGOPHER simulations taken from [5]

Molecular constants/cm^{-1}	
T_{00}	19 722.594
B''	0.14690
B'	0.14009
D''_0	2.0×10^{-8}
D'_0	1.9×10^{-8}
A''	-33.3
A'	-31.1

was necessary to account for line broadening in the interstellar spectrum due to velocity dispersion. Therefore, interstellar velocity dispersions of 6 and 20 km s^{-1} were chosen.

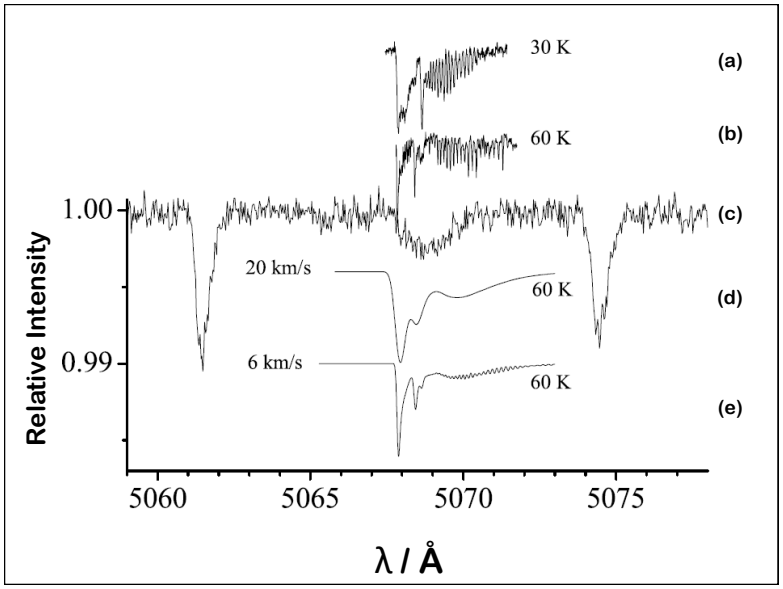

Figure 5.4: Trace (c) is the astronomical spectrum taken from Ref. [1]. Spectra (a) and (b) are rotationally resolved origin band of the $A^2\Pi_u \leftarrow X^2\Pi_g$ electronic transition of HC_4H^+ measured in the ion trap and by CRD, respectively. (d) and (e) are simulations of rotational profiles considering interstellar broadening of 20 and 6 km s^{-1}.

Simulations shown in Figure 5.5 accounted for non-Boltzmann rotational population. This becomes a possibility in space due to competing collisional rates and magnetic dipole transitions. (See Appendix A for more details)

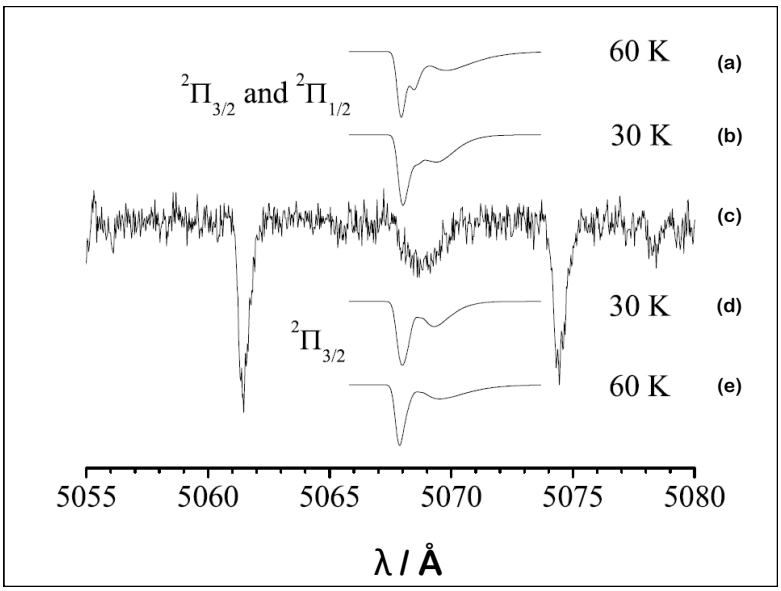

Figure 5.5: Trace (c) is from Ref. [1]. The simulated profiles (a) and (b) are at 60 and 30 K with spin-orbit and rotational temperatures equilibrated. Traces (d) and (e) have the $X^2\Pi_{1/2}$ component depopulated by magnetic dipole transitions.

Inspite of the broadening effects and different temperatures employed for the above simulations, no matches were observed with the astronomical spectrum. [6] Since neither the central wavelength nor the band profile showed agreement, it was concluded that HC_4H^+ is not a possible carrier for the reported DIB in Ref. [1].

5.2 The $A^2\Pi_g \leftarrow X^2\Pi_u$ electronic spectrum of HC_6H^+

5.2.1 Introduction

The motivation behind measuring the electronic spectrum of HC_6H^+ was to compare with astronomical observations. The origin band had been recorded previously, [7] therefore, focus of this study was to examine the vibrational transitions. Structurally, this cation is very similar to HC_4H^+ ion. The molecular orbital configurations for the ion in the $X^2\Pi_u$ and $A^2\Pi_g$ states are $...(\pi_u)^4(\pi_g)^4(\pi_u)^3$ and $(\pi_u)^4(\pi_g)^3(\pi_u)^4$, respectively. The ground state is inverted, with the Ω= 3/2 spin-orbit component lying 31.4 cm^{-1} below the Ω= 1/2. The spin orbit splitting constant in the excited $A^2\Pi_g$ state is -28.41 cm^{-1}. As for HC_4H^+, the $A^2\Pi_g \leftarrow X^2\Pi_u$ transition of HC_6H^+ belongs to Hund' s case (a).

5.2.2 Results and Discussion

Figure 5.4 shows the $A^2\Pi_g \leftarrow X^2\Pi_u$ electronic spectrum of HC_6H^+ measured by a resonant two-colour, two-photon dissociation. Within the energy range relevant for the present measurements, two fragmentation pathways are available to the HC_6H^+ ion. These are loss of an H atom and that of a C_3H_2 unit.

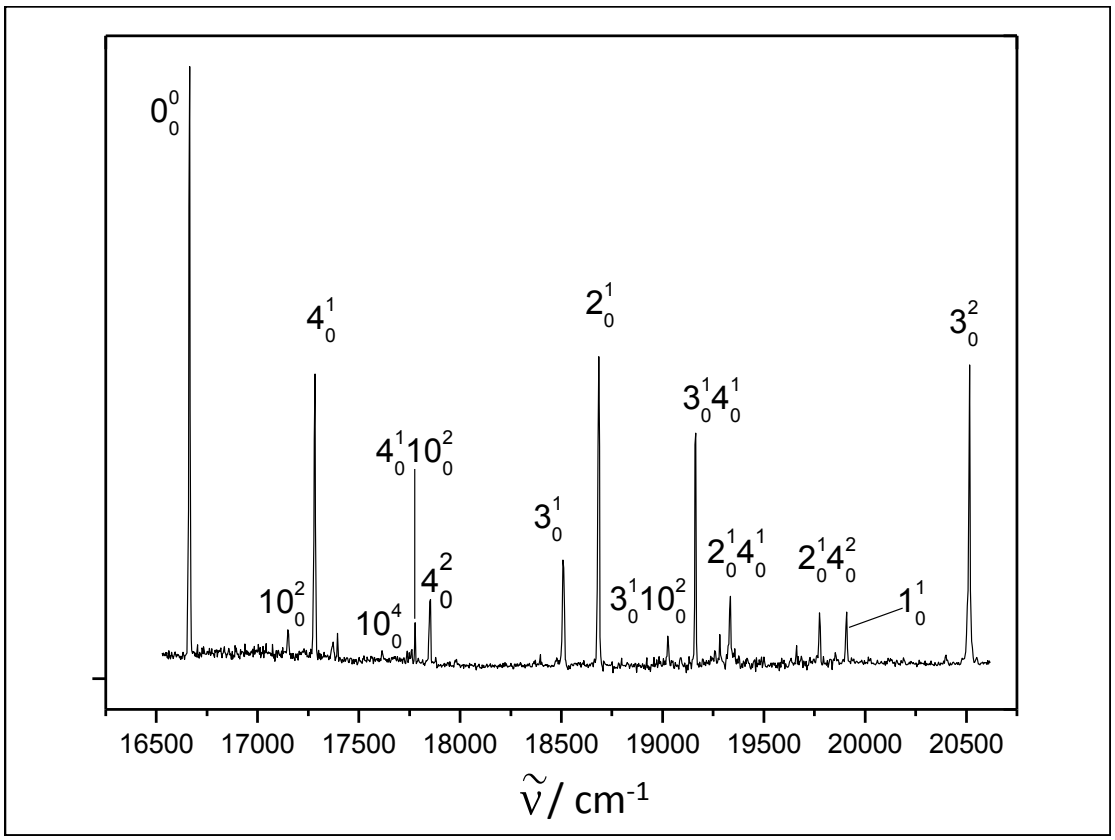

Figure 5.6: The $A^2\Pi_g \leftarrow X^2\Pi_u$ electronic spectrum of HC_6H^+. Loss of H and C_3H_2 units were monitored to generate the spectrum.

The former occurs by unimolecular bond cleavage, whereas the latter proceeds via a rearrangement/isomerisation of the parent ion near the threshold. The spectrum is dominated by the origin band and shows progressions in the ν_3 and ν_4 symmetric stretching modes in the $A^2\Pi_g$ state. The transitions originate from the $v=0$ level of the $X^2\Pi_u$ ground electronic state. Hot bands that could arise due to residual population of the low frequency modes ($\nu_{13}=100\,\mathrm{cm}^{-1}$) were not detected, indicating that the ions were cooled vibrationally with a population of $\sim 0.3\,\%$ of $v=0$ at 25 K.

Comparison of the spectrum in Figure 5.6 with a previously recorded laser excitation spectrum [8], showed anomalies in the intensity patterns in the former. The latter was used a reference because the quantum yield of HC_6H^+ remains constant

in the range 4 000−8 000 ÅThe 2^1_0 and 3^2_0 bands are more intense than expected from the excitation spectrum. This is attributed to the rate of fragmentation being a function of the internal energy of the ion.

The origin band of the $A^2\Pi_g \leftarrow X^2\Pi_u$ transition was measured and compared to simulations done using the known rotational spectroscopic constants. The best fit was obtained for a rotational temperature of 25 K. Table 5.2 lists the constants and their values. At 25 K, the v= 0 level of the $X^2\Pi_{u,1/2}$ has only about $\sim$15 % of the population of v =0 of $X^2\Pi_{u,3/2}$. Figure 5.7 shows the measured and simulated origin band profile. The shoulder in the unresolved P branch is the much weaker transition arising out of the Ω= 1/2 spin-orbit component. [9]

Table 5.3: Constants used for PGOPHER simulations taken from [10]

Molecular constants/cm^{-1}	
T_{00}	16 654.6873
B''	0.044 594
B'	0.043 792
B''/B'	1.018
A''	-31.40
A'	-28.41

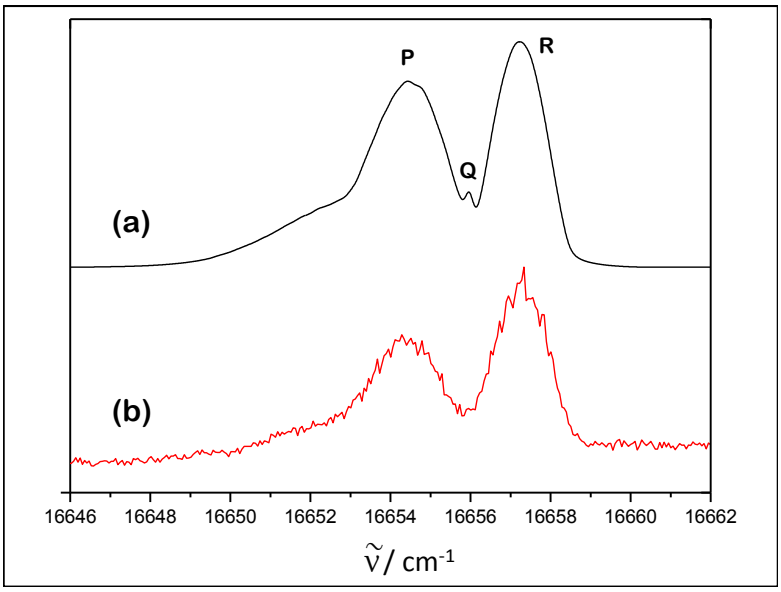

Figure 5.7: The origin band of the $A^2\Pi_g \leftarrow X^2\Pi_u$ electronic transition of HC_6H^+. (a) is the simulated spectrum and (b) is the experimental one.

5.3 The $^2A' \leftarrow {}^2A''$ electronic transition of $C_4H_3Cl^+$

5.3.1 Introduction

The original aim was to measure the electronic transitions of molecules with the general formula $HC_{2n+1}H^+$ in the gas phase. The absorptions of the so called odd cationic polyacetylene chains were studied earlier by Matrix Isolation Spectroscopy. Neutral diacetylene vapours were used to generate these ions. For n=3, one expects to see HC_7H^+ ions with an m/z of 86. However, no signal was observed upon scanning the laser in the expected region. A closer look at the mass spectrum revealed one more peak at m/z = 88 with an intensity roughly a third of the one at 86. This was the first indication that chlorine was a constituent atom in the generated ion. An analysis of the sample of diacetylene, used for ion production in the above experiments, revealed the presence of neutral C_4H_3Cl. The latter remains in the sample if the distillation process is inadequate. Neutral C_4H_3Cl can contaminate the sample of C_4H_2 if not extracted at -20 °C.

Literature survey showed several experiments that had been done to characterise the isomers of neutral C_4H_3Cl. Mass spectrometry, NMR, microwave, IR and Raman spectroscopy are among the techniques that have been employed. [11–14] However no data was found about the structural properties of the cation. The molecule that has been studied by high resolution spectroscopy and bears the closest resemblance to $C_4H_3Cl^+$ is $C_4H_4^+$. The latter was used as a test molecule for theoretical calculations as mentioned below. As is evident, substitution of an H-atom by Cl gives rise to several isomers. The C-Cl bond so formed is also labile, making it possible to measure the spectrum by photodissociation in the gas phase by the following scheme: $C_4H_3Cl^+ + h\nu \rightarrow [C_4H_3Cl^+]^* + h\nu \rightarrow C_4H_3^+ + Cl$. In order to elucidate the role of different isomers in the observed spectrum, Matrix Isolation experiments and calculations were also necessary.

5.3.2 Results and Discussion

The electronic transitions of $C_4H_3Cl^+$ were identified by conducting a survey scan by Matrix Isolation Spectroscopy. The spectrum obtained was rich and indicated the possible contribution of several isomers. A low resolution broad range spectrum was recorded in the gas phase in an ion-trap at 20 K with a laser of bandwidth $5\,cm^{-1}$. The absorptions in the matrix are shifted and broadened because of the perturbation due to neon environment. This is very well illustrated in Figure 5.8 which compares the two relevant spectra. The matrix trace has been shifted by $\sim$2.4 nm match with the gas phase spectrum. Broadening effects aside, there are two major differences. Firstly, the intensity patterns are different and this can be attributed to the two separate techniques used for measuring. Secondly, in the gas phase no transitions were observed to the red of the band at 520 nm. The ion trap spectrum helps interpret the nature of the broad bands observed in the matrix. For example, the asymmetry of the profile at 480 nm in the matrix is because of the overlap of five vibrational bands which are clearly visible in the blue trace.

Table 5.4 is a compilation of the band maxima positions and of the transitions observed in the matrix and gas phase. Overall the contribution of three isomers have been observed, however only two show up in the ion trap measurements. Possible reasons are discussed later. Assignments of the vibrational bands in table 5.4 were done on the basis of calculated values for ground state frequencies. Theory suggested the possibility of seven isomers, with $ClBa^+$ (Figure 5.9) being the most stable on the potential energy surface. Only five of the seven isomers are relevant in the energy range of the present experiments. Both the neutral and cationic forms of these are shown in Figure 5.9. The other two lie almost $200\,kJ\,mol^{-1}$ to higher energy. Once these five isomers were identified, it was a matter of ascertaining whether all of them contributed to the observed measurements. A neon matrix IR spectrum was recorded using the same sample that was used for the electronic spectra. Comparison of calculated IR spectra, of the five isomers, to this spectrum ruled out the presence of ClBd and ClBe isomers. Figure 5.8 shows all the calculated spectra as well as the experimental trace. Further calculations were

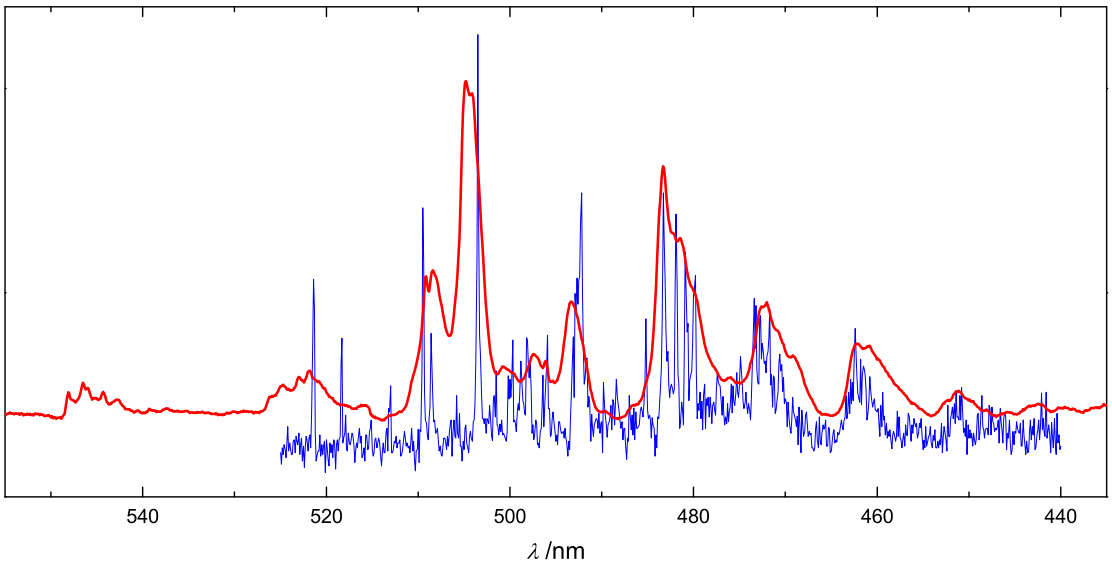

Figure 5.8: A comparison of the $^2A' \leftarrow {}^2A''$ electronic spectrum of $C_4H_3Cl^+$ measured in the gas phase in the ion trap (blue trace) with the one from matrix (red trace). The latter has been shifted by about 2.4 nm to the blue to match the gas phase vibrational band at 483.27 nm. Comparison of the two helped explain the broad absorption bands in the matrix spectrum. The assignments are given in Table 5.4.

done to determine excitation energies of the different isomers using time-dependent DFT and coupled cluster routines. Higher level CC2 calculations predicted one electronic transition per isomer in the visible. Therefore, the three bands observed at 550.5, 524.4 and 507.2 nm in the matrix were concluded to be due to three different isomers. Test CC2 calculations at the same level of theory done for the known $C_4H_4^+$ ion showed that the experimentally observed transitions are about 0.5 eV lower in energy than the computed ones. Taking this into account, the band system with its origin at 507.2 nm was assigned to $ClBa^+$. The transitions at 524.4 and 550.5 nm were found to be due to $ClBb^+$ and $ClBc^+$ isomers. The results of these calculations are shown in Table 5.5. Upon identification of the three isomers, the next step was to elucidate their structures by rotationally resolving their origin band. The isomer $ClBc^+$ was not observed in the gas phase. The origin band of $ClBa^+$ showed no discernible rotational profile even when a dye laser of bandwidth 0.15 cm^{-1} was used. This indicated a lifetime of the order of

Table 5.4: Assignment of $C_4H_3Cl^+$ isomers in a neon matrix and in the gas phase to observed band maxima

λ_{Ne}/nm	λ_{air}/nm	$\tilde{\nu}$/cm^{-1}	$\delta\tilde{\nu}$/cm^{-1}	Assignment
550.50		18 160	0	(1) $^2A' \leftarrow {}^2A''$ ClBc$^+$
528.50		18 196	756	$2\nu_{17}$
524.40	521.30	19 177	0	(1) $^2A' \leftarrow {}^2A''$ ClBb$^+$
	518.34	19 287	110	ν_{13}
	513.08	19 485	308	ν_{12}
511.60	509.51	19 621	444	$\nu_{13}+ \nu_{12}$
510.80	508.60	19 656	479	
503.10	501.51	19 934	757	ν_{10}
	498.79	20 043	866	ν_9
	498.15	20 069	892	$2\nu_{13}+ 2\nu_{12}$
498.40	495.92	20 159	982	ν_8
	485.20	20 604	1427	ν_5 or $\nu_8+\nu_{12}+\nu_{13}$
	474.88	21 052	1875	$\nu_5+\nu_{12}+\nu_{13}$
507.20	503.49	19 856	0	(1) $^2A' \leftarrow {}^2A''$ ClBa$^+$
499.80	499.73	20 005	149	ν_{13}
495.70	492.20	20 311	455	ν_{11}
	488.41	20 469	613	$\nu_{13}+\nu_{11}$
485.7	483.27	20 687	831	$2\nu_{17}$
483.8	481.90	20 745	889	$2\nu_{11}$
	480.91	20 788	932	ν_9
	479.83	20 835	979	$\nu_{13}+2\nu_{17}$
	477.38	20 942	1086	$\nu_{13}+\nu_9$
	473.37	21 119	1263	$\nu_{11}+2\nu_{17}$
474.5	472.71	21 149	1293	ν_6
	471.72	21 193	1337	$3\nu_{11}$
	470.68	21 240	1384	$\nu_{11}+\nu_9$
464.6	462.34	21 623	1767	$\nu_9+2\nu_{17}$
463.2	461.44	21 665	1809	
453.6	451.49	22 147	2291	$\nu_{11}+2\nu_9$
	450.84	22 175	2319	

a few hundred picoseconds. However, a high resolution scan of the origin band of the ClBb$^+$ isomer showed partially resolved features, the linewidth in the spectra being lifetime broadened. The origin bands of both isotopologues were measured

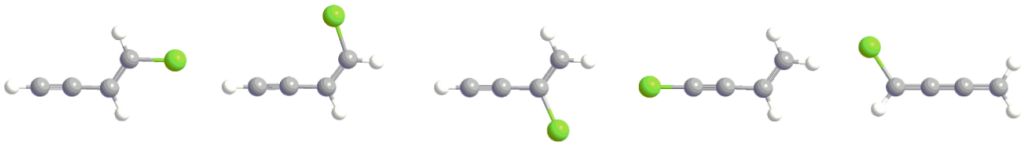

Method	ClBA	ClBB	ClBC	ClBD	ClBE
B3LYP	0 (0)	1.6 (5.2)	9.4 (33.9)	25.1 (16.0)	16.6 (0.7)
BLYP	0 (0)	1.5 (5.4)	8.7 (33.5)	24.9 (15.7)	6.2 (-4.6)

Figure 5.9: Relative energy (kJ mol^{-1}, zero-point correction included) of C_4H_3Cl isomers and their cations (in parentheses) calculated with DFT (B3LYP and BLYP potentials) and MP2 methods using the cc-pVTZ basis set. All structures are of C_s symmetry except $ClBe^+$ (C_1). The neutrals and cations were checked for triplet or quartet ground states, respectively. Two other isomers, H_3C_4Cl and ClH_2C_4H, are not shown; both lie $\sim$200 kJ mol^{-1} to higher energy.

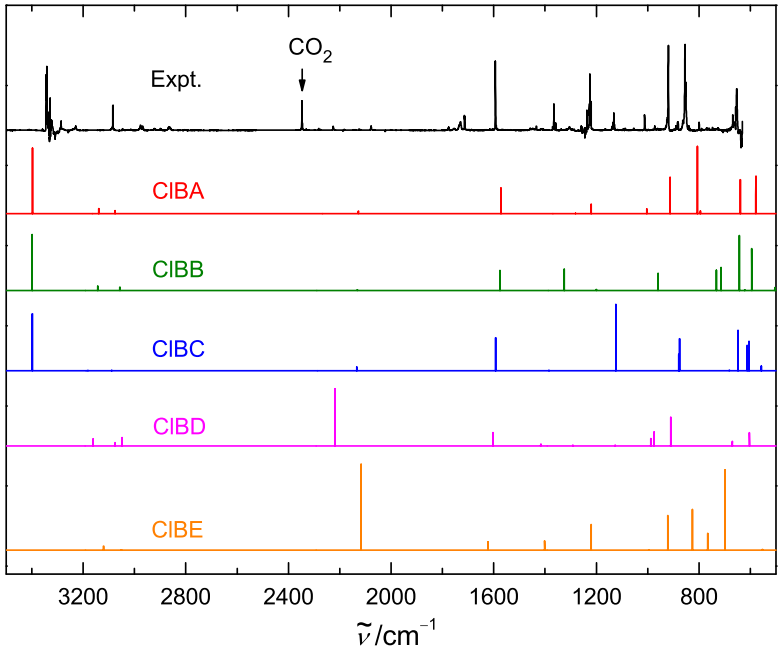

Figure 5.10: Neon matrix IR spectrum of C_4H_3Cl sample used in this study and theoretical vibrational spectra obtained with DFT at the B3LYP/cc-pVTZ level of theory. Bands of HC_4H were removed from the experimental trace.

and are shown in Figure 5.9. Besides a small isotope induced shift and narrower bands for ^{37}Cl, the spectra are identical. The trap temperature was raised to 50 K and the same spectrum was measured for the ^{35}Cl isotopologue. These two

Table 5.5: Excited state symmetries, vertical excitation energies Δ E and transition oscillator strengths f computed with two methods for the considered $C_4H_3Cl^+$ isomers and the experimental data. The values for structurally similar $C_4H_4^+$ ion are shown for comparison.

	TD DFT//B3LYP/cc-pVTZ		CC2//MP2/cc-pVTZ		
Exc. st.	Δ E/eV	f	Δ E/eV	f	Expt./eV
$ClBa^+$ (C_s, X^2A")					
(1) $^2A'$	2.86	0.058	2.94	0.10	2.46
(2) $^2A'$	4.26	0.30	4.27	0.45	3.62
(3) $^2A'$	4.35	0.082	4.83	0.011	
$ClBb^+$ (C_s, X^2A")					
(1) $^2A'$	2.73	0.035	2.80	0.057	2.38
(2) $^2A'$	4.16	0.14	4.22	0.30	
(3) $^2A'$	4.33	0.15	4.73	0.40	
$ClBc^+$ (C_s, X^2A")					
(1) $^2A'$	2.17	0.050	2.47	0.077	2.25
(2) $^2A'$	3.90	0.020	4.25	0.087	
(3) $^2A'$	4.83	0.077	5.23	0.13	
(4) $^2A'$	4.95	0.11			
$ClBd^+$ (C_s, X^2A")					
(1) $^2A'$	2.89	0.060	2.84	0.11	
(2) $^2A'$	4.37	0.29	4.50	0.40	
(3) $^2A'$	4.80	0.024			
$ClBe^+$ (C_1, X^2A)					
(1) ^2A	1.73	0.0010	2.86	0.023	
(2) ^2A	2.70	0.0033	3.88	0.0012	
(3) ^2A	3.25	0.066	3.92	0.52	
(4) ^2A	3.87	0.13	5.01	0.0082	
(5) ^2A	4.39	0.015			
(6) ^2A	4.62	0.011			
(7) ^2A	4.66	0.068			
$C_4H_4^+$ (C_s, X^2A")					
(1) $^2A'$	3.06	0.034	2.97	0.060	2.41
(2) $^2A'$	4.75	0.26	4.90	0.29	

measurements were used for fitting the simulated profile. The rotational constants were determined from the fit and are listed in Table 5.6.

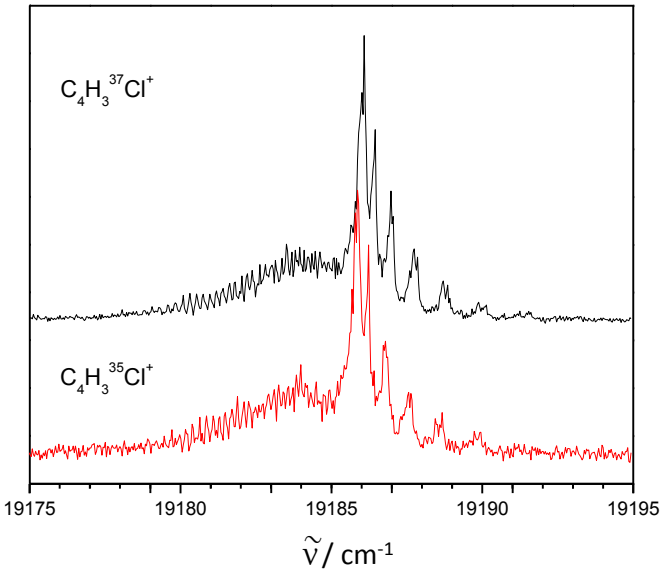

Figure 5.11: Rotationally resolved origin band of the $^2A' \leftarrow {}^2A''$ electronic transition of the two isotopologues of *cis*-1-chlorobutenynylium ClBb$^+$ isomer.

Table 5.6: Molecular constants (in cm^{-1}) of *cis*-1-chlorobutenynylium ClBb$^+$ determinced from a non-linear, least-squares fitting routine assuming a *c*-type $^2A' \leftarrow {}^2A''$.

Molecular constants/ cm^{-1}	
T_{00}	19 184.680(5)
A''	1.530
B''	0.051
C''	0.050
e''_{aa}	0.1
e''_{bb}	0.005
A'	1.638(1)
B'	0.049(1)
C'	0.048(1)
e'_{aa}	0
e'_{bb}	0

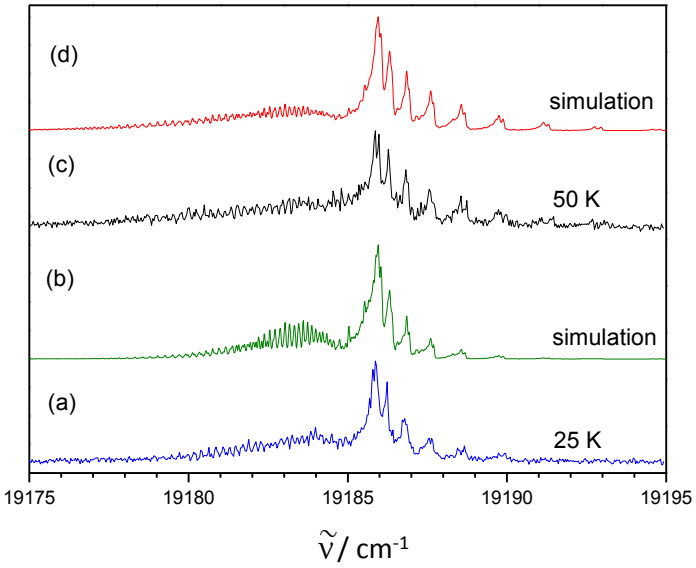

Figure 5.12: Origin band of the *c*-type $(1)^2A' \leftarrow {}^2A''$ electronic transition of *cis*-1-chlorobutenynylium $ClBb^+$ recorded with a one-colour two photon fragmentation technique. Traces (a) and (c) are at rotational temperatures of 25 and 50 K; traces (b) and (d) are the simulated spectra.

Therefore, while the matrix spectrum was the sum of contributions from three different isomers, only two of them were observed in the gas phase. [15] Since the same chemical sample was used for both experiments, the difference can be attributed to ionisation processes. The hot cathode discharge source employed in the matrix studies operates at higher temperatures than the electron impact source used for the ion trap studies, making other isomers accessible through rearrangement.

5.4 The $S_1 \leftarrow S_0$ electronic spectrum of $C_6H_7^+$

5.4.1 Introduction

One of the most common classes of organic reactions is aromatic electrophilic substitution that proceeds through the formation of a protonated intermediate. The latter has the general formula AH^+, where A is an aromatic core. They have been detected in several extreme media, for example in jet engine gas exhaust and hydrocarbon plasmas. [16] They have been considered to be possible carriers of the unidentified IR emission bands in interstellar media. The simplest ion of this category is the protonated benzene, $C_6H_7^+$. Its presence has been confirmed in the ionosphere of Titan by mass spectrometry.

Of the three possible structures for $C_6H_7^+$, the so called σ-complex was found to be the most stable. [17] This conclusion is based on evidence from IR studies done in the gas phase on its complexes with Ar [18] and N_2. In this structure the proton is covalently bonded to a carbon atom in the ring which develops a partial sp^3 hybridisation to accommodate it. Recently, electronic transitions of $C_6H_7^+$ were measured in a neon matrix and several isomers were found to contribute. Besides the σ-complex, these experiments identified another isomer, the α-protonated fulvene. This study used a variety of precursors to generate the $C_6H_7^+$. The electronic transitions of these two isomers overlap in the UV which could make it difficult to distinguish them, especially because they were produced concomitantly from different starting precursors. [19]

For the studies in the ion trap, $C_6H_7^+$ was generated by dehydrogenation of 1,3-cyclohexadiene induced by electron bombardment. The dissociation energy of the ion is known to be around 2.74 eV, above which loss of an H or H_2 occurs. The $S_1 \leftarrow S_0$ transition, at 3.54 eV lies above the thermodynamic threshold, which implies that absorption of one photon is sufficient to induce electronic excitation followed by dissociation of the ion.

5.4.2 Results and Discussion

The electronic spectrum of $C_6H_7^+$ measured by one photon dissociation is shown in Figure 5.11. As discussed earlier, loss of H/H_2 was monitored. Two band systems have been observed. Both of them are broad with vibrational features superimposed on the continuum.

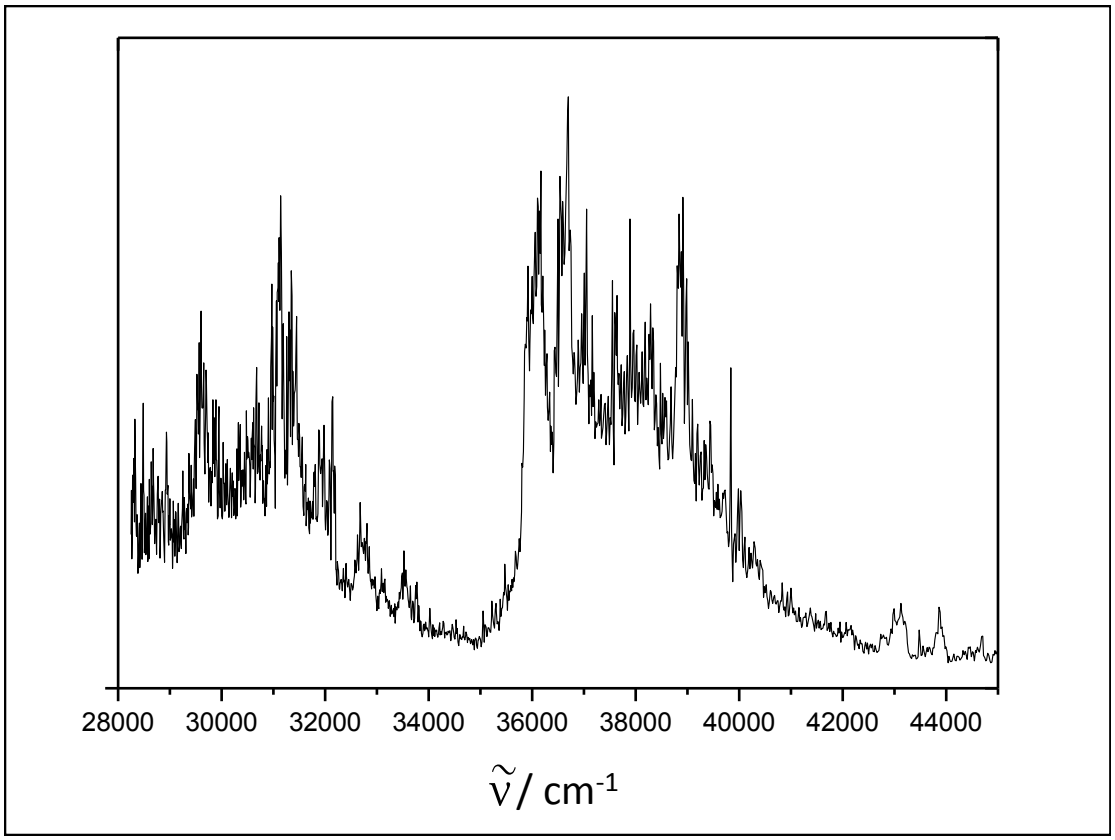

Figure 5.13: The $S_1 \leftarrow S_0$ electronic spectrum of $C_6H_7^+$

The profile corresponds very well to an earlier photodissociation experiment, where the ions were held at room temperature. [20] However, the relative intensities of the bands appear to be inverted in the low temperature experiment. A recent theoretical work has suggested assignments for these bands. [21] The band with an onset at 300 nm is because of an $S_1(A^1B_2) \leftarrow S_0(X^1A_1)$ transition. However, the assignment of the higher energy state was not straightforward. It could be because of an optically forbidden transition to the S_2 state which becomes

allowed due to vibronic coupling. The other possibility is absorption occurring to the allowed S_3 state. The authors argue that the latter is more likely suggesting that calculations may overestimate the magnitude of energy. Upon referring to the latest matrix results, possibility of contribution of the protonated fulvene cannot be entirely ruled out. Further experiments are necessary to characterise the observed spectrum and identify if there is more than one isomer undergoing absorption in the trap.

5.5 Summary of photodissociation spectroscopy

The photodissociation scheme works well with smaller molecules. Depending on the molecule, different approaches had to be adopted. For a molecule like N_2O^+, one colour predissociation was used. The photon promotes excitation to a higher electronic state which then undergoes internal conversion to a repulsive state. Dissociation occurs from the second one. In some of the other cations like $C_6H_4Cl_2^+$, [22] two photons of the same colour were sufficient to induce electronic absorption and subsequent loss of Cl atom. The mechanism has been envisaged as excitation followed by fast internal conversion resulting in accumulation of population in the high vibrational levels of the ground electronic state with a total internal energy content greater than the fragmentation threshold. For the electronic transitions of cationic polyacetylenes ($HC_{2n}H^+$) and protonated polyacetylenes ($H_2C_{2n}H^+$) two different colours, temporally and spacially overlapped were used. Once again, the first photon induced electronic excitation while fragmentation was initiated by the second one. [7] Following the first absorption, the excited state population underwent fast internal conversion to higher vibrational manifold of the electronic ground state or an intersystem crossing to close lying triplet or quartet states. Dissociation occurred via absorption of the second photon from either of these two states. The depopulation of higher electronic states to which the first excitation happens via non-radiative decay pathways becomes more efficient in larger molecules because of the many close lying states. For example, the fluorescence lifetime of the $A^2\Pi$ state falls from 71 ns to less than 6 ns on going from HC_4H^+ to HC_8H^+. [7] This is a clear indication of the increasing efficiency of non-radiative pathways.

Measuring electronic spectra of PAHs under conditions relevant to the ISM was one of the major motivations behind construction of the 22-pole trap machine. The resonant two-colour, two-photon dissociation scheme was tried on such ions with nano-second lasers. However, efficient intramolecular vibrational relaxation (IVR) in these ions proved to be a major barrier. The excitation energy is distributed efficiently over the entire molecule due to coupling between different vibrational

modes. The larger is the ion, greater the density of states and hence easier the redistribution. Hence, the second photon failed to promote dissociation . Absorption of several photons would then be necessary to build up enough energy in a single bond to induce its fragmentation. This increases the timescale for the observation of a fragment ion by several orders of magnitude. Multiphoton dissociation spectra can be used as another option, but the width of absorptions in such a spectrum would render comparison with astronomical data unsuccessful.

Bibliography

[1] J. Krełowski, Y. Beletsky, G. A. Galazutdinov, R. Kołlos, M. Gronowski, and G. LoCurto. Evidence for Diacetylene cation as the carrier of a Diffuse Interstellar Band. *Astrophys. J. Lett*, 714:L64, 2010.

[2] T. Motylewski, H. Linnartz, O. Vaizert, J. P. Maier, G. A. Galazutdinov, F. A. Museev, J. Krełowski, G. A. H. Walker, and D. A. Bohlender. Gas-phase electronic spectra of carbon-chain radicals compared with diffuse interstellar band observations. *Astrophys. J.*, 531:312, 2000.

[3] B. J. McCall, K. H. Hinkle, T. R. Geballe, G. H. Moriarty-Schieven, N. J. Evans II, K. Kawaguchi, S. Takano, V. V. Smith, and T. Oka. Observations of H_3 in the Diffuse Interstellar Medium. *Astrophys. J.*, 567:391, 2002.

[4] J. P. Maier, N. M. Lakin, G. A. H. Walker, and D. A. Bohlender. Detection of C3 in Diffuse Interstellar Clouds. *Astrophys. J.*, 553:267, 2001.

[5] R. Kuhn, J. P. Maier, and M. Ochsner. Absolute rotational assignment of the origin band of the $\tilde{A}^2\Pi$ transition of the diacetylene cation. *Mol. Phys.*, 59:441, 1986.

[6] J. P. Maier, S. Chakrabarty, F. J. Mazzotti, C.A. Rice, R. Dietsche, G. A. H. Walker, and D. A. Bohlender. Assignment of 5069 Å diffuse interstellar band to HC_4H^+: disagreement with laboratory absorption band. *Astrophys. J. Lett.*, 729:L20, 2011.

[7] A. Dzhonson, E. B. Jochnowitz, and J. P. Maier. Electronic Gas-Phase Spectra of Larger Polyacetylene Cations. *J. Phys. Chem. A*, 111:1887, 2007.

[8] D. Klapstein, R. Kuhn, J. P. Maier, M. Ochsner, and W. Zambach. Emission and Laser Excitation Spectra of the $A^2\Pi_g \leftrightarrow X^2\Pi_u$ Transition of Rotationally Cooled Triacetylene Cation. *J. Phys. Chem*, 88:5176, 1984.

[9] S. Chakrabarty, C. A. Rice, F. J. Mazzotti, R. Dietsche, and J. P. Maier. Electronic absorption spectrum of triacetylene cation for astronomical considerations. *J. Phys.Chem. A*, 2013.

[10] P. Cias, O. Vaizert, A. Denisov, J. Mes, H. Linnartz, and J.P. Maier. Electronic Gas-Phase Spectrum of the Pentaacetylene Cation. *J. Phys. Chem. A*, 106:9890, 2002.

[11] R. Vestin, A. Borg, and T. Lindblom. Chlorobutatriene - Identification and Spectrochemical Characterization. *Acta. Chem. Scand.*, 22:685, 1968.

[12] R. Vestin, A. Borg, and T. Lindblom. Three Isomeric Chlorobutenynes. *Acta. Chem. Scand.*, 22:687, 1968.

[13] F. Karlsson, M. Granberg, and R. Vestin. Microwave Spectrum, Structural Parameters and Nuclear Quadrupole Coupling of cis-1-Chlorobuten-3-yne. *Acta. Chem. Scand.*, 29a:855, 1975.

[14] A. Borg and P. Cederbalk. The Vibrational Spectrum of 4-chlorobuten-3-yne. *Acta. Chem. Scand.*, 40a:113, 1986.

[15] S. Chakrabarty, V. Rudnev, J. Fulara, R. Dietsche, A. Nagy, I. Garkusha, F. J. Mazzotti, C. A. Rice, and J. P. Maier. Electronic spectra of $C_4H_3Cl^+$ isomers. *Mol. Phys.*, 110:194307, 2012.

[16] O. Dopfer. *Laboratory Spectroscopy of protonated PAH molecules relevant for Interstellar Chemistry, PAHs and the Universe*, volume 46. 2011.

[17] N. Solca and O. Dopfer. Protonated Benzene: IR Spectrum and Structure of $C_6H_7^+$. *Angew. Chem. Int. Ed.*, 41:3628, 2002.

[18] G. E. Douberly, A. M. Ricks, P. v. R. Schleyer, and M. A. Duncan. Infrared Spectroscopy of Gas Phase Benzenium Ions: Protonated Benzene and Protonated Toluene, from 750 to 3400 cm^{-1}. *J. Phys. Chem. A*, 112:4869, 2008.

[19] I. Garkusha, J. Fulara, A. Nagy, and J. P. Maier. Electronic Transitions of Protonated Benzene and Fulvene, and of C_6H_7 Isomers in Neon Matrices. *J. Am. Chem. Soc.*, 132:14979, 2010.

[20] B. S. Freiser and J. L. Beauchamp. Photochemistry of Organic Ions in the Gas Phase. Comparison of the Gas Phase Photodissociation and Solution Absorption Spectra of Benzoyl Cation, Protonated Benzene, and Protonated Mesitylene. *J. Am. Chem. Soc.*, 98:3136, 1976.

[21] M. F. Rode, A. L. Sobolewski, C. Dedonder, C. Jouvet, and O. Dopfer. Computational Study on the Photophysics of Protonated Benzene. *J. Phys. Chem. A*, 113:5865, 2009.

[22] A. Dzhonson, D. Gerlich, E. Bieske, and J. P. Maier. Apparatus for the study of electronic spectra of collisionally cooled cations: para-dichlorobenzene. *J. Mol. Struct.*, 795:93, 2006.

6 Laser Induced Charge Transfer (LICT)

More general alternative methods of measuring electronic spectra were sought for after the photodissociation scheme was found unsuitable for larger ions. The first method tried was laser induced charge transfer (LICT). In the early 80s, a rotationally resolved $A^2\Pi(v'=4) \leftarrow X^2\Sigma(v''=0)$ electronic spectrum of N_2^+ was recorded by inducing CT to Ar. [1] Charge exchange between ground state N_2^+ and Ar is endothermic by 0.18 eV. The CT rate coefficient for $X^2\Sigma(v''=0)N_2^+$ in $v=0$ level at room temperature has been determined to be $<10^{-12}\,cm^3\,s^{-1}$. Vibrationally excited N_2^+ has a much higher rate constant ($4\times10^{-10}\,cm^3\,s^{-1}$). [2] A general illustration of this technique is shown in Figure 6.1. Absorption of a photon promotes electronic excitation of the ion BC^+. Charge exchange occurs when such an ion collides with the neutral. This reaction is endothermic when the ion is in the electronic ground state. The spectrum of BC^+ is then produced by counting the number of A^+ ions as a function of excitation frequency.

6.1 $NCCN^+$ + Ar

6.1.1 Introduction

The following electronic transitions of $NCCN^+$ ion have been studied previously in an ion-trap by photodissociation: $D^2\Pi_u, C^2\Pi_u, B^2\Sigma_u^+ \leftarrow X^2\Pi_g$. [3,4] The $D^2\Pi_u$ state lies above the dissociation threshold of the cation and was accessible by one photon absorption. Absorption of two photons of the same colour was necessary

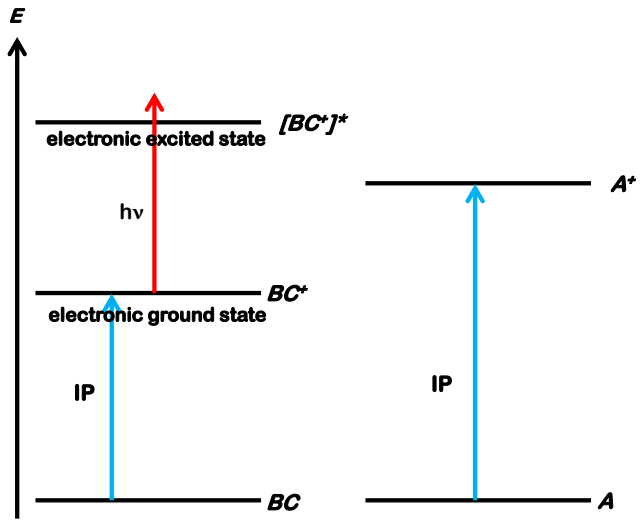

Figure 6.1: The generic molecule BC undergoes ionisation to produce BC^+ in the ground state.

to excite the ion to the $C^2\Pi_u$ and subsequently fragment it, while the $B^2\Sigma_u^+$ state was studied by a two colour two photon scheme. These electronic states and their corresponding energies are shown in Figure 6.2. In order to measure LICT spectrum of $NCCN^+$, the $C^2\Pi_u$ and $D^2\Pi_u$ states were chosen. The ion possesses a total internal energy of 15.53 eV and 17.51 eV in these two states respectively. The IP of Ar is 15.53 eV, these transitions were suitable candidates to try the LICT approach. $NCCN^+$ ions were created by electron bombardment of the neutral molecule. For these experiments, the trap was held at 120 K to prevent condensation of Ar which were introduced continuously through a leak valve. Ar served as both the neutral and charge exchange partner. Ions were allowed to undergo collisional relaxation for 60 ms, following which they were probed with laser. All the measurements done in this section were recorded by counting the number of C_2^+ fragments to compare with earlier measurements at 15 K. To generate the LICT spectrum, Ar^+ was detected.

6.1.2 Results and Discussion

6.1.2.1 The $C^2\Pi_u \leftarrow X^2\Pi_g$ electronic spectrum of $NCCN^+$

Figure 6.3 shows the $C^2\Pi_u \leftarrow X^2\Pi_g$ electronic spectrum of $NCCN^+$ measured under three different conditions. Trace (c) is the fragmentation spectrum measured at 10 K. The vibrational transitions are narrow because of collisional cooling with helium. Details of the spectrum are described elsewhere. The origin band lies at 17 363 cm^{-1}. The small absorption feature to the red of the origin band is most likely beacuse of a transition to the vibrational manifold of the $B^2\Sigma_u^+$ state. The spectrum shows progressions in ν_2 and combination bands in ν_3 and ν_5. The same features are observed in the spectrum at 120 K except for broadening due to temperature. This spectrum was not power corrected and as a result some of the weaker features showed more than expected intensity because of power saturation. The spectrum obtained by CT to Ar reproduces the same basic pattern; however, there are some significant differences. It appears that some of the finer features are smeared out in this spectrum, indicating some additional broadening factor. For example the vibrational band arising from $B^2\Sigma_u^+$ state is no longer discernible. Once the first photon has been absorbed, the excited ion has two pathways available to it. It can either absorb another photon and undergo bond cleavage or it can transfer its charge to Ar neutrals. Traces (a) and (b) in Figure 6.2 were observed under identical experimental conditions only by switching the mass channel on the second quadrupole for data acquisition. This implied that dissociation and charge exchange competed with one another or, the former occurred first and the fragments were sufficiently energetic to ionise Ar. From the linewidth of transitions of the fragmentation spectrum, a lifetime of the order of femtoseconds was concluded for the excited state. Absorption of the second photon must have happened immediately after- from the same pulse of the nano second laser- for the fragmentation to occur. Based on these facts, it seems that dissociation preceded charge exchange and the latter is induced from collisions with fragments (C_2^+) and not the parent ions.

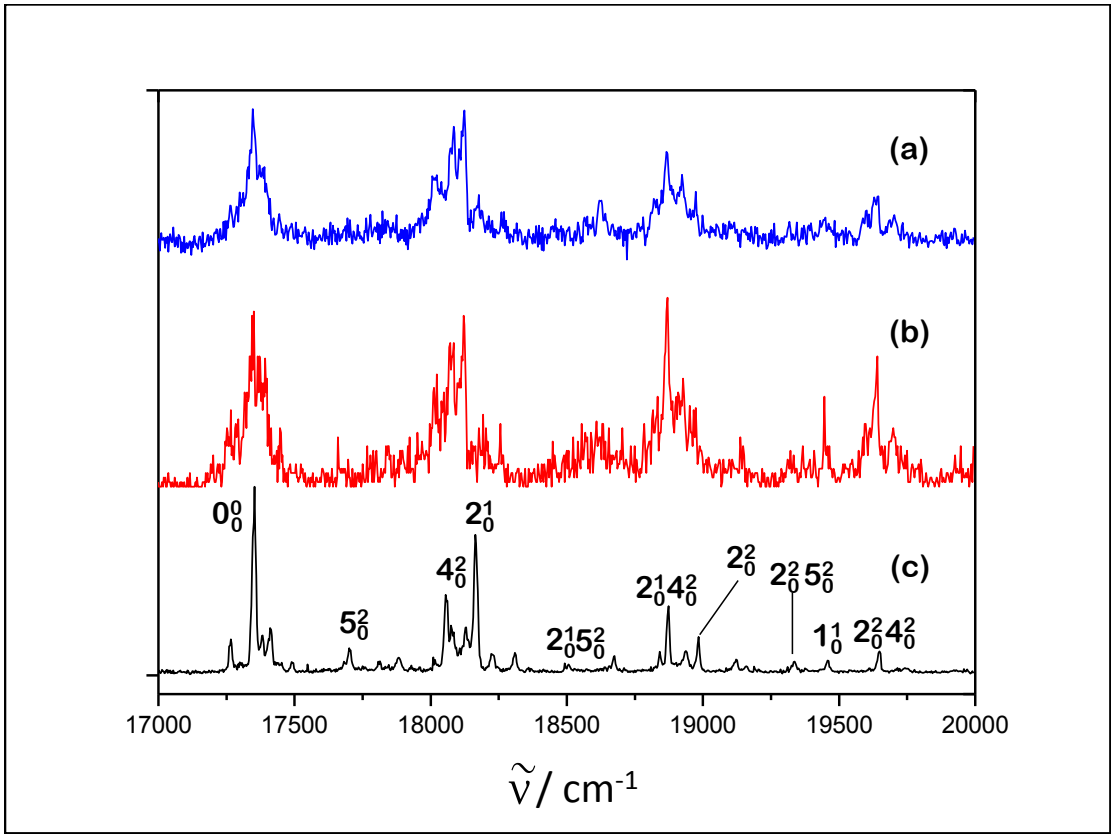

Figure 6.2: The $C^2\Pi_u \leftarrow X^2\Pi_g$ electronic spectrum of $NCCN^+$. Trace (c) is the fragmentation spectrum obtained by monitoring the loss of C_2^+ products at 10 K. Trace (b) is the same spectrum at 120 K. Trace (a) was obtained by monitoring laser induced charge transfer to Ar.

6.1.2.2 The $D^2\Pi_u \leftarrow X^2\Pi_g$ electronic spectrum of $NCCN^+$

Figure 6.3 is a compilation of the $D^2\Pi_u \leftarrow X^2\Pi_g$ electronic spectrum of $C_2N_2^+$ measured under three different conditions. The bottom two traces are fragmentation spectra at two different temperatures. The strongest peak to the red at 33 409 cm^{-1} is assigned as the origin band. The width of the band is attributed to fast internal conversion. A vibrational progression in ν_2 is observed along with combination bands. The features above 37 000 cm^{-1} in trace (b) are due to saturation.

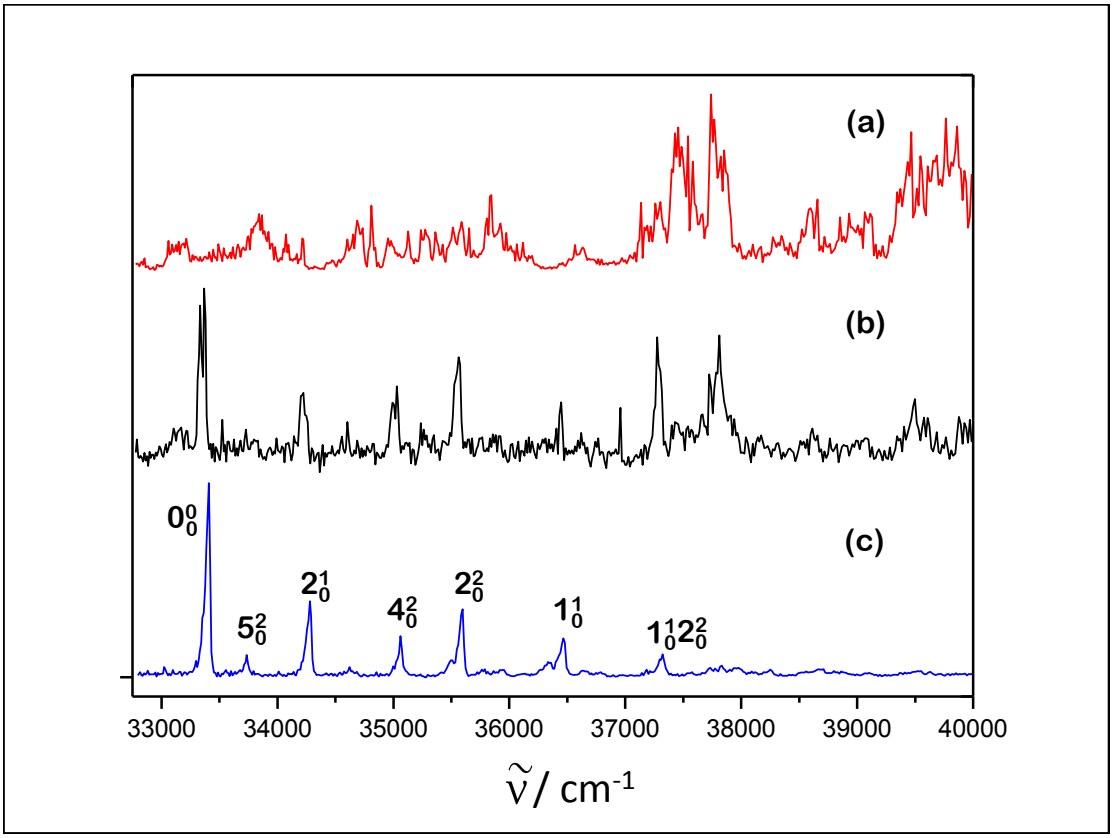

Figure 6.3: The $D^2\Pi_u \leftarrow X^2\Pi_g$ electronic spectrum of $NCCN^+$. Traces (c) and (b) are photodissociation spectrum measure at 10 and 120 K respectively. Trace (a) was obtained by laser induced charge transfer to Ar neutrals.

Trace (a) does not reflect the absorption features observed in the other two. Dissociation from the $D^2\Pi_u$ state is a one photon process, in which case it is complete before collision with the neutral partner occurs. As the expected bands are not observed, in a collision between a fragment ion and Ar, charge transfer is not necessarily the preferred mechanism for energy dissipation. This may indicate that even when energetics are favourable for such a process to occur, other factors may be more dominant. Charge transfer becomes more favoured above 37 000 cm^{-1}. However, it is difficult to conclude whether this happens from the fragments or from a very high vibrational level in the $D^2\Pi_u$ state as the fragmentation spectrum does not show absorption in this region. For a detailed understanding, it

may be necessary to look into potential energy surfaces of parent, fragment and charge exchange products.

6.2 1,4-dichlorobenzene cation + $C_6H_5NO_2$ and CH_2Cl_2

6.2.1 Introduction

In an earlier study the $B^2B_{3u} \leftarrow X^2B_{2g}$ electronic spectrum of 1,4-dichlorobenzene cation was measured by monitoring the loss of a Cl atom. [5] The lowest frequency transition at 19 622 cm^1 was assigned as the origin band. A progression was observed in ν_6, which also showed combination bands with ν_{30}, ν_{17} and ν_4. The photodissociation was thought to occur via a sequential excitation/internal conversion process where the cation absorbed two photons of the same colour. Once again, the ions were produced by electron impact of the neutrals. Since both the charge exchange partners chosen here were organic compounds, the measurements were done at room temperature. These molecules were nitrobenzene ($C_6H_5NO_2$) and dichloromethane (CH_2Cl_2). Nitrobenzene ionises at 9.94 eV while the IP of dichloromethane is 11.33 eV. Upon electronic excitation, 1,4-DCB$^+$ gains 2.4 eV on top of the 8.95 eV necessary for ionisation. Therefore, after the absorption of the first photon the ion has a total energy content of 11.35 eV, making it possible for it to undergo charge exchange with either of the chosen neutrals. Considering that internal conversion is very efficient, most of the excited state population collapses into the vibrational manifold of the X^2B_{2g} state. The question then is, whether the ion absorbs the second photon to undergo fragmentation or is charge exchange more favoured. If dissociation occurs first, then CT could happen between the newly fragment ion and the neutral.

6.2.2 Results and Discussion

The measured spectra are shown in Figure 6.4. The bottom most trace was measured by photodissociation, in which the number of fragment ions $C_6H_4Cl^+$ were counted. The other two traces were obtained by monitoring charge transfer. Interestingly, none of these spectra were observed at the expected masses. When $C_6H_5NO_2$, which has a m/z of 123, was introduced in the trap, absorption was seen at m/z 105. For CH_2Cl_2 with an m/z of 84, signal was observed at m/z 157. These observations indicate that instead of a simple charge transfer, laser induced reactions occur. Although similar to the photodissociation signal, it is

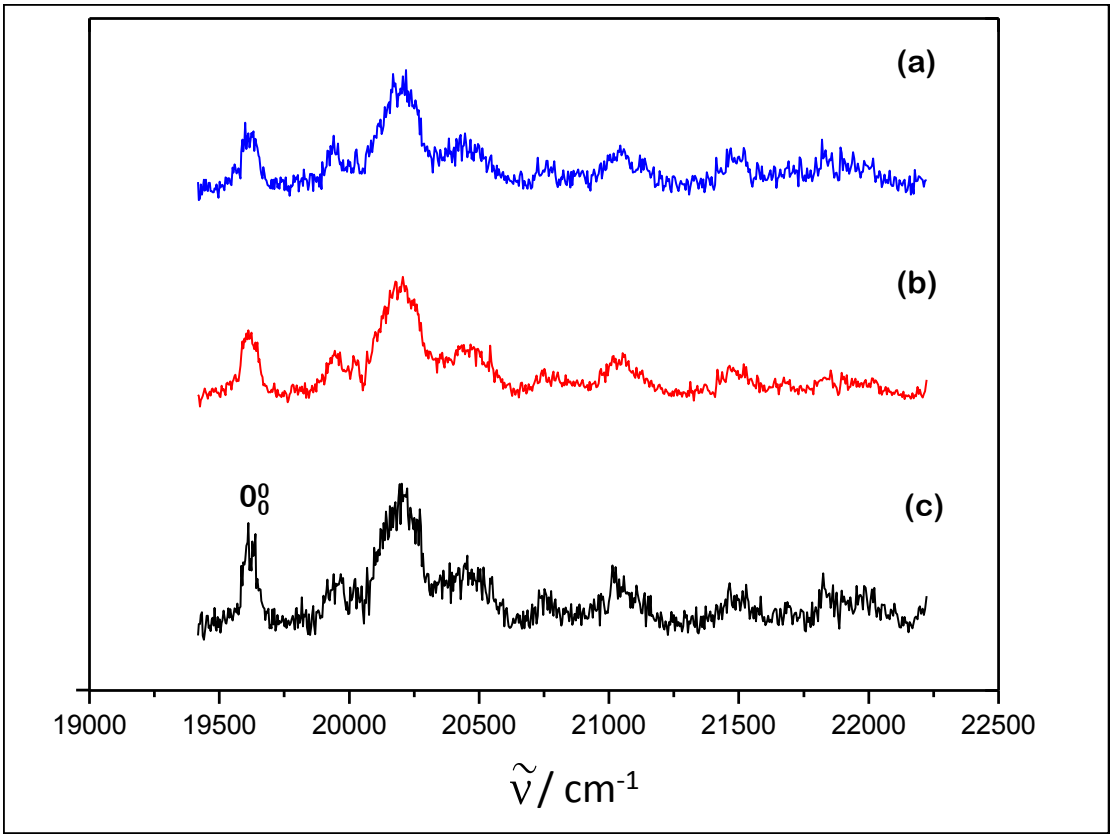

Figure 6.4: the $B^2B_{3u} \leftarrow X^2B_{2g}$ electronic spectrum of $C_6H_4Cl_2^+$. Traces (a) and (b) were recorded at 300 K to prevent condensation of the organic neutral partners. The bottom trace is a photodissociation spectrum also at 300 K to enable comparison with charge exchange spectrum.

not straightforward to explain the origin or composition of the ions that appear

at these unexpected masses. From a spectroscopic point of view, it is important to realise, that using a complex molecule as the neutral partner may not be ideal. The excess energy can be partitioned into several modes leading to opening up of more than one reaction channel. The temperature could have had an influence in addition because all the experiments were conducted at 300 K. Since both these neutrals have considerable vapour pressure at room temperature, they were leaked in directly into the trap. To ensure maximum S/N, measurements were done in a pure environment of the neutral partner. The mass ratio between the parent ion and buffer gas being unfavourable, relaxation was not efficient. In fact, this could have led to collisional activation of the neutral even before the ions were laser excited.

6.3 Discussion

The LICT method presents an elegant way of doing spectroscopy but it has its share of limitations. In order to do measurements on cold ions, it is necessary to prepare a supersonic beam of neutrals that can be pulsed into the trap without colliding against the walls. This requires careful alignment of the molecular beam arrangement with respect to the trap. One such setup has been shown in Figure 6.5. The other aspect and probably the more important one, is the choice of the neutral partner. Since the distribution of excess energy is easier to foresee in atoms, most successful charge transfer experiments to date have been carried out with these. Many of the large organic molecules have IPs below 10 eV, while their optical transitions are between 1.5-4 eV. Most atoms and simple molecules, that can be introduced into the trap in a molecular beam, are then energetically unfavourable for this scheme. Taking these into account, it seems LICT cannot be employed as a universal technique. The results presented within indicate that even when the neutral partner may be thermodynamically feasible, the transfer of an electron can be determined by other factors. Another possible handicap can be fast IVR which occurs efficiently in large ions. The total energy may be

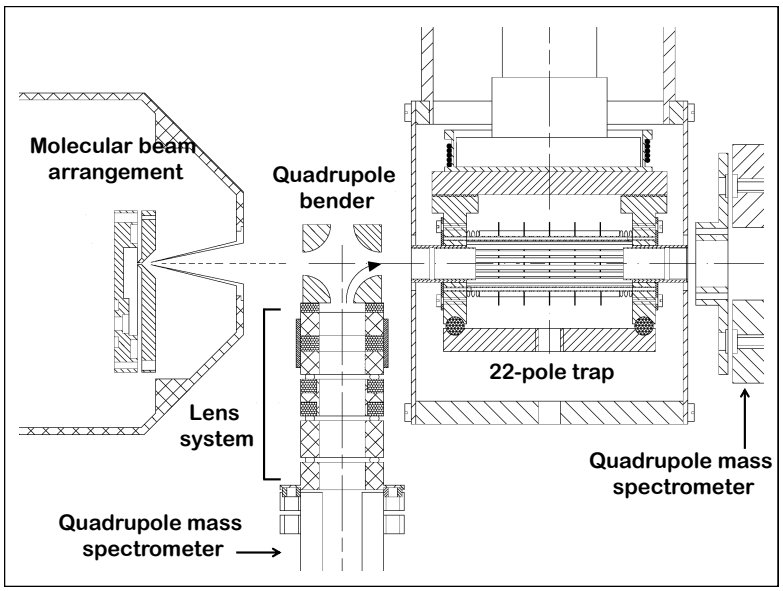

Figure 6.5: Experimental arrangement for LICT at low temperatures. The neutrals are introduced via a molecular beam while ions are injected into the trap by the bender. [6]

distributed at a rate faster than the capture procedure of the charge exchange process.

Bibliography

[1] J. C. Hansen, C. H. Kuo, F. J. Grieman, and J. T. Moseley. High resolution absorption spectroscopy of N_2^+ $X(v'' = 0) \rightarrow A(v' = 4)$ using charge exchange detection. *J. Chem. Phys.*, 79:1111, 1983.

[2] S. Schlemmer, T. Kuhn, E. Lescop, and D. Gerlich. Laser excited N_2^+ in a 22-pole ion trap: Experimental studies of rotational relaxation processes. *Int. J. Mass Spectrom.*, 185/186/187:589, 1999.

[3] C. A. Rice, V. Rudnev, S. Chakrabarty, and J. P. Maier. $D^2\Pi_u$, $C^2\Pi_u \leftarrow X^2\Pi_g$ electronic transitions of $NCCN^+$. *J. Phys. Chem. A*, 114:1684, 2010.

[4] V. Rudnev, C. A. Rice, and J. P. Maier. $B^2\Sigma_u^+ \leftarrow X^2\Pi_g$ electronic spectrum of $NCCN^+$ in the gas phase. *J. Chem. Phys.*, 129:134315, 2008.

[5] A. Dzhonson, D. Gerlich, E. Bieske, and J. P. Maier. Apparatus for the study of electronic spectra of collisionally cooled cations: para-dichlorobenzene. *J. Mol. Struct.*, 795:93, 2006.

[6] D.Gerlich. *Personal Communication*, 2000.

7 Laser Induced Inhibition of Complex Growth

7.1 Introduction

Van der Waals clusters of neutral molecules and ionic complexes between a wide variety of atoms or molecules have been the subject of extensive experimental characterisation over the last thirty years. [1] Mass selective techniques have enhanced derivation of structural information by allowing exact determination of cluster sizes and hence corresponding solvation numbers. [2] Electronic, vibrational and rotational spectroscopy have been performed to elucidate the nature of bonding and location of the partner atom/molecule with respect to the central one. Interest in ionic complexes, arises because of their ubiquitous presence in gaseous environments such as plasmas, flames and the atmosphere. [3] Clusters have been traditionally produced in the laboratory by a supersonic expansion of a gas mixture. The gas undergoes adiabatic expansion in vacuum which cools its rotational and translational degrees of freedom down to a few kelvins. In the initial part of the expansion, there is enough density of the interacting species to facilitate three body association reactions that lead to formation of clusters between the precursor molecule and the entrained neutral ligand. Subsequently, electron impact or photoionisation can be used for ionisation. Complexes involving an ionic core and a suitable neutral have also been formed in ion traps. [4–6] By varying storage times in the trap, ions can be allowed to interact for long durations with a well defined number of neutral atoms or molecules, which is usually also the buffer gas. Favourable rate coefficients are achieved by operating

the traps at temperatures below ∼10 K. The general reaction can be written as:

$$\mathrm{A^+ + 2B} \underset{\Gamma}{\overset{k_f n}{\rightleftharpoons}} [\mathrm{A^+ - B}]^* + \mathrm{B} \xrightarrow{\mathrm{k_s}} [\mathrm{A^+ - B}] + \mathrm{B}$$

The total formation rate is given by

$$R = k_3 n^2 \tag{7.1}$$

where k_3 is the ternary rate coefficient and n the neutral density. Quadratic dependence on the latter is a characteristic of three body collisions and provides direct experimental evidence of their occurrence. Typical values of k_3 range from 10^{-30} to $10^{-26}\,\mathrm{cm^6\ s^{-1}}$. [7] Hydrogen ion clusters with the general formula, H_n^+, where n = 5-23 have been observed in a 22-pole trap. [8] The same setup was used to produce $(\mathrm{CO})_n^+$ complexes, with n = 2-9. [9] In another experiment, $[\mathrm{Cl^-{-}CH_3Cl}]$ complexes were formed. [10] The temperature dependence of k_3 reveals information on coupling of degrees of freedom during collisions. Experimental results indicate that coupling often violates assumptions in statistical models used to explain them. For some cases like the formation of $(\mathrm{CO})_2^+$, dependence on temperature can be explained by statistical models. But deviations from this model was observed for the formation of $(\mathrm{CO})_3^+$. Association of $\mathrm{Cl^-}$ with $\mathrm{CH_3Cl}$ too showed deviation from statistical models. In the low density regime, the three body association constant can be expressed as,

$$k_3 = \frac{k_f k_s}{\Gamma} = k_f k_s \tau. \tag{7.2}$$

The formation rate k_f of the metastable complex is obtained from the Langevin collision rate for polarisable neutral species and by a modified rate of capture for polar molecules. The product of the capture collision rate and an often unknown stabilisation constant $\beta \leqslant 1$ gives the rate of stabilisation k_s. The lifetime $\tau = \Gamma^{-1}$ of the metastable complex can be determined experimentally if β is known. Assuming $\beta = 1$ has yielded lifetimes between 0.1 and 4 ns for the carbon monoxide

clusters at a temperature of 80 K. Similarly, the metastable complex $[Cl^- - CH_3Cl]^*$ was found to have a lifetime of the order of a few tens of picoseconds.

Several methods of indirect spectroscopy have been discussed in the introduction of this thesis. Vibrational predissociation spectra of different cations and anions have been measured over the last decade by tagging them with neutral atoms or molecules via three-body collisions. Well resolved IRPD spectra of metal oxide-rare gas atom complexes have been obtained in a cold hexadecapole trap. [11] These results are very good approximations to linear absorption spectra when the neutral atoms used were He or Ne. In other experiments, Ar, H_2, D_2, N_2, CH_4 and even H_2O have been employed. [12] For larger neutral molecules, significant perturbations are expected in the observed spectra. [13] These are seen as shifts in vibrational frequencies and relative stabilities of isomers. Such effects are undesirable in spectra intended for comparison to DIBs. The method described here relies on complex formation as well. The actual spectroscopic approach detects absorption of photon by the bare ion by counting the number of complexes as a function of laser frequency. The target molecule acquires internal energy and consequently undergoes complexation at a significantly reduced rate. Therefore, a drop in the complex number corresponds to an absorption in the parent ion.

To begin with, rare gas ions were used to form complexes. Helium was successfully attached to Ar^+ ion. The binding energy (B.E.) of this complex is $209\,cm^{-1}$. Ar^+ proved to be a simple case and for longer trapping times, attachment of two helium atoms were observed.

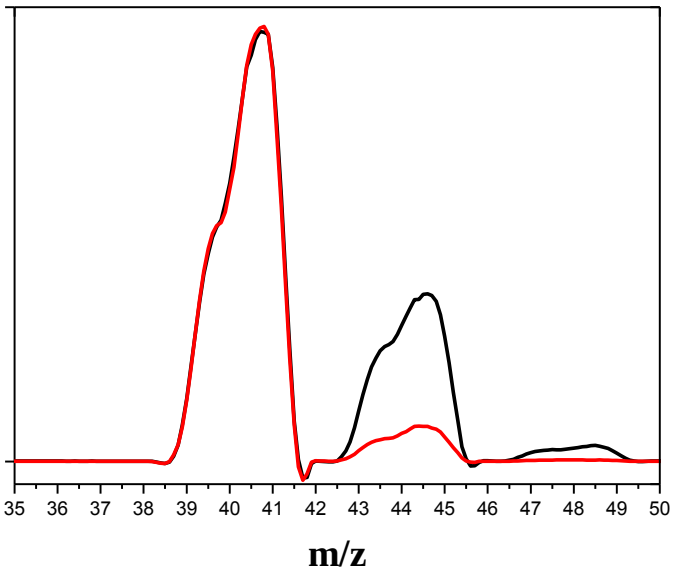

Figure 7.1: Mass spectrum showing the formation of Ar^+-He and Ar^+-He_2 complexes. The latter appear for longer storage times. The trace in red and black correspond to storage times of 80 and 940 ms respectively.

The efficiency of conversion was found to increase with pressure as well. This is illustrated with another example where complexes were observed to form between Xe^+ and Ne neutrals. The B.E. is 334 cm^{-1}.

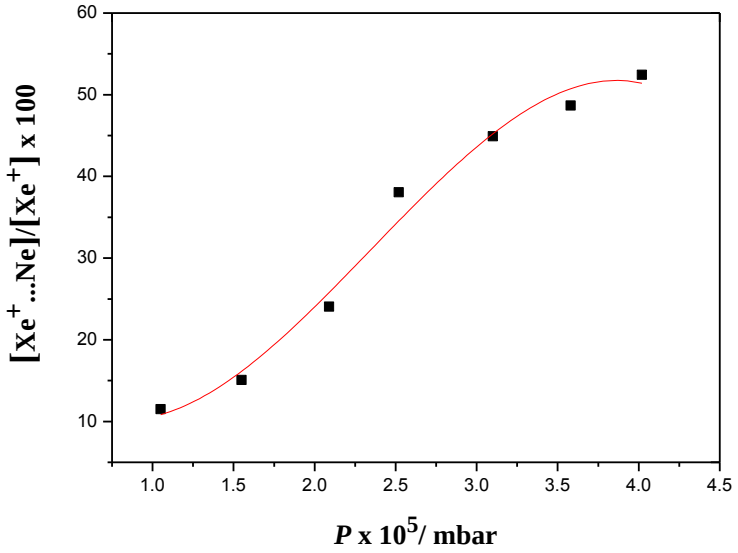

Figure 7.2: The percentage of Xe^+-Ne complexes increased with higher pressures of Ne in the trap.

Another typical diagnostic for ion complexes is to observe their behaviour with increase in temperature. The following figure is a compilation of mass spectra of H_2O^+ ions at three different trap temperatures of 5, 13 and 25 K.

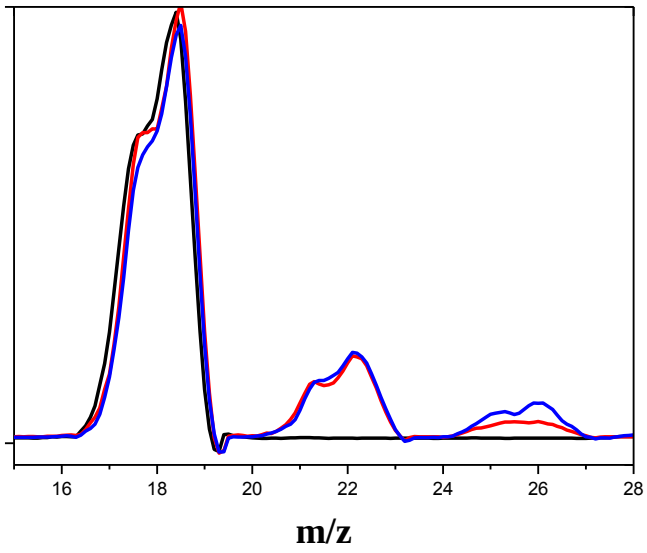

Figure 7.3: Mass spectra of H_2O^+ measured at three different temperatures; 5 K (blue), 13 K (red) and 25 K (black).

As expected, the complexes disappeared at elevated temperatures. All the above experiments were performed while helium was leaked into the trap continuously. N_2O^+ also showed attachment of one helium, although the conversion was not as efficient.

7.2 Proof of Principle: N_2^+

Cluster formation of N^+ with He was studied inside a 22-pole trap and the underlying kinetics was evaluated. The ternary rate constant was found to be $4.16\times10^{-31}\,cm^6s^{-1}$ at 15 ± 5 K. [14] The binding energy of N^+-He is $\sim1\,950\,cm^{-1}$. Efficient conversion was achieved because of high B. E. of the complex. To provide proof of principle for the LIICG method, it was necessary to start with a simple ion whose spectroscopy is well characterised. N_2^+ fulfilled this condition and even though its B.E. with He is an order of magnitude lower than atomic N^+, use of higher number densities of buffer gas led to appreciable conversion percentages.

The electronic spectroscopy of N_2^+ has been studied extensively. The ground state electronic configuration of the ion is $...(2\sigma_u^+)^2(1\pi_u)^4(3\sigma_g^+)^1$, which corresponds to a $^2\Sigma_g^+$ state. The first excited electronic state is $^2\Pi_u$. The transitions between these two states form the so called Meinel band system, which has received a lot of attention from very early on especially because it lies in a region accessible to cw lasers. [15] Several groups have studied transitions from the $v=0$ level of the X state to $v=0$-4 of the A state. The two states do not perturb each other because N_2^+ is homonuclear. The next excited level, $B^2\Sigma_u^+$, lies above $v=9$ of the A state. Therefore no perturbations from any of the higher states are expected when the lower vibrational levels of the A state are being studied. The observed transitions in this work and the corresponding spectroscopic notations are shown in Figure 7.4.

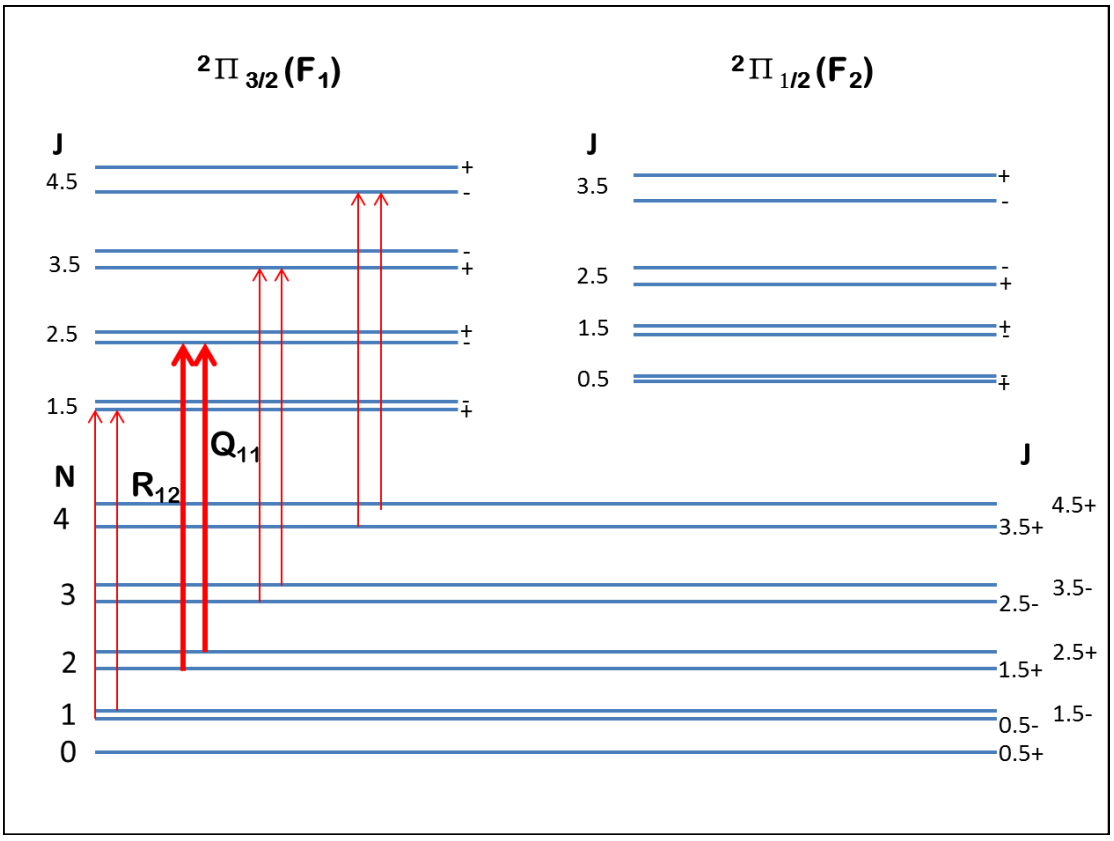

Figure 7.4: The energy levels of N_2^+ involved in the spectrum shown in Figure 7.7.

The spin components in each level are denoted by F_1 and F_2. The $^2\Sigma$ state corresponds to Hund' case (b), while $^2\Pi$ state belongs to case (a). Besides the bare ion, electronic spectra of the complexes $N_2^+-He_{n=1-3}$ and N_2^+-Ne have been measured in the region corresponding to the $B^2\Sigma_u^+ \leftarrow X^2\Sigma_g^+$ origin and 1-0 transitions of N_2^+. [1] Spectra were generated by monitoring the loss of rare gas atom(s) resulting in the formation of N_2^+ as a function of the irradiating wavelength. The charge exchange method that was utilised by Hansen et al, [16] was exploited to remeasure spectra of N_2^+ inside a 22-pole trap. [17] The ions were cooled to $\sim$120 K by collisions with Ar buffer gas which served as the charge transfer partner as well. N_2^+ was irradiated continuously by a diode laser and the method proved to be very sensitive as conversion to Ar^+ proceeded with a rate constant $4\pm2\times10^{-10}\,cm^{-3}\,s^{-1}$. A later modification of the experimental set-up used a molecular beam of Ar that allowed measurements below 20 K without appreciable condensation of neutrals on the walls of the trap.

7.2.1 The experimental scheme

N_2^+ was generated by electron bombardment of the neutrals. After injection into the trap following mass selection, the ions were interacted with helium for 500 ms. Subsequently, the piezo valve was shut and the gas was pumped out. A delay of 450 ms was used before the ions were let out of the trap, to ensure that residual helium did not affect ion transmission to the detector and to avoid collision induced dissociation of weakly bound complexes. A 10 mW cw Titanium: Sapphire ring laser with a bandwidth of 0.5 MHz was the source of radiation. A mechanical shutter (Thorlabs) was used to regulate the exposure time to laser. The timing sequence is shown in Figure 7.5.

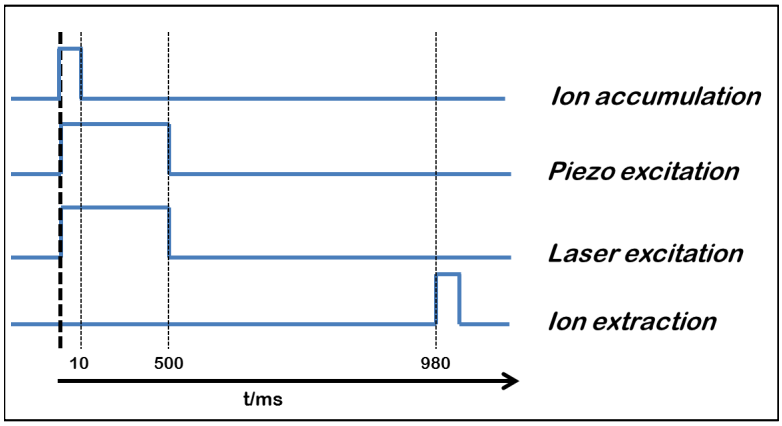

Figure 7.5: Experimental scheme employed for LIICG.

It is clear from Figure 7.5 that the ions are irradiated at the same time while they interact with helium. While collisions with helium resulted in complexation, the simultaneous addition of energy to N_2^+ via resonant excitation hindered the formation of N_2^+-He. The two competing processes along with collision induced dissociation of the complexes, lead to a stationary equilibrium in the trap. Collision induced population redistribution between the rotational levels was also found to play an important role.

Figure 7.6 shows the competing rate processes that were taken into account to obtain a complete picture of the LIICG method. Relaxation of the trapped ions occurs via bimolecular collisions with helium atoms, while complexation is a three body process. The rate constant of the latter is indicated by k_3. The $A^2\Pi_u(v' = 2, J') \leftarrow X^2\Sigma_g^+(v'' = 0, J'')$ electronic excitation of N_2^+ was chosen to be monitored for the present studies. The rotational transitions of this band are well characterised and the line positions are known with high accuracy. The electronic energy deposited into the ion is subsequently dissipated radiatively, the rate coefficient being k_{rad}. Further collisions with helium atoms result in

relaxation of the population from v>0 levels into v = 0. The efficiency of this step is determined by k_{rel}.

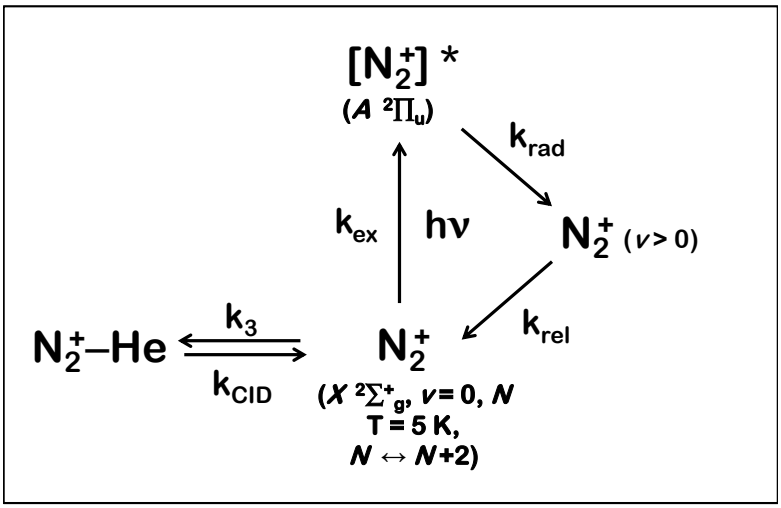

Figure 7.6: The elementary rate processes involved in the LIICG scheme.

All spectra measured by LIICG used cw lasers. A large k_{rel} implies fast population transfer from v > 0 levels into v = 0. Continuous excitation of the ions would pump them back into the higher electronic state immediately after relaxation. A pulsed laser would then be unsuitable. The ions would have enough time to relax and undergo conversion to complexes which is undesirable to observe a spectroscopic signal. However, recent theoretical work suggests that collisional quenching from $v = 1 \rightarrow v = 0$ occurs at $10^{-14}\,\mathrm{cm^3 s^{-1}}$. [18] This is also corroborated by the present observations, suggesting experimental realisation of LIICG should be possible with pulsed lasers as well.

7.2.2 Spectroscopy by LIICG

Figure 7.7 is a section of the $A^2\Pi_u(v' = 2, J') \leftarrow X^2\Sigma_g^+(v'' = 0, J'')$ electronic spectrum of N_2^+ measured by LIICG. The transitions were recorded by counting the number of complex ions as a function of the laser wavelength. Each point

was averaged over 10 cycles. Attempts to obtain a reference signal by measuring alternatively with and without laser were made to reduce the influence of long term fluctuations in the ions beam or helium density. However, this increased instabilities, caused most likely by the laser induced thermal fluctuations of the entrance and exit electrodes of the trap.

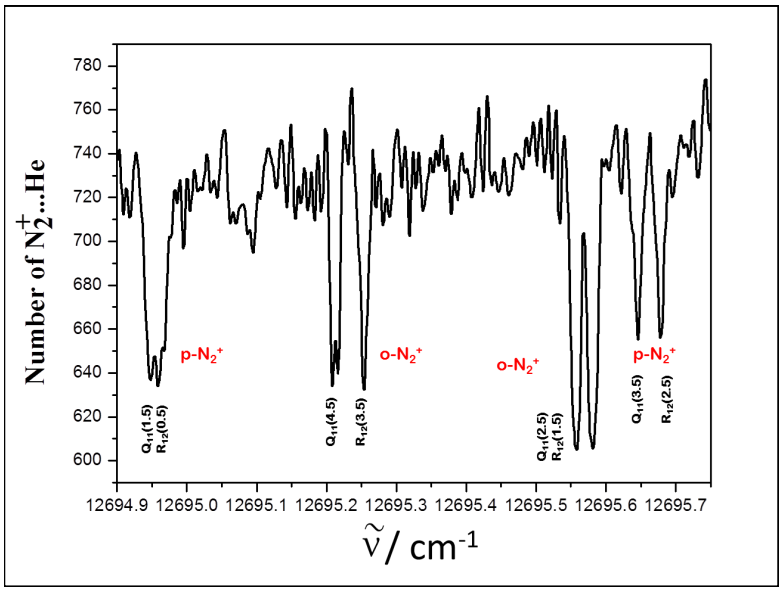

Figure 7.7: The $A^2\Pi_u(v' = 2, J') \leftarrow X^2\Sigma_g^+(v'' = 0, J'')$ electronic spectrum of N_2^+ measured by LIICG.

Figure 7.4 shows the energy levels involved. The observed rotational transitions arise out of the electronic fine structure components $F_1(J = N + 1/2)$ and $F_2(J = N - 1/2)$ of the N_2^+ ground state in its two nuclear spin components *ortho*-$N_2^+(N = 0,2,4...)$ and *para*-$N_2^+(N = 1,3,5...)$. Spin splitting in the electronic ground state leads to the doublet structure. It is well resolved for the measured transitions with exception of the two lines $Q_{11}(1.5)$ and $R_{12}(0.5)$. They are separated by $0.014\,cm^{-1}$ while the Doppler width at 5.5 K is $0.004\,cm^{-1}$, corresponding to 121 MHz. Analysis of several line profiles leads to a full width at half maximum of 350 ± 40 MHz. This gives a translational temperature (T_{trans}) of ~46 K. It remains to be understood whether the ions are hot translationally or the broadening is caused by laser power or collisions. The rotational temperature (T_{rot}) of the

ions can then be calculated from the mass weighted average of the translational temperatures of the ions and the buffer gas (Equation 6.2 in [19]) and was found to be 10.6 K.

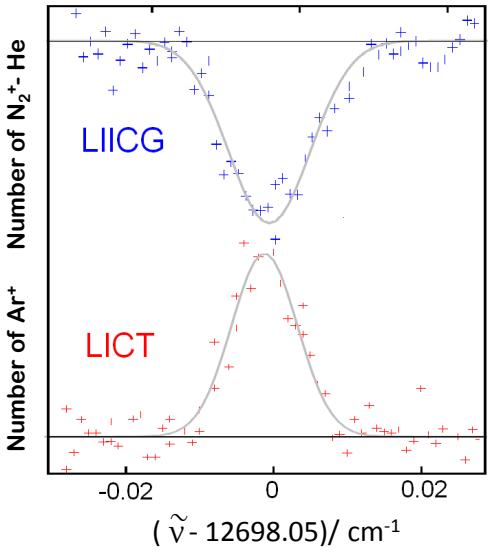

Figure 7.8: The Doppler profile of the $R_{11}(0.5)$ line measured by LIICG (decrease in N_2^+-He) and LICT (increase in Ar^+).

It was necessary to verify that the measured spectra had no overlapping contributions from photodissociation of N_2^+-He complexes. The observed line positions agreed within an accuracy of better than $0.005\,cm^{-1}$ with known spectroscopic constants. Figure 7.8 is another evidence. The upper part is the $R_{11}(0.5)$ line measured by LIICG while the bottom trace is the spectrum obtained by LICT. The line positions agree within $0.001\,cm^{-1}$. In another test, the ions were irradiated in the second half of the duty cycle. Neither inhibition nor dissociation was observed. Lastly, no optical transitions of N_2^+-He were observed which could have been due to fast predissociation in the excited $A^2\Pi_u$ state.

7.2.3 Characterisation of the rate processes

The changes in N_2^+-He complex numbers upon irradiation are not simply related to the population of the rotational levels. Table 7.1 lists the population of the rotational levels and observed depletion.

Table 7.1: Comparison of the population of the rotational states at $T_{rot} = 10.6\,K$ and observed depletion (in %)

N	Population	Depletion
0	31.8	-
1	28.4	37
2	33.3	26
3	4.9	32
4	1.6	19

As already stated, there are in reality two separate ion ensembles in the trap, *ortho* and *para*-N_2^+. Nuclear spin changing transitions are strictly forbidden. Therefore, the *ortho*:*para* ratio of 2:1, generated in the ion source, remains conserved. A rather efficient inhibition of N_2^+-He complex formation is achieved even when pumping from $N = 4$ level. Qualitatively, this can be attributed to fast refilling of this level by rotational relaxation.

A deeper understanding of the laser induced signal can be obtained by simulating the interactions of ion with helium and laser. The ion cloud is assumed to be composed of *ortho*-N_2^+ (N= 0, 2, 4, 6), N_2^+-He products and N_2^+* ("hot" ions). Electronic excitation to the $A^2\Pi_u$ state is not accounted for because radiative relaxation occurs in $10\,\mu$s and is much shorter than other time constants. The initial conditions chosen are summarised in Table 7.2. Relaxation of the rotational states have been accounted for as well by choosing $k_{N\to N-2} = 10^{-13}\,cm^3s^{-1}$. The reverse rates for excitation have been calculated by microscopic reversibility. While rotational relaxation occurs early, hot N_2^+* ions, created in the source due to electron impact, takes longer to equilibrate. The efficiency of the growth of N_2^+-He is reduced due to collision induced fragmentation. The used rate coefficient of only $10^{-14}\,cm^3s^{-1}$ for k_{CID}, is responsible for the stationary equilibrium

Table 7.2: Initial values of Population,P(); helium density,[He] ; T_{rot} and associated rate constants, $k_{()}$

Parameter	Initial Value
P(6)	0.5
$P(N_2^+*)$	0.5
P(all other)	0
[He]	$4.75 \times 10^{15}\,cm^{-3}$
T_{rot}	10.6 K
k_3	$1 \times 10^{-31}\,cm^6s^{-1}$
k_{CID}	$1 \times 10^{-14}\,cm^3s^{-1}$
k_{rel}	$1 \times 10^{-14}\,cm^3s^{-1}$

of 4.5 %, reached after 100 ms. The number of N_2^+-He is reduced to 1.1 % when the N_2^+ ions are excited with a rate of $500\,s^{-1}$. This result is in agreement with the low number of N_2^+-He complexes but large laser induced changes observed. For example, the measured number of complexes increases with density, but not quadratically as expected from ternary association alone, as shown in Figure 7.10. The red line corresponds to a quadratic fit.

The number of complexes has an inverse temperature relation as shown by the black trace in Figure 7.11. The blue trace corresponds to an exponential growth in the number of O_2^+, formed due to charge exchange with N_2^+. The O_2 neutrals start desorbing from the trap walls at temperatures above 20 K and their density was estimated to be $5{\times}10^8\,cm^{-3}$.

7.2.4 Discussion

The biggest advantage of LIICG over photodissociation and LICT is its generality. Ternary collisions should result in complex formation irrespective of the primary ion, although the relaxation period is expected to vary with the molecular ion. Being a one photon process, IVR is not expected to play a role in LIICG. The universality of helium attachment makes it a much superior technique compared to LIR or LICT.

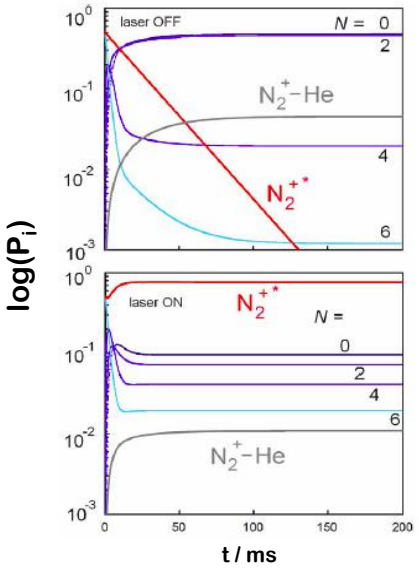

Figure 7.9: Simulation of evolution of rotational population with and without laser. 4.5 % of the parents are converted to complexes without laser. Exciting N_2^+ via $N = 2$ level in the $X^2\Sigma_g^+$ state with a rate of $500\,s^{-1}$ reduces the number of products to 1.1 % and the distribution reaches a non-statistical equilibrium before 50 ms.

It is obvious from the data presented, the successful application of LIICG heavily depends on high number densities($>10^{14}\,cm^{-3}$) and low temperatures. A cryostat that reaches temperatures of less than 5 K is desirable for this method. Care has to be taken so as to efficiently couple ion temperature to that of the trap and eliminate parasitic heating processes. The present apparatus has to improved in this regard because of the difference in the translational and internal temperatures reported. Clean vacuum conditions are also necessary to allow longer trapping cycles without loss in ion numbers. The current set-up needs to be modified to allow use of higher number densities. For example, the trap volume can be reduced further and differential pumping in the quadrupole chambers can be improved to prevent influence on ion transmission.

LIICG is not a background free technique. A fall in complex number is monitored upon absorption by the parent ion. Therefore, a stable primary ion beam along with highly reproducible conversion percentages are desired for the duration

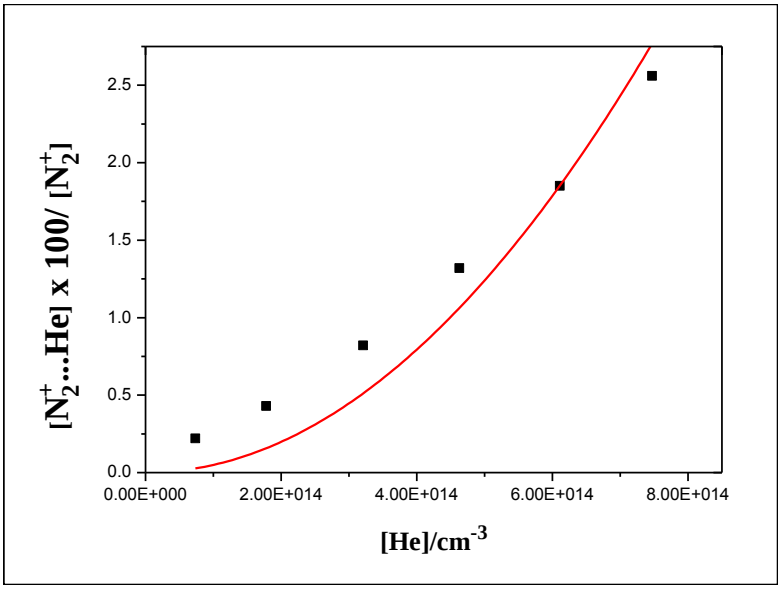

Figure 7.10: Percentage of complexes as a fucntion of [He]

of the experiment. There was an indication from the above experiments that laser induced heating of the end-cap electrodes of the trap may have influenced conductance of helium. Future measurements will aim to minimise photons striking the electrode surfaces.

Although all possible tests were done to eliminate contribution of complex dissociation in the recorded spectrum, the extent of helium induced perturbation on the spectrum remains unknown. Since the gas phase transitions of N_2^+ are rather well characterised, experimental diagnostics were sufficient in this case. The results of future experiments, however, may require detailed theoretical analysis.

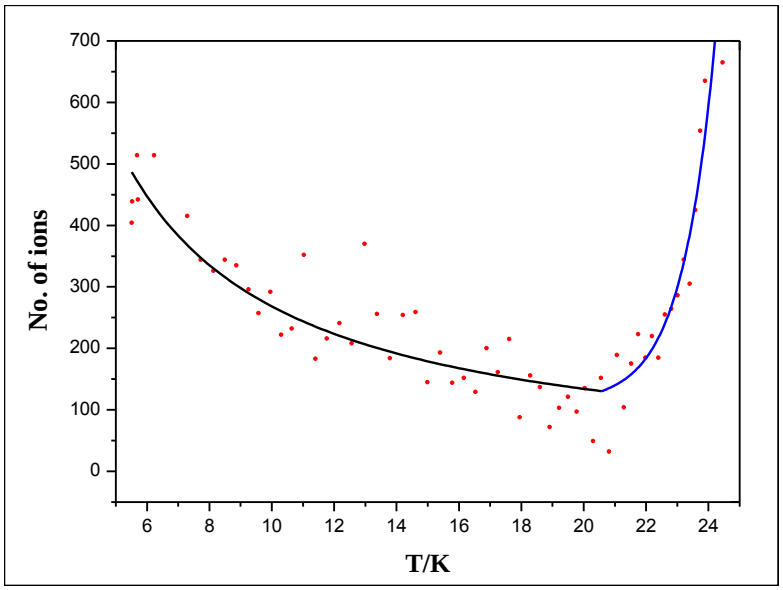

Figure 7.11: The number of ions that appeared at m/z 32 was counted as the temperature of the trap increased after switching the cryostat off. The complex ions disappeared when the trap warmed up. The sharp rise above 21 K is because of a charge exchange reaction between N_2^+ and O_2 neutrals desorbing from the trap surface.

Bibliography

[1] E.J. Bieske and O. Dopfer. High resolution spectroscopy of cluster ions. *Chem. Rev.*, 100:3963, 2000.

[2] K. Asmis and D. Neumark. Vibrational Spectroscopy of Microhydrated Conjugate Base Anions. *Acc. Chem. Res.*, 45:43, 2012.

[3] E. J. Bieske and J. P. Maier. Spectroscopic Studies of Ionic Complexes and Clusters. *Chem. Rev.*, 93:2603, 1993.

[4] M. Brümmer, C. Kaposta, G. Santambrogio, and K. R. Asmis. Formation and Photodepletion of Cluster IonMessenger Atom Complexes in a Cold Ion Trap: Infrared Spectroscopy of VO^+, VO_2^+ and VO_3^+. *J. Chem. Phys.*, 119:12700, 2003.

[5] M. Z. Kamrath, R. A. Relph, T. L. Guasco, C. M. Leavitt, and M. A. Johnson. Vibrational predissociation spectroscopy of the H2-tagged mono- and dicarboxylate anions of dodecanedioic acid. *Int. J. Mass. Spectrom.*, 300:91, 2011.

[6] J. Roithová J. Jašík, J. Žabka and D. Gerlich. Infrared spectroscopy of trapped molecular dications below 4 K. *Int. J. Mass Spectrom.*, 2013.

[7] R. Wester. Radiofrequency multipole traps: tools for spectroscopy and dynamics of cold molecular ions. *J. Phys. B: At. Mol. Opt. Phys.*, 42:154001, 2009.

[8] W. Paul, B. Lücke, S. Schlemmer, and D. Gerlich. On the dynamics of the reaction of positive hydrogen cluster ions (H_5^+ to H_{23}^+) with para and normal hydrogen at 10 K. *Int. J. Mass Spectrom.*, (149-150):373, 1995.

[9] S. Schlemmer, A. Luca, J. Glosik, and D. Gerlich. Temperature dependence of ternary rate coefficients for the $(CO)_{n-1}^+ + 2CO \rightleftharpoons (CO)_n^+ + CO$ reaction, and the role of isomers for the growth of larger $(CO)_n^+$ clusters. *J. Chem. Phys.*, 116:4508, 2002.

[10] J. Mikosch, R. Otto, S. Trippel, C. Eichhorn, M. Weidemüller, and R. Wester. Inverse Temperature Dependent Lifetimes of Transient SN2 Ion-Dipole Complexes. *J. Phys. Chem. A*, 112:10448, 2008.

[11] K.R. Asmis, G. Santambrogio, M. Brümmer, and J. Sauer. Polyhedral Vanadium Oxide Cages: Infrared Spectra of Cluster Anions and Size-Induced d-Electron Localization. *Angew. Chem. Int. Ed.*, 44:3122, 2005.

[12] A. B. McCoy, T. L. Guasco, C. M. Leavitt, S. G. Olesen, and M. A. Johnson. Vibrational manifestations of strong non-Condon effects in the $H_3O^+ \cdot X_3$(X = Ar, N_2, CH_4, H_2O) complexes: A possible explanation for the intensity in the "association band" in the vibrational spectrum of water. *PCCP*, 14:7205, 2012.

[13] T. W. Schmidt, T. Pino, J. van Wijngaarden, K. Tikhomirov, F. Güthe, and J. P. Maier. Electronic photodissociation spectra of the $Ar_n - C_4H_2^+$ (n= 1−4) weakly bound cationic complexes. *J. Mol. Spec.*, 222:86, 2003.

[14] D. Gerlich. Ion-Neutral Collisions in a 22-pole trap at very low energies. *Physica Scripta*, T59:256, 1995.

[15] K. Harada, T. Wada, and T. Tanaka. Near-Infrared Diode Laser Spectroscopy of the (2,0) Band of the $A^2\Pi_u \leftarrow X^2\Sigma_g^+$ system of the N_2^+ ion. *J. Mol. Spec.*, 163:436, 1994.

[16] J. C. Hansen, C. H. Kuo, F. J. Grieman, and J. T. Moseley. High resolution absorption spectroscopy of N_2^+ $X(v'' = 0) \rightarrow A(v' = 4)$ using charge exchange detection. *J. Chem. Phys.*, 79:1111, 1983.

[17] S. Schlemmer, T. Kuhn, E. Lescop, and D. Gerlich. Laser excited N_2^+ in a 22-Pole trap, Experimental Studies of Rotational Relaxation processes. *Int. J. Mass Spectrom. Ion Proc.*, 185:589, 1999.

[18] T. Stoecklin and A. Voronin. Strong isotope effect in ultracold collision of $N_2^+(v{=}1, j{=}0)$ with He: A case study of virtual-state scattering. *Phys. Rev. A*, 72:042714, 2005.

[19] Dieter Gerlich. Inhomogeneous Electrical Radio Frequency Fields: A Versatile Tool for the Study of Processes with Slow Ions,. *Adv. Chem. Phys.*, 82:1, 1992.

[20] T. Stoecklin and A. Voronin. Vibrational and rotational cooling of NO^+ in collisions with He. *J. Chem. Phys.*, 134:204312, 2011.

8 Conclusion

The 22-pole trap has evolved into a versatile tool for measuring spectra of ions. In this thesis, three different "indirect" techniques have been used to obtain electronic spectra of cations. The sensitivity of these methods have allowed successful laser interrogation of only few thousands of ions. Mass filtering prior to injection into the trap ensured only a specific ion was probed. Cryogenic cooling was used in all but one case to allow simplification of spectral analysis and comparison with astronomical data.

The $A^2\Pi_u \leftarrow X^2\Pi_g$ electronic spectrum of HC_4H^+ was measured with the objective of verifying the claim that the origin band of the $A^2\Pi_u \leftarrow X^2\Pi_g$ transition matched with a DIB. Simulated profiles of the origin band took into account interstellar broadening and non-Boltzmann rotational distributions and showed that neither the central wavelength nor the contour replicated the observed DIB. Two new vibrational bands of the same electronic transition were reported. Estimation of the spin-orbit temperature revealed that it was equilibrated to the rotational temperature. [1]

The $A^2\Pi_g \leftarrow X^2\Pi_u$ electronic spectrum of HC_6H^+ was recorded similarly. The broad range spectrum was compared to previously measured LIF spectrum [2] and discrepancies were noticed in the relative intensity patterns of the bands. A radiative collisional model was used to simulate the rotational profile under conditions similar to the ISM. (See Appendix A for details) [3]

Fortuitous discovery of C_4H_3Cl neutral in a sample of HC_4H led to the measurement of the $^2A' \leftarrow {}^2A''$ electronic transition of $C_4H_3Cl^+$. The unique aspect of this cation was the coexistence of its several isomers in the trap even at $\sim$20 K.

Extensive theory complemented with Matrix Isolation experiments helped reveal the structures of these isomers and explained their relative stabilities. [4]

Protonated benzene being the simplest ion of its category and a well known reaction intermediate in organic reactions, its $S_1 \leftarrow S_0$ electronic transition was looked at. The spectrum was broad with some features above the continuum.

The molecules mentioned above were all studied by one or another variant of the photodissociation approach. Electronic spectra of HC_4H^+ and HC_6H^+ were measured by a resonant two colour two photon dissociation scheme. The ion absorbed the first photon to undergo electronic excitation and subsequently fragmented due to the second photon. The two photons arrived at a delay of $\sim$10 ns. Radiative and non-radiative pathways were available to the photon to undergo relaxation into the vibrational manifold of the ground electronic state. Absorption of the fragmentation photon occurred out of these states. HC_4H^+ lost an H atom, while HC_6H^+ lost an H atom or a C_3H_2 unit.

The $C_4H_3Cl^+$ ion absorbed two photons of the same colour to be excited electronically and then subsequently lost a Cl atom.

$C_6H_7^+$ ion lost an H atom, but absorption of one photon in the UV was sufficient to promote the ion electronically and above the fragmentation threshold. The broad nature of the spectrum was most likely due to transition between a bound and repulsive state.

Inspite of it being a background free technique, analysis of photodissociation revealed it was not too well suited for the electronic spectroscopy of bare PAH cations. Therefore, later experiments focused on developing methods that could be employed more generally.

LICT was tested on the previously characterised $NCCN^+$ and $C_6H_4Cl_2^+$ ions. Ar was chosen as the neutral partner for the former, while $C_6H_5NO_2$ and CH_2Cl_2 were used for the later. The $C^2\Pi_u \leftarrow X^2\Pi_g$ electronic transition of $NCCN^+$ [5] was reproduced well by charge exchange with Ar. However, the $D^2\Pi_u \leftarrow X^2\Pi_g$ electronic transition was not observed, although reproducible features were recorded. This indicated that all collisions between an electronically excited ion and a neutral may not necessarily lead to charge exchange. The $B^2B_{3u} \leftarrow X^2B_{2g}$ of $C_6H_4Cl_2^+$

was measured but instead of charge transfer to the chosen organic neutrals, laser induced reactions were observed leading to unexpected mass channels. The use of molecules with rich internal structure meant the excess energy could partition in many different ways resulting in interesting gas phase chemistry.

The third technique, LIICG, was a completely new method that was developed and tested on the N_2^+ ion. [6] The $A^2\Pi_u(v' = 2, J') \leftarrow X^2\Sigma_g^+(v'' = 0, J'')$ electronic spectrum of this ion was measured successfully using this approach. The method is based on the concept that an ion with internal energy undergoes complex formation through three body collisions at a rate appreciably lower than one that is in its ground state. This excess energy was supplied in the form of resonant laser excitation. For N_2^+ ions, attachment of one helium atom was observed. The electronic spectrum of the bare ion was measured by monitoring a decrease in the number of ion complexes. Of the three methods discussed in this thesis and summarised above, the LIICG method appears to be the most promising. Provided sufficiently high number density of He can be achieved in the trap, complexation should occur as a natural consequence. For bigger ions with several vibrational modes, longer trapping times and helium number densities of upto $10^{17}\,\mathrm{cm}^{-3}$ in the trap may be necessary to achieve efficient vibrational relaxation before three body association reaction starts taking effect. Current measurements indicate that cw laser sources are the best suited for these purposes.

Bibliography

[1] J. P. Maier, S. Chakrabarty, F. J. Mazzotti, C.A. Rice, R. Dietsche, G. A. H. Walker, and D. A. Bohlender. Assignment of 5069 Å diffuse interstellar band to HC_4H^+: disagreement with laboratory absorption band. *Astrophys. J. Lett.*, 729:L20, 2011.

[2] D. Klapstein, R. Kuhn, J. P. Maier, M. Ochsner, and W. Zambach. Emission and Laser Excitation Spectra of the $A^2\Pi_g \leftrightarrow X^2\Pi_u$ Transition of Rotationally Cooled Triacetylene Cation. *J. Phys. Chem*, 88:5176, 1984.

[3] S. Chakrabarty, C. A. Rice, F. J. Mazzotti, R. Dietsche, and J. P. Maier. Electronic absorption spectrum of triacetylene cation for astronomical considerations. *J. Phys.Chem. A*, 2013.

[4] S. Chakrabarty, V. Rudnev, J. Fulara, R. Dietsche, A. Nagy, I. Garkusha, F. J. Mazzotti, C. A. Rice, and J. P. Maier. Electronic spectra of $C_4H_3Cl^+$ isomers. *Mol. Phys.*, 110:194307, 2012.

[5] C. A. Rice, V. Rudnev, S. Chakrabarty, and J. P. Maier. $D^2\Pi_u$, $C^2\Pi_u \leftarrow X^2\Pi_g$ electronic transitions of $NCCN^+$. *J. Phys. Chem. A*, 114:1684, 2010.

[6] S. Chakrabarty, M. Holz, A. Banerjee, D. Gerlich, and J. P. Maier. A new method to measure electronic spectra: The $A^2\Pi_u(v' = 2, J') \leftarrow X^2\Sigma_g^+(v'' = 0, J'')$ electronic transition of N_2^+ ions trapped in a 22-pole by Laser Induced Inhibition of Cluster Growth (LIICG).

A Appendix

Rotational population distribution in HC_4H^+ and HC_6H^+ in the ISM

In order to estimate the rotational state distribution in the electronic ground state of cations in the ISM, it is important to take into consideration magnetic dipole transitions and collisions with the background gas. Centro symmetric molecules that conform to Hund's case (a) lack a permanent dipole moment and pure rotational transitions can be induced by magnetic dipole. The expected positions of the magnetic dipole allowed rotational transitions were predicted for the molecules HC_2H^+, HC_4H^+, CO_2^+ and N_3 to aid their detection in the ISM. It was found that magnetic dipole and collision induced transitions are competitive leading to a non-Boltzmann population distribution.

In HC_4H^+, the rotational level of the $X^2\Pi_g$ state that is expected to have maximum population at 60 K is $J = 10.5$. For the lower J states, the rate of magnetic dipole transitions was estimated to be 10^{-9} s^{-1}. The rate increases to 10^{-8} s^{-1} for $J = 20.5$. Since the rate of collisions is of the order 10^{-8} to $10^{-7}\,s^{-1}$, the higher J values may have lesser occupation than predicted by Boltzmann distribution. This would result in a reduction of the tail of the R_1 and P_1 branches to the red. [1]

As in the case of HC_4H^+, the population of the rotational levels in the $X^2\Pi_u$ state of HC_6H^+ was modelled using a radiative-collisional approach. Along with the radiative decay and collisional rates, the influence of blackbody cosmic radia-

tion at 2.7 K were taken into consideration. Expressions for the upward collisional rates [2] were taken as follows:

$$k_{up}(i,j,T) \;=\; \alpha(T)\left(1+\frac{\frac{aE_i}{kT\delta_{MEG}}}{\frac{aE_i}{kT}}\right)^2 e^{\left(\frac{-\beta_{MEG}E_{ij}}{kT}\right)} \tag{A.1}$$

with the dependence of the normalising parameter being given by

$$\alpha(T) \;=\; AT^{-B}. \tag{A.2}$$

The downward collision rates were calculated form the expression: [3]

$$k_{down}(j,i,T) \;=\; k_{up}(i,j,T)\frac{2i+1}{2j+1}\frac{m_i}{m_j}e^{\left(\frac{-E_{ij}}{kT}\right)} \tag{A.3}$$

where $\frac{m_i}{m_j}$ is the ratio of nuclear spin statistics and is 3:1 for the antisymmetric (a) to symmetric (s) levels. Without radiative rates, the distribution is Boltzmann and the rotational and kinetic temperatures are equal. The values for the parameters were that of CO. Absorption and stimulated emission of a photon is induced by the background blackbody radiation. The respective rate constants are given by,

$$k_{stim,ji} = \frac{A_{ji}}{e^{\frac{E_{ij}}{kT}}-1} \tag{A.4}$$

$$k_{abs,ij} = \frac{2j+1}{2i+1}\frac{m_j}{m_i}\frac{A_{ji}}{e^{\frac{E_{ij}}{kT}}-1} \tag{A.5}$$

where A_{ji} is the Einstein coefficient of spontaneous emission. Collisional rates between $a\leftrightarrow$ s were neglected and only those between $s\leftrightarrow$ s and $a\leftrightarrow$ a were considered. In the $\Omega =$ 3/2 manifold, $J=$ 3/2 has a a:s::3:1 ratio. The symmetry restriction of the *e/f* levels and their respective nuclear spin statistics (g_{ns})comes from the fact that J-3/2 is even. When collision induced $\Delta\Omega\pm$ 1 transitions are neglected, then the upper spin-orbit component is completely depopulated. Since the triacetylene cation does not have a dipole moment, the rotational levels are coupled via magnetic dipole transitions. The radiative rates were calculated with PGOPHER for a magnetic dipole transition of the $X^2\Pi_u$ state. This was done by

taking the transition tensor to be a sum of an orbital transition moment and a spin transition moment (two components, a zero for the projection of the spin on the internuclear axis (same Ω component) and a one for the ladder operator connecting states of different Ω). Radiative transition between $\Omega = 1/2$ to $3/2$ occurs at a faster rate than collisional relaxation for the density range: 1- $10^5\,\mathrm{cm}^{-3}$. Rates of upward transitions due to collisions decrease exponentially with increasing J. As a result the rates of R_{11} and R_{22} become predominant. The profile of the origin

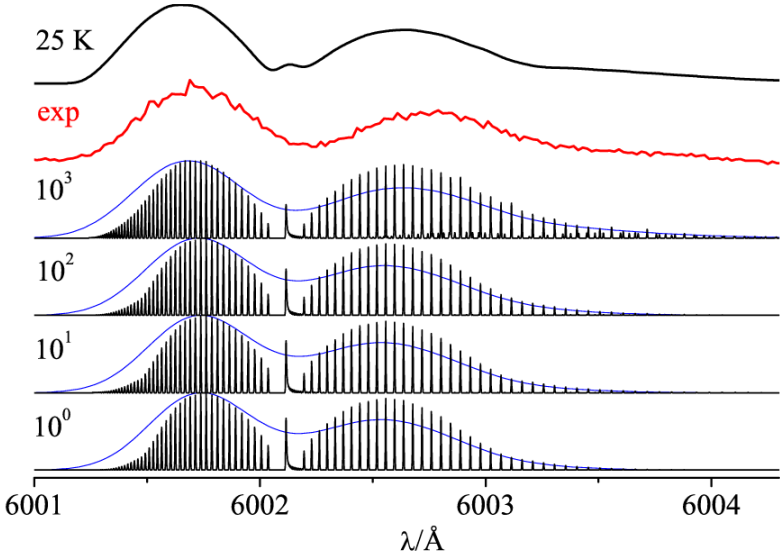

Figure A.1: The red trace is the experimental origin band of the $A^2\Pi_g \leftarrow X^2\Pi_u$ electronic transition of HC_6H^+ recorded with a 0.05 Å laser bandwidth. The top trace is the simulated profile. A Gaussian of 0.1 Å and a Boltzmann temperature of 25 K was used. The rest are predicted rotational profiles of this band as a function of collision partner density in cm^{-3}. Individual J lines with a 0.007 Å fwhm at 6000 Å are shown in black. The blue overlays were obtained for a velocity dispersion of $18\,\mathrm{km\,s}^{-1}$.

of the $A^2\Pi_g \leftarrow X^2\Pi_u$ electronic transition was simulated with a linewidth of $1\,\mathrm{cm}^{-1}$. This is equivalent to an interstellar cloud velocity dispersion of $18\,\mathrm{km\,s}^{-1}$. The profile shows up as nearly a single peak for low temperatures corresponding to negligible collisions, when the ion is equilibrated to 2.7 K blackbody radiation. The P_{11} and R_{11} branches start to split up at higher temperatures, into two distinct

features. At higher densities, the collisional rates are faster than radiative ones and the $\Omega = 1/2$ component start becoming prominent.

The results of the modelling can be summarised as: The rotational temperature is lower than the kinetic one of the surrounding gas upto a threshold of the dimensionless parameter $\rho \approx 107$, where $\rho = (N \times \alpha(60K))/2.5A_{j,j-1}$. The $\Omega = 1/2$ component is depopulated when spin conversion by collisions is not considered. The spin-orbit temperature is then equilibrated to the 2.7 K blackbody radiation.

Bibliography

[1] M. More and J. P. Maier. Detection of nonpolar ions in $^2\Pi_{3/2}$ states by radioastronomy via magnetic dipole transitions. *Astrophys. J.*, 732:103, 2011.

[2] A. E. Belikov and M. A. Smith. State-to-state rate coefficients for rotational relaxation of CO in Ar. *J. Chem. Phys.*, 110:8513, 1999.

[3] F. Lique, A. Spielfiedel, M.-L. Dubernet, and N. Feautrier. Rotational excitation of sulfur monoxide by collisions with helium at low temperature. *J. Chem. Phys.*, 123:134316, 2005.